Pontifícia Universidade Católica
do Rio de Janeiro

Gabriela de Castro Almeida

Numerical investigation of the evolution of blood flow patterns of different years in patients with ascending aortic aneurysm

Dissertação de Mestrado

Dissertation presented to the Programa de Pós-graduação em Engenharia Mecânica of PUC-Rio in partial fulfillment of the requirements for the degree of Mestre em Engenharia Mecânica.

Advisor: Prof. Angela Ourivio Nieckele
Co-advisor: Dr. Bruno Alvares de Azevedo Gomes

Rio de Janeiro
February 2019

Gabriela de Castro Almeida

The author is a graduate in Mechanical Engineering from Universidade Federal de Juiz de Fora, Juiz de Fora, Minas Gerais, in 2016, and is currently a postgraduate student in the Mechanical Engineering program at PUC-Rio. She has experience in the area of computational fluid dynamics and bioengineering, subjects oriented to the academic and scientific fields.

Bibliographic data

Almeida, Gabriela de Castro

Numerical investigation of the evolution of blood flow patterns of different years in patients with ascending aortic aneurysm / Gabriela de Castro Almeida ; advisor: Angela Ourivio Nieckele ; co-advisor: Bruno Alvares de Azevedo Gomes. – 2019.
118 f. : il. color. ; 30 cm

Dissertação (mestrado)–Pontifícia Universidade Católica do Rio de Janeiro, Departamento de Engenharia Mecânica, 2019.
Inclui bibliografia

1. Engenharia Mecânica – Teses. 2. Aneurisma de aorta. 3. Aorta. 4. Dinâmica dos fluidos computacional. 5. Hemodinâmica. I. Nieckele, Angela Ourivio. II. Gomes, Bruno Alvares de Azevedo. III. Pontifícia Universidade Católica do Rio de Janeiro. Departamento de Engenharia Mecânica. IV. Título.

CDD: 621

To João Vicente

Acknowledgements

I thank my parents, Marcelo and Márcia, my son João Vicente and my brother Rafael for all patience, strength and support that provided to me.

Thank you to all the professionals at PUC-Rio. Without the work of each one, this dissertation would not be possible. I am very grateful to my mentors Angela and Bruno for all knowledge, suggestions and unrestricted assistance provided. You are inspiring.

To the Cardiovascular Engineering Team, for all the meetings, discussions and stimulate in improving my work.

The friends I made during the master's degree: Monique for opening the doors of her home to me; Ivan, for always being willing to help; Ingrid in the moments of outburst; Renan being always empathetic and Omar with good conversation.

My cousin Simone, who helped me immensely by giving a room, her conversations, advisors and prayers helped me a lot.

I also gratefully acknowledge the financial support of CNPq.

Abstract

Almeida, Gabriela de Castro; Nieckele, Angela Ourivio (Advisor); Gomes, Bruno Alvares de Azevedo (Co-advisor). **Numerical investigation of the evolution of blood flow patterns of different years in patients with ascending aortic aneurysm.** Rio de Janeiro, 2019. 118p. Dissertação de Mestrado – Departamento de Engenharia Mecânica, Pontifícia Universidade Católica do Rio de Janeiro.

Arterial aneurysmal is defined as an excessive dilation of the normal diameter of an artery. Ascending aortic aneurysm is generally asymptomatic, so it is often accidentally identified during routine imaging examinations. After the aneurysm has been identified, if there is no surgical indication, the patient should be followed adequately, since arterial rupture can be fatal. The influence of blood flow on aortic remodeling is an important area of investigation. The aim of this study is to identify hemodynamic patterns in ascending aortic aneurysms that may be related to aneurysm enlargement. Each patient in the study was evaluated at two different times. A three-dimensional model of the ascending aortic aneurysm was generated for each patient from aortic angiotomography examinations. The flow field was numerically determined with a commercial software. It has been shown that the angle between the entrance of the main flow and the brachiocephalic trunk can induce an incident jet on the aortic wall, causing areas of recirculation in the posterior region of the jet, besides high values of pressure and wall shear stress. The present hemodynamics findings may be related to remodeling of the ascending aorta.

Keywords

Ascending Aortic Aneurysm; Aorta; Computational Fluid Dynamics; Hemodynamics.

Resumo

Almeida, Gabriela de Castro; Nieckele, Angela Ourivio; Gomes, Bruno Alvares de Azevedo. **Investigação numérica da evolução dos padrões de fluxo sanguíneo de diferentes anos em pacientes com aneurisma de aorta ascendente.** Rio de Janeiro, 2019. 118p. Dissertação de Mestrado – Departamento de Engenharia Mecânica, Pontifícia Universidade Católica do Rio de Janeiro.

Aneurisma arterial é definido como uma dilatação excessiva do diâmetro normal de uma artéria. O aneurisma da aorta ascendente é geralmente assintomático, portanto, é frequentemente identificado acidentalmente durante exames de imagem de rotina. Após a identificação do aneurisma, caso não haja indicação cirúrgica, o paciente deve ser acompanhado de maneira adequada, pois a ruptura arterial pode ser fatal. A influência do fluxo sanguíneo no remodelamento aórtico é uma importante área de investigação. O objetivo deste estudo é identificar padrões hemodinâmicos em aneurismas de aorta ascendente que possam estar relacionados com o aumento do aneurisma. Cada paciente do estudo foi avaliado em dois momentos distintos. Um modelo tridimensional do aneurisma de aorta ascendente foi gerado para cada paciente a partir de exames de angiotomografia de aorta. O padrão de fluxo foi determinado numericamente com a utilização de um software comercial. Foi demonstrado que o ângulo entre a entrada do fluxo principal e o tronco braquiocefálico pode induzir a uma incidência de um jato incidente na parede da aorta, ocasionado áreas de recirculação na região posterior do jato, além de altos valores de pressão e tensão cisalhante. Os presentes achados hemodinâmicos podem estar relacionados com o remodelamento da aorta ascendente.

Palavras-chave

Aneurisma de Aorta; Aorta; Dinâmica dos Fluidos Computacional; Hemodinâmica.

Summary

List of figures

List of tables

List of Symbols and Abbreviations

AAA	Abdominal Aortic Aneurysm
AAoA	Ascending Aortic Aneurysm
ξ	Blending Factor
CTA	Computerized Tomography Angiography
CFD	Computational Fluid Dynamics
m	Convergence Order
x	Coordinate Axe
y	Coordinate Axe
i	Coordinate Direction
j	Coordinate Direction
ρ	Density
Γ	Diffusion Coefficient
DICOM	Digital Imaging and Communication in Medicine
$\bar{P}$	Dimensionless Mean Pressure
$\overline{WSS}$	Dimensionless Mean Wall Shear Stress
P	Dimensionless Pressure
ω^+	Dimensionless Specific Dissipation
Ω	Dimensionless Specific Rate of Dissipation
K	Dimensionless Turbulence Kinetic Energy
y^+	Dimensionless Wall Distance
V_x	Dimensionless x-Velocity
V_y	Dimensionless y-Velocity
DNS	Direct Numerical Simulation
n	Direction Normal
y	Distance from the wall
μ	Dynamic Viscosity
D	Effective Inlet Diameter
ϵ	Error
FIJI	Fiji is Just ImageJ
F	First
u^*	Friction Velocity

ϕ	Generical Variable
GCI	Grid Convergence Index
w_{in}	Inlet Normal Velocity
Q_{in}	Inlet Volumetric Rate
I	Intensity
δ_{ij}	Kronecker Delta
LES	Large Eddy Simulation
ℓ	Length Scale
l	Liters
$\tilde{P}_\kappa$	Limited Production of Turbulent Kinetic Energy
S	Magnitude of the Strain Rate
ϕ	Main Area of Interest
TSS_{max}	Maximum Turbulent Shear Stress
$\bar{P}$	Mean Pressure
w_m	Mean Velocity of the Fluid
$\overline{WSS}$	Mean Wall Shear Stress
h	Mesh
m	Meters
min	Minute
$\hat{p}$	Modified Pressure
μ	Molecular Viscosity
τ_w	Normal Tangential Gradient
σ	Normal Stress
Pa	Pascal
PIV	Particle Image Velocimetry
p	Pressure
p_{in}	Pressure at Inlet
P_κ	Production of Turbulent Kinetic Energy
Q	Q-criterion
Re	Reynolds
RANS	Reynolds-averaged Navier-Stokes
$-\rho\overline{u_i' u_j'}$	Reynolds Strain Rate Tensor
σ_{Re}	Reynolds Stress

Ω_{ij}	Rotation
F_s	Safety Factor
S	Second
s	Seconds
SIMPLE	Semi-Implicit Method for Pressure-Linked Equations
SST	Shear Stress Transport
ω	Specific Turbulent Dissipation Rate
γ	Strain Rate Magnitude
S_{ij}	Strain Rate Tensor
A_{ref}	Superficial Aorta's Area
t	Time
TAA	Thoracic Aortic Aneurysm
3D	Three-Dimensional
TDMA	Tridiagonal Matrix Algorithm
ε	Turbulence Dissipation Rate
κ	Turbulent Kinetic Energy
TKE	Turbulent Kinetic Energy
σ_κ	Turbulent Prandtl Number of Kinetic Energy
σ_ω	Turbulent Prandtl number of Specific Dissipation Rate
Re_t	Turbulent Reynolds Number
μ_t	Turbulent Viscosity
U	Velocity
u	Velocity
τ_{ij}	Viscous Stress Tensor
Ω_{ij}	Vorticity Tensor
WSS	Wall Shear Stress
V_x	Dimensionless x-Velocity
V_y	Dimensionless y-Velocity

Learning is the only thing the mind never exhausts, never fears, and never regrets

Leonardo da Vinci

1
INTRODUCTION

The aorta is the major artery of human organism. Its main purpose is to receive oxygenated blood from the heart and to distribute it to the human body. The aorta is connected to the heart at its base and it forms an arch before being directed to the abdominal region, as shown in Fig. 1.1. The arch's downward portion, called the descending aorta is connected to a network of arteries that supplies most of the body with oxygen-rich blood. The upper part of the arch is responsible to distribute blood to upward members and head. The part which is connected to the heart until the arch part is called the ascending aorta (Standring, 2016).

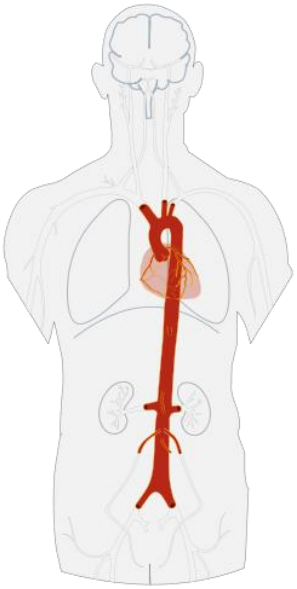

Figure 1.1 – Aorta in a human body. (CC BY-SA 3.0)

An aneurysm is a bulge that forms in the wall of an artery. The existence of an aneurysm is defined when the artery´s diameter exceeds 1.5 times the normal diameter. Aneurysms can be formed anywhere in the body, and they are very dangerous because they can rupture and cause massive internal bleeding. Ascending aortic aneurysm is particularly more serious, because a rupture in this part of the body can be life threatening. Frequently this disease is asymptomatic and in many cases, it is discovered by accident when a chest X-ray or other screening exam is required for different reasons (Standring, 2016).

When a patient presents an aneurysm larger than 6 cm in diameter, surgery is indicated. On the other hand, if an aneurysm has been diagnosed, but is not too large, surgery should be avoided, but the patient must be followed up. For some patients, the aneurysm does not grow while other patients present a significant growth in a relatively short time period. The reasons for the different behaviors related to the development of an aneurysm are not yet know. It is believed that changes in the blood flow can influence the disease development (Hope et al., 2007).

Frequently, changes in blood flow along the segment of the ascending aorta are related to the aortic remodeling associated with various pathological conditions, such as bicuspid aortic valve, aortic stenosis, dilatation, aneurysmal formations and tortuosity (Faggiano et al., 2013; Ha et al., 2016).

Computational Fluid Dynamics (CFD) has gained a lot of interest as a complementary tool for improving understanding of pathogenesis and disease progression in cardiovascular disease (Sun & Chaichana, 2016) .

Identification of regions where the wall shear stress and pressure has large values is important because these quantities are associated with aneurysmal dilatation of the ascending aorta (Bürk et al., 2012).

According to the previous observations, it can be believed that the use of CFD to study the blood flow path along the aorta of particular patients can contribute in the impact of the quality of life, getting better prognosis in patients with ascending aortic aneurysm.

1.1. Objectives

The goal of the present dissertation is to investigate numerically the flow path through the ascending aorta of six patients, at two different times, aiming to identify some flow characteristic that might be associated with the growth of an ascending aortic aneurysm (AAoA).

To perform the study, three-dimensional aortic models were obtained from six patients diagnosed with AAoA. Two examinations at different times were collected and the patients were classified into aneurysms that grew and did not grow. Hemodynamic flow was numerically determined and analyzed.

1.2. Organization of the Manuscript

This text is divided in five chapters. In the next chapter it is presented a literature review regarding the areas of study, medical and engineering, required

for the development of the research.

In Chapter 3 the mathematical and numerical models employed for the present analysis are described.

The flow field through the ascending aorta of six patients is presented and analyzed in Chapter 4, where the patients were classified in two groups depending if the aneurysm aortic grew or did not growth. Finally, Chapter 5 presents general conclusions and suggestions for future works.

2
LITERATURE REVIEW

The bibliographic review chapter was divided into 2 sub-sections. In the first section, basic cardiovascular anatomy and aorta's physiology with particular interest in the layers that form the aorta as they are the entities most affected by an aneurysm, are introduced. It also includes studies related with the aorta´s pathology, which is this study focus, the ascending aortic aneurysm. Its incidence, risk factors, symptoms and treatment modalities are discussed.

The second section presents the application of Computational Fluid Dynamics modeling in hemodynamics study to determine the flow field through the aorta. It also includes the description of studies that have captured changes in blood flow patterns in aortic models with aneurysm. A discussion of the wall shear stress parameter is introduced since it is widely considered to be one of the principal indicator of blood flow anomalies in aneurysmatic pathology. In order to better reproduce the complex fluid dynamics of blood flow that occur in the aortic region, approximations are necessary to employ computational analysis. One important topic is the blood viscosity, which has been studied by a few authors. Finally, some studies that compare models of steady state blood flow with transient models are mentioned.

2.1. Cardiovascular Anatomy of Aorta

The cardiovascular system is the transport system of the body. It consists on heart, which pumps blood into the pulmonary circulation for gas exchange and into the systemic circulation to supply oxygen to the body tissues; and the vessels that carry the blood, including arteries, arterioles, capillaries, venules, and veins (Porth et al., 2009).

Blood is a fluid connective tissue, formed by platelets, white and red blood cells and plasma, which circulates through the cardiovascular system through blood vessels. Blood vessels are tubes that carry blood. Veins are blood vessels, which carry blood from the body back to the heart. Arteries are blood vessels that reach the body's tissues and carry blood from the heart to the body (McMillan & Harris, 2018).

The heart is a hollow muscular organ that is divided into four chambers. Figure 2.1 shows a diagram of the human heart. The right atrium receives the blood from the systemic circulation via the superior and inferior venae cavae. The right ventricle receives the blood from the right atrium and pumps into the pulmonary circulation via the pulmonary trunk and pulmonary arteries. The left atrium receives the blood from the lungs via pulmonary veins. The left ventricle receives the blood from the left atrium and pumps it into the systemic circulation via the aorta. The atria and ventricles are separated by atrioventricular valves that prevent the blood from refluxing into the atria when the ventricles contract. Likewise, the two major outflow vessels, the pulmonary trunk from the right ventricle and the ascending aorta from the left ventricle, possess the pulmonary valve and the aortic valve, respectively (Hansen, 2014).

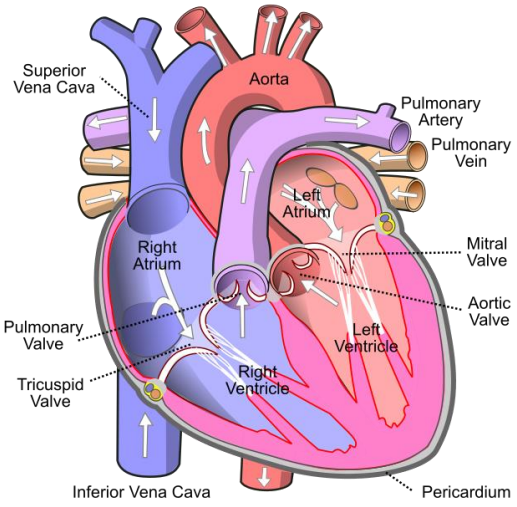

Figure 2.1 – Diagram of the human heart. (CC BY-SA 3.0)

The largest artery in the human body is the aorta, showing a physiological diameter ranging between 25 and 35 mm in adults.

Figure 2.2 shows schematically the thoracic aorta. The heart is connected to the aortic root, which receives blood from the left ventricle. In the aortic root, the aorta branches off into two main coronary blood vessels. The right and left main coronary arteries, that ramify into smaller arteries, are responsible to supply oxygen-rich blood to the entire heart muscle. The aortic arch connects the ascending aorta and the descending aorta, which is connected to the thoracic, leading to the abdominal aorta. Several arteries extend from the aorta to deliver blood to the various regions of the body. The aorta carries and distributes blood rich with oxygen to all arteries, with the exception of the main pulmonary artery (Standring, 2016).

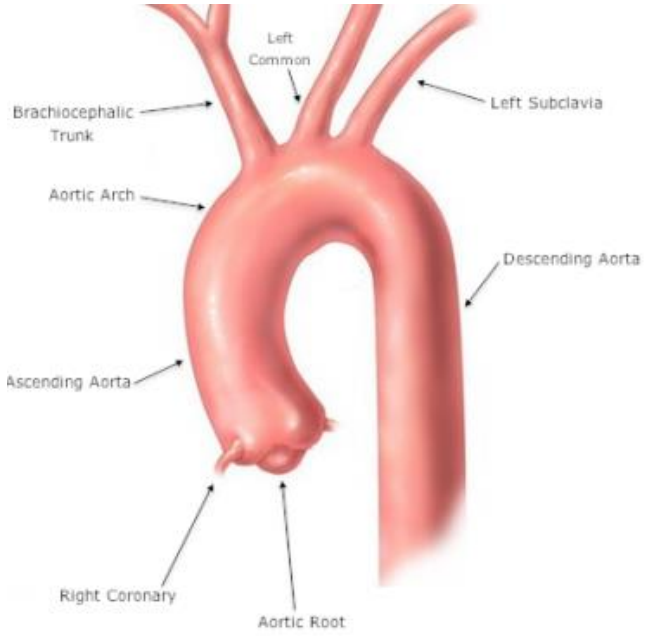

Figure 2.2 – Physiologic thoracic aorta. (Criscione, 2013)

Arteries surfaces, including aorta, are comprised of three distinct layers: the tunica adventitia, the tunica media and the tunica intimate. The outer layer or adventitia is formed of irregularly arranged collagen bundles, providing support and structure to the artery. The middle layer, media, is thicker and contains arranged elastic fibers, connective tissue and smooth muscle cells. The inner layer, intima, corresponds to the surface along which the blood flows. The media layer accomplishes the compliant function being the largest thickness at the ascending aorta wall, which are the most requested of the entire aorta (Marieb et al., 2005).

Researchers suggested that the fluid dynamics of blood flow through these regions might play a significant role in the initiation and propagation of lesions along the arterial wall (Schwartz & Mitchell, 1962; Wesolowski et al., 1965; Wienbaum & Caro, 1976; Yearwood & Chandran, 1980).

It has been demonstrated that severe mechanical trauma, sustained by endothelial cells in the arterial wall, due to high fluid shearing stresses, serves to promote the development of these lesions (Fry, 1968).

When a part of the aortic wall is dilated and thereby forms a bump, or when the diameter is increased to a degree at least 1.5 greater than normal in a fusiform manner, the condition is called aneurysm (JCS, 2013).

Aortic aneurysm is a circumferential or local enlargement of a part of the aortic wall. Aortic aneurysms are described in their location, morphology and cause. The aneurysm location can be classified as thoracic, thoracoabdominal and abdominal regions (JCS, 2013).

The incidence of abdominal aortic aneurysms (AAAs) has increased during the past two decades, due in part to the aging of the population, the rise in the number of smokers, the introduction of screening programs and improved diagnostic tools (Mathur et al., 2016). The disorder is more common in men than in women, with prevalence rates estimate at 1.3-8.9% in men and 1.0-2.2% in women (Lederle et al., 2000). However, thoracic aortic aneurysms (TAAs) have an estimated incidence of at least 5-10 per 100,000 person-years, and can be classified according to your location (Kuzmik et al., 2012). Ascending aortic aneurysms (AAoA), shown in Figure 2.3, are most common (≈60%), followed by aneurysms of the descending aorta (≈35%) and aortic arch (<10%) Thoracoabdominal aortic aneurysm refers to descending thoracic aortic aneurysms that extend distally to involve the abdominal aorta. (Kuzmik et al., 2012).

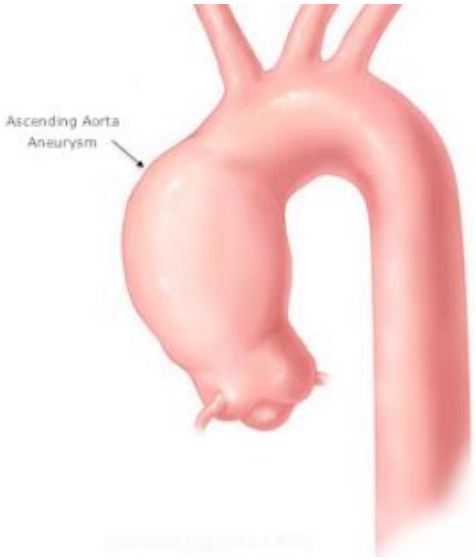

Figure 2.3 – A typical example of and ascending aortic aneurysm (Criscione, 2013)

Data from Department of Informatics of the Unified Health System, Ministry of Health – Brazil, reveal that aortic aneurysm and aortic dissection rank among 40 leading causes of death for all Brazilians (all races, all ages, both sexes) (DATASUS, 2016). Despite the lethality of these disease processes, their underlying mechanisms remains understood.

Risks factors for TAA are thought to include increasing age, male sex, smoking (Landenhed et al., 2015), arteriosclerosis, hypertension (Kato et al., 2008), and inflammatory or autoimmune diseases (Chen et al., 2006) that affect the aorta.

The most common TAA, the ascending aortic aneurysm AAoA, is generally

asymptomatic in most patients. They are essentially diagnosed incidentally during clinical examination or during population screening (Mathur et al., 2016).

In the ascending aorta, progressive dilation may lead to aortic valve insufficiency (even in anatomically normal valves), acute dissection, or spontaneous rupture (Albuquerque et al., 2004).

Surgery is recommended for asymptomatic aneurysms with a diameter above 6 cm (Erbel et al., 2001), as well as when there is presence of symptoms or aortic valve insufficiency.

Once an aneurysm reaches a maximum diameter of 6 cm, the annual probability of rupture, dissection, or death is 14.1% (Elefteriades, 2002). Approximately 50% of patients with acute untreated ascending aortic dissection die within 48 hours, and those undergoing emergency surgery have 15-26% mortality (Hagan et al., 2000; Ehrlich et al., 2000). Elective surgery lowers mortality to only 3-5% (Isselbacher, 2005).

The successful treatment of ascending aortic aneurysm consists of a careful monitoring and referral for surgical consultation to avoid rupture or dissection of the aneurysm, reducing the morbidity and mortality associates of this pathophysiology (Saliba & Sia, 2015).

2.2. Aorta´s Modeling

Goldsmith & Skalak (1975) demonstrated that hemodynamics comprises a large field and provides examples of a variety of mechanical-fluid phenomena. Yoganathan et al. (1988) reviewed the principles of hemodynamic of circulatory system, emphasized internal flow, free jet and the role of acceleration and deacceleration in turbulent flow.

With the advent of new faster and larger computers and efficient numerical schemes to solve the equations that govern fluid dynamics, the computational fluid dynamics began to be applied in hemodynamics study. De Leval et al. (1996) applied the finite-element technique to study the flows inside veins in cavopulmonary connections. The volume finite method, is a numerical technique highly developed, and largely applied in engineering studies to analyze flow field of different fluids. It has also be employed to solve the equations governing blood flow (Hunter et al., 2003).

Researchers have been documenting two hemodynamic scenarios that occur in AAoA patients: the jet eccentricity of blood flow and the helical systolic flow (Criscione, 2013). In the first scenario, the jet is not aligned with the central

ascending aorta axis, it deviates from the axis, hitting the aorta wall (Hope et al, 2007). In second scenario which is more evident in dilated or aneurysmatic cases, the ejected flow forms spirals moving towards the aortic arch (Numata et al, 2016). In case of Hope et al. (2007)'s research group, the difference in flow patterns between healthy volunteers and ascending aortic aneurysm patients using time-resolved three-dimensional (3D) was studied, by employing phase contrast magnetic resonance velocity (4D-flow) profiling. The 4D-flow technique was performed on 19 healthy volunteers and 13 patients with ascending aortic aneurysms. Vector fields placed on 2D planes were visually graded to analyze helical and retrograde flow patterns along the aortic arch. In volunteers, flow progressed as an initial jet of blood skewed toward the anterior right wall of the ascending aorta is reflected posterolaterally toward the inner curvature creating opposing helices, occurring retrograde flow along the inner curvature between the location of the two helices. In the aneurysm patients, the helices were larger; retrograde flow occurred earlier and lasted longer. It was concluded that dilation of the ascending aorta skews normal flow in the ascending aorta, changing retrograde and helical flow patterns. Hope et al. (2007) study is very interesting to begin understanding the behavior of the blood flow in AAoA cases.

Weigang et al. (2008) study discusses that the flow impact at aortic wall might affect pathogenesis and the progression of thoracic aortic diseases. Six patients suffering from ascending aortic aneurysms and one healthy individual were investigated. Patients with ascending aortic aneurysms reveal considerable differences in local flow patterns among themselves when compared to healthy individuals.

As was stated in certain publications, *in vitro* (Morbiducci et al., 2007) and *in vivo* (Morbiducci et al., 2009) relates the detection of abnormalities in the expected physiological flow with the development of helicity in aorta, which occurs mainly to the asymmetry of blood flow.

Gülan et al. (2018) observed that counterclockwise helical flow patterns are developed from the ascending aorta and are extended towards the aortic arch in the healthy case. In the aneurysmal case, however, it was found formation of large rotational regions in the systolic phase, which shows qualitative similarity with vortex ring formation, mainly a central jet and two large vortices, seen in patients with ascending aortic aneurysms, as it was found in the study of Weigang et al. (2008). From a fluid mechanical point of view, a sudden increase in diameter leads to a separation of the boundary layer and a separation bubble, and hence it is likely that there is an analogy between the separation, the associated turbulence and

pressure loss and aneurysm growth (Gülan et al., 2018).

Coherent structures are often related with regions of high vorticity, but there is no universal threshold over which vorticity is to be considered high (Haller, 2005). The first 3D vortex criterion was proposed by Hunt, Wray & Moin (1988) and it is denominated as Q-criterion. This criterion allows define coherent structures in the fluid (Holmén, 2012).

Several type of coherent structures have been identified in a turbulent flow. It can be vortex rings inside of fluid, behaving as an enclosed volume circulating along streamline. That rings can be visualize as a toroidal volume of vertical fluid moving in a surrounding medium at an approximately constant translational speed perpendicular to the ring plane (Akhmetov, 2009).

Another coherent structure that has been identified is the hairpin vortex, and it has been first visualized in the study of turbulent wall layer (Zhou et al., 1999). it was first proposed by Theodorsen (1952), which visualized a vortex filament distancing from the wall, so called the arch or head. That arch is oriented spanwise to the mean flow, and perturbed by a small upward motion. It was formed by higher mean flow velocity, which was convected downstream faster than its lower-lying parts.

According to Adrian (2007), the single hairpin eddy is a useful paradigm that explains many observations in wall turbulence. It can provide a mechanism for creating high Reynolds shear stress at the wall, low-speed streaks, and for transporting vorticity of the mean shear at the wall away from the wall and for transforming it into more isotropically distributed small scale turbulent vorticity.

In Biasetti et al. (2011) research, it was investigated a correlation between vertical structures with high wall shear stress in patients with abdominal aortic aneurysms (AAAs). It was shown the development of hairpin vertical structure inside of the abdominal aortic aneurysm. For aneurysmatical ascending aorta, the analysis of this criterion has not been studied yet. Therefore, one can believe that the study of coherent structures in flow patterns can help understand how vortex creation can influence aneurysm growth.

Several studies have analyzed the effects of wall shear stress (WSS) and its relation to aortic dilation. It has recently been shown that regions with increased WSS correspond to extracellular matrix dysregulation (Guzzardi et al., 2015) and elastic fiber degeneration, caused by the frictional force acting on the endothelial cell surface (Malek et al., 1999), may contribute to aneurysm's growth. The wall shear stress distribution is considered as an important hemodynamic variable in the genesis of atherosclerotic lesions by several authors (Caro et al., 1971;

Friedman et al., 1981; Ku et al., 1985). Nevertheless, there is not yet sufficient evidence to include these variables for clinical management (Rodríguez-Palomares et al., 2018).

Raghavan et al. (2000) using computational mechanics techniques, analyzed six patients with abdominal aortic aneurysm and one control patient without aneurysm to study the wall stress distribution in three-dimensional reconstructed models. The peak shear stress in the aortic wall in patients with aneurysm was up to four times greater than the shear stress in the patient without the disease. This led to further analysis of other cases investigating the relationship between mechanical factors, aneurysm volume and the shear stress rate, which may lead to aortic rupture.

Thus, a more detailed 3D representation of WSS components would help to explain the different aortic dilatation morphotypes. Bieging et al. (2011) have investigated the WSS dynamics during the cardiac cycle over the entire ascending aortic wall. It was found that AAoA is associated with alterations in WSS and that these alterations correspond to changes in flow patterns and velocities.

According to Cecchi et al. (2011), the change in the shear stress can cause the occurrence of aortic aneurysm, leading to growth or rupture.

It is perceived that the WSS study is fundamental for the understanding of how the AAoA pathology can manifest itself. Bäck et al. (2013) emphasized that aortic aneurysm is a multifactorial and predominantly degenerative process, resulting from a complex interplay between hemodynamic factors and the adaptive biological processes. It is important to take into account biomechanical factors when studying the pathophysiology of aortic wall and aortic valve diseases (Bäck et al., 2013).

Malvindi et al. (2016) performed a pre-dissection computational fluid analysis of an ascending aortic aneurysm associated with unicuspid aortic valve. The analysis showed an abnormal helical flow pattern inside the aneurysm and an increased wall stress on the right posterolateral wall of the ascending aorta. These values were largely higher than the theoretical cut-off for aortic wall dissection, their topographic distribution followed the intimal tear site as subsequently diagnosed by computed tomography scan and confirmed during the operation for dissection repair. The methodology provided the simulation only at peak systole, whereas shear stress changes over the cardiac cycle can also influence the onset of aortic dissection. Malvindi et al. (2016) study is quite unusual, for the reason that they were able to grasp the aneurysm before the rupture has occurred and the ruptured aneurysm was captured intraoperatively. Preoperative computed tomography and

intraoperative findings confirmed the presence of the intimal feature in the WSS area.

Rodríguez-Palomares (2018) analyzed differences in flow patterns and regional axial circumferential WSS maps in 101 patients with bicuspid aortic valve (BAV) and their correlation with ascending aorta dilatation. An increase in aortic wall WSS was observed in patients with AAoA.

Transient simulations capture the pulsality of blood flow. However, steady-state simulations are less computationally expensive, simplified modeling approach that may facilitate the hemodynamic simulation into clinical practice and an efficient alternative to obtain information of the mains flow characterizes and WSS distribution (Geers et al., 2010).

In Morsi (2000) research, experiments with artificial heart valves *in vitro* were carried out to compare steady and pulsatile flow conditions. The comparison made revealed that the steady flow results obtained during peak systole were similar to those found in pulsatile flow experiments with an acceptable degree of accuracy.

According to Jin et al. (2003), the differences in the magnitude of WSS between the rigid and full motion models, while remarkable, are not large, at least at mid-section of the ascending aorta. The streamlines during the acceleration phase of systole are predominantly in the axial direction, and strong secondary patterns develop during systolic deceleration and diastole (Jin et al., 2003).

Benim (2011) has investigated the blood flow in a human aortic arch using computational fluid dynamics, for physiologic and extracorporeal circulation. For the physiologic circulation under the assumption of negligible wall distensibility, it was observed that the time-averaged results of the pulsatile computation do not remarkably differ from those of a steady-state one.

Johnston et al. (2004) and Johnston et al. (2006) analyzed the same 3D geometry of a right coronary artery. The first paper studied the characteristics of steady flow and second one the transient flow. The distributions of wall shear stress found in the steady-state simulations are qualitatively the same as those obtained in the transient simulation for about 70% of the cardiac cycle. The wall shear stress patterns differ most significantly when the flow is either slow or reversing. According to Johnston et al. (2006), this is in agreement with experimental observations (Asakura & Karino, 1990) as well as previous simulations which suggest that cycle averaged wall shear stress patterns are in good agreement with steady flow patterns (Myers et al., 2001; van de Vosse et al., 2001; Feldman et al., 2002).

The majority of fluids found in nature are classified as Newtonian fluids. That

is, the viscous stress tensor is directly proportional to the rate of deformation tensor. All other fluids are classified as non-Newtonian, and they are a large variety of non-Newtonian fluids with different behaviors (Johnson, 1998).

Viscoelasticity is known to be an important rheological property of blood (Thurston et al., 2004). It means that viscosity decreases as the fluid is subjected to a higher shear rate, being called shear-thinning. Attempts to recognize the shear-thinning nature of blood were initiated by Chien et al. (1970). The viscoelastic properties depend on the elastic behavior of red blood cells. Some author believe that a suitable blood model should include non-Newtonian properties of blood (Criscione, 2013), especially for small diameter vessels. However, it does not appear to be a consensus in the literature on the importance of non-Newtonian effects on unsteady flows in large arteries (Johnston et al., 2006). Some studies consider important to include the non-Newtonian rheology of the blood in their studies (Rodkiewicz et al., 1990; Tu & Deville, 1996; Gijsen et al., 1999), while others found that it is relatively unimportant in determining flow patterns in large arteries (Perktold et al., 1989; Ballyk et al., 1994).

Bodnár et al., (2011) describes possible reasons why there is no full consensus on this subject, since none of homogenized models of non-Newtonian fluids can predict the viscoelastic response of blood. Blood cells are essentially elastic membranes filled with a fluid and it seems reasonable, at least under certain flow conditions, to expect blood to behave like a viscoelastic fluid. At low shear rates, erythrocytes aggregate and store elastic energy that accounts for the memory effects in blood. At high shear rates, they disaggregate forming smaller rouleaux, and later individual cells, that are characterized by distinct relaxation times. They lose their ability to store elastic energy and the dissipation is primarily due to the internal friction.

Various non-Newtonian blood models are obtained by parameter fitting to experimental viscosity data obtained at certain deformation rates under steady-state conditions (Walburn & Schneck, 1976; Cho & Kensey, 1991; Ballyk et al., 1994). In some deformation rate ranges is acceptable to approximate the blood as Newtonian. If deformation rate does not exceed a limiting value, the blood behaves like a Newtonian fluid. This limiting value of deformation rate, which determines the blood apparent viscosity, is a function of a large quantity of factors as it was described above. In literature, the limiting value of deformation rate is not yet properly assessed. As reported by Stuart & Kenny (1980), the blood behaves like a Newtonian fluid when the deformation rate varies above 50 s^{-1} (Long et al., 2004).

According to Crowley & Pizziconi (2005), at deformation rates lower than

$50s^{-1}$, the viscosity of blood increases exponentially due to the formation of large aggregates of erythrocytes. As shear rate increases, the erythrocytes are dispersed and aligned in the direction of the flow (Stuart & Kenny, 1980). Consequently, the use of a Newtonian fluid is often justified on the grounds that blood hemolysis is a result of strong shear flows and turbulence, which are characterized by high shear rates (Deutsch et al., 2006), and can be found in patients with AAoA (Simão et al., 2017).

Finally, it is worth mentioning the high fidelity of the results obtained by Gomes (2017) and Cellis (2017) using a Newtonian fluid flowing inside an aorta to study the ascending part. While the former employed experimental techniques, the latter investigated the problem numerically. The numerical methodology was validated by comparing with the experimental data of the former obtained with particle image velocimetry (PIV).

3
MODELING

As mentioned, the objective of this work is to investigate numerically the flow path through the ascending aorta of different patients, aiming to identify some flow characteristic that might be associated with the growth of an ascending aortic aneurysm (AAoA). To this end, it is necessary to define a computational domain that corresponds to each patient aorta. To analyze the blood flow, i.e., to determine pressure and shear stress distribution, as well as to examine the flow structure, one must solve the governing equations of mass and momentum.

In order to evaluate the flow through the aorta of different patients at different times in a systematic way, a methodology was created subdivided into three stages, which are detailed in the subsequent sections. First, it is presented the method used to obtain the three dimensional geometry model used in this research. Then, the hypotheses and conservation equations to determine the flow are discussed. Finally, the numerical method employed for solving these equations is described.

3.1. 3D Modeling of the Patient's Aorta

Six patients with ascending aortic aneurysm were selected to be investigated. The research is registered in the National Council of Ethics in Research from Ministry of Health and was approved by the Research Ethics Committee of the National Institute of Cardiology. The geometry was built based on computerized tomography angiography (CTA) scan of each patient in two different years. Four of the patients had been diagnosed with aortic aneurysm growth and two with no aortic aneurysm growth between the time intervals of the exams.

The CTA images were obtained with a 64-slice scanner SOMATOM Sensation 64 (Siemens, Germany). The selected CTA slices (DICOM format) spanned from the aortic annulus to the thoracic aorta. In order to verify the quality of the images and the diameter of the aortic valve, the images were first examined with the Synedra View Personal software (Synedra, Austria) (Figure 3.1). Synedra is a versatile intuitive viewer suitable for applications such as clinical imaging and diagnostic imaging.

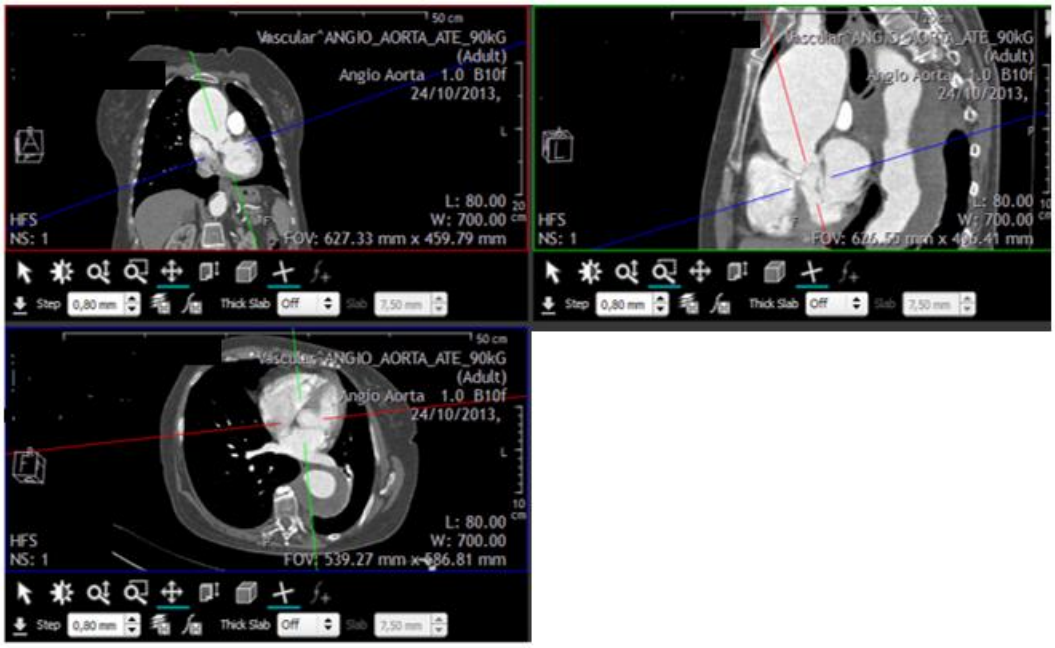

Figure 3.1 – CTA slices views with Synedra View Personal

The DICOM images were transferred to the software FIJI (Fiji is Just ImageJ), which is distributer of the popular open-source software ImageJ, focused on biological-image analysis (Schindelin et al., 2012). Information such as pixel size and distance slice were harvested, to further adjust the aorta model in 3D with its actual size (Figure 3.2). The values acquired in this process are shown in Table 3.1.

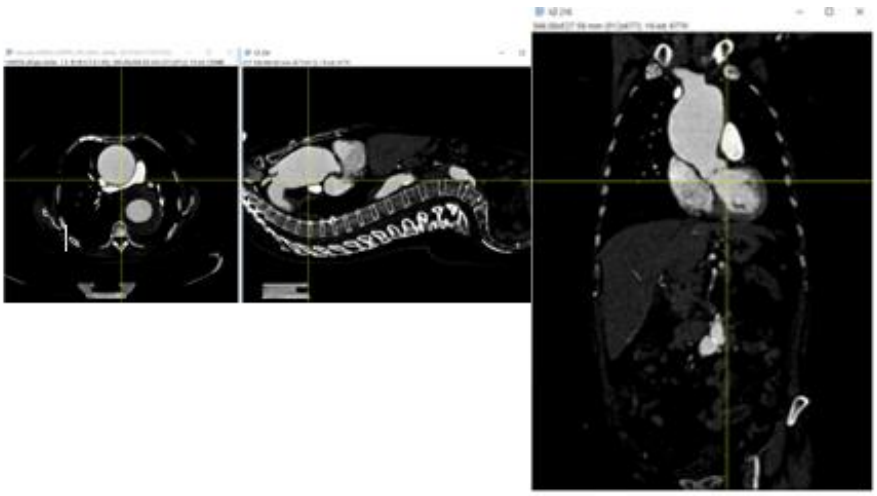

Figure 3.2 – Step to collect slice distance at Fiji

Table 3.1 – Example of slice distance and pixel size

Slice	Scale (pixels/mm)	z (mm)	Slice Distance (mm/slice)	Pixel Size (mm/pixels)
659	1.28	527.58	0.80	0.78

A sequence of commands is required in order to separate the object of interest, which is the aortic region. In Figure 3.3 (a), the yellow square shows a select area that incorporates the aorta (ascendant part is the biggest circle and descendant part the small one). Figure 3.3 (b) displays just the area selected, while in Figure 3.3 (c), the segmented aorta is shown, which means, the aorta was separated from all other objects that are not part of this study.

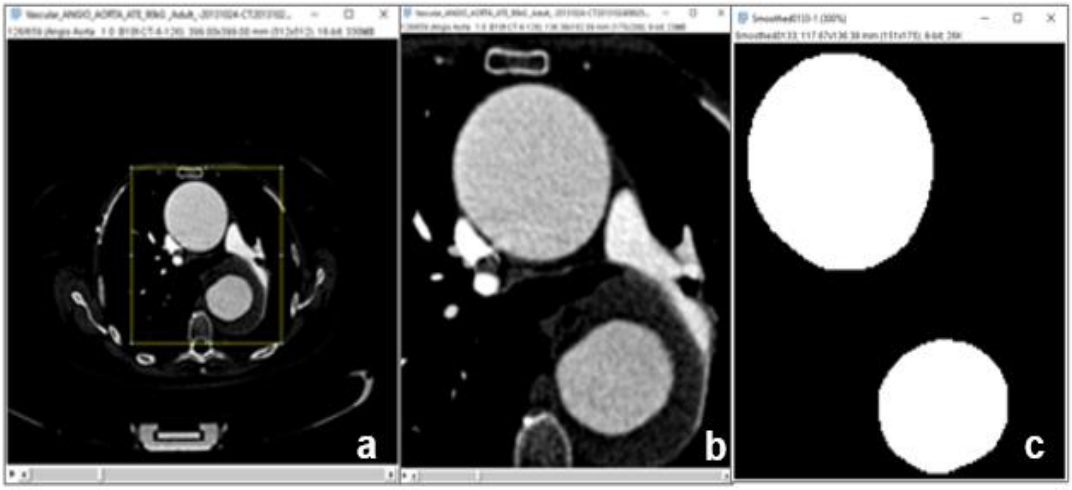

Figure 3.3 – (a) All images transferred to Fiji (b) Aortic region selected (c) Segmented aorta.

The segmented images were sent to Mimics software (Materialise, Belgium) aiming to transform the slices into a 3D object. Information such as pixel size and slice distance, shown in Table 3.1, and the orientation of aorta, shown in Figure 3.4, were given as information to adjust the 3D object in to this real size.

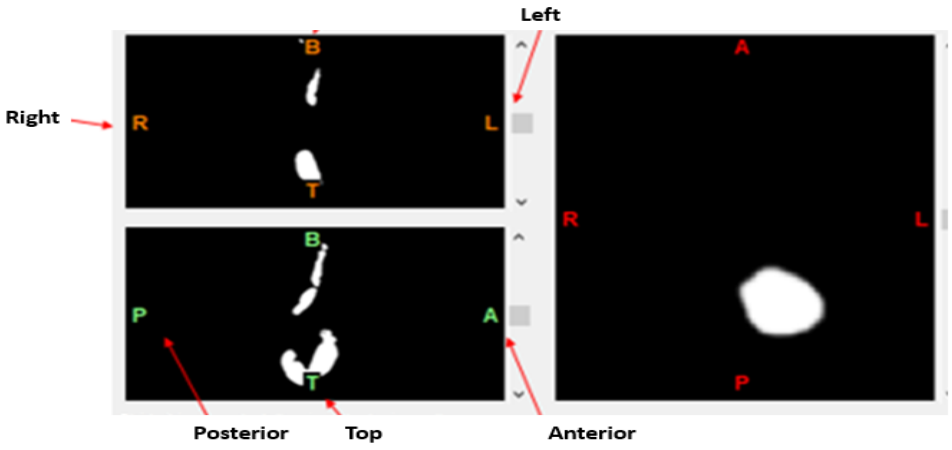

Figure 3.4 – Orientation of the object

Figure 3.5 is an example of a three-dimensional (3D) aortic model after all the procedures discussed above. It is composed by the ascending aorta ; the aortic arch, which is connected to the brachiocephalic, left common carotid and left subclavian arteries at the upperpart; and finally a portion of descending aorta.

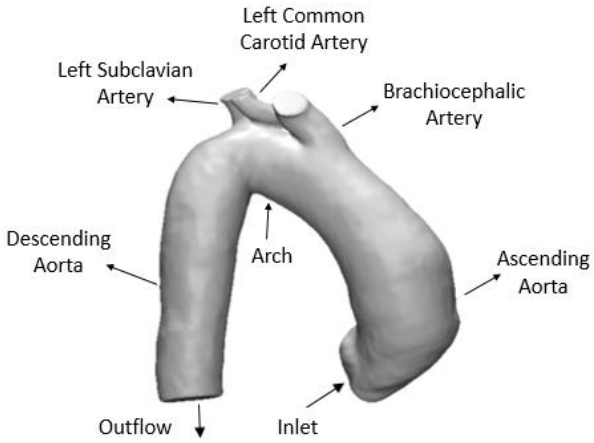

Figure 3.5 – 3D aorta

As a final procedure to create the computational domain, it was necessary to define a criterion to compare the aortas in different years, since the quality of the exams was not exactly the same (due to process variability) and possible modifications of aorta geometry caused by the growth of the aortic aneurysm. So, the 3D models were first superposed, aiming the beginning of the brachiocephalic trunk, Figure 3.6 (a), and right coronary, Figure 3.6 (b) overlap. In these figures, the aorta corresponding to the first year is gray, while the aorta of the same patient corresponding to the posterior exam is blue. Once the arteries were overlapping, the aortic valve and the descending part were sliced, Figure 3.6 (c), ensuring that the inflow and outflow sections had the same spatial reference.

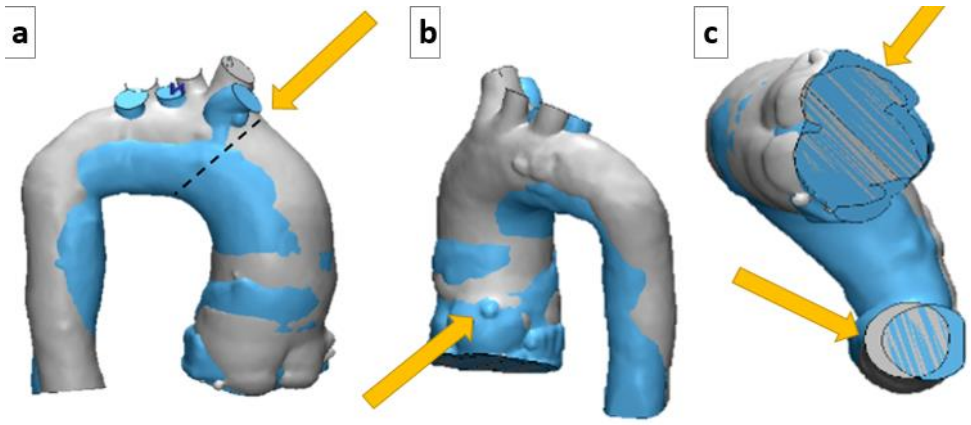

Figure 3.6 – Criteria of comparison between aortas of the same patient in different years: (a) The dashed line indicates the beginning of the brachiocephalic trunk; (b) right coronary overlapped; (c) Aortic valve and descending part sliced.

3.2. Mathematical Modeling

To model the aorta and to determine the flow field through it, several hypotheses were made in order to simplify the problem, allowing to obtain a solution with a reasonable computing effort, but at the same time, accurate enough to ensure the solution´s quality.

As mentioned in Chapter 2, the human heart consists of four chambers: the left side and the right side each have one atrium and one ventricle. Each of the upper chambers, the right atrium and the left atrium, acts as a receiving chamber and contracts to push blood into the lower chambers, the right ventricle and the left ventricle. The ventricles serve as the primary pumping chambers of the heart, propelling blood to the lungs and aorta (Betts, 2013).

This movement of filling and emptying the ventricles makes the heart works like a pump in a periodic cycle, known as the cardiac cycle. Figure 3.7 illustrates the volumetric flow rate entering the aorta, during the cycle, where two different behaviors can be identified. The first part of the period is called systole, and it corresponds to the period where blood is ejected from the heart into the aorta. During this period, a ventricular contraction occurs, the pressure in the ventricles increases abruptly, causing the opening of the aortic valve, resulting in an inflow of blood to the aorta, until it reaches a maximum flow rate (indicated Fig. 3.7). With the emptying of the ventricle, the intraventricular pressure decreases and the aortic valve closes, causing a steep drop in the flow rate.

The focus of the present study is to analyze the flow during ventricular systole. In this period, the maximum distension of the aortic wall occurs, obtaining its greater diameter and with the less complacency.

Following the works of several researches, as described in Chapter 2, three major hypotheses were made to analyze the differences in the flow field inside the aorta of patients with and without aneurysm, examining the flow in the aorta of the same patient in two different years.

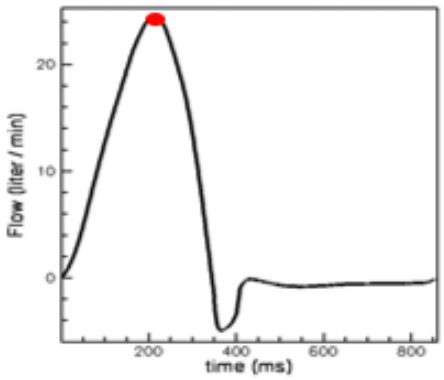

Figure 3.7 – Cardiac cycle at the inlet. Adapted from (Borazjani et al., 2008)

The first one was to assume that the pulsatile flow can be represented by a succession of stationary states at different instants of pulsatile cycle. As presented along the literature review, several authors like Morsi (2000); Geers et al. (2010) and Benim (2011), have shown that similar results are obtained when steady flow results are compared with pulsatile flow. With this assumption, one can analyze the problem, neglecting the time variation of the flow, focusing in the critical mass flow rate condition, corresponding to the maximum volumetric flow rate, Q_{in}, equal to 25 lt/min, which is the peak of systole, when the aortic wall is submitted to the largest mechanical stresses.

The second important hypothesis adopted here was to consider the aortic wall rigid. This can be justified by remembering that during the peak of the ventricular systole, the maximum distension of the aortic wall occurs, resulting in a greater diameter with less complacency. As a result, small differences have been observed in the magnitude of WSS between the rigid and full motion models in the aortas´s ascending region (Jin et al., 2003). The aortic complacency may be important when the entire cardiac cycle is studied. However, in this work, the critical situation is being investigated, which corresponds to the peak of the systole.

The third significant hypothesis employed in this study was to consider the blood as a Newtonian fluid. According to the literature, blood behaves as a Newtonian fluid for large deformation rates, above 50 s^{-1} (Stuart & Kenny, 1980, Long et al, 2004, Crowley & Pizziconi, 2005). At values of shear rate below 50 s^{-1}, blood behaves as non-Newtonian fluid (Stuart & Kenny, 1980) and the apparent viscosity of blood increases exponentially due to a reversible aggregation of red cells known as rouleaux formation (Long et al., 2004).

It is well known that the blood viscosity is strongly influenced by the volume percentage of red blood cells in whole blood (hematocrit). The viscosity increases when hematocrit increases and/or temperature decreases (Barbee, 1973). During

blood flow, depending on the shear stress, disaggregation of the rouleaux (stacks of red blood cells) can occur, modifying the orienting of individual red blood cells (Soares et al., 2017). This ratio explains why the viscosity of the blood approaches a minimum on *in vivo* arterial flow rates, while reaches maximum levels in the venous circulation (Simmonds et al., 2013).

In Figure 3.8, is possible to analyze the effect of shear rate on blood viscosity. For values above 50 s^{-1} it is possible to visualize the blood viscosity becoming approximately constant. Shear rate (or deformation rate) is defined as the ratio of the velocity difference between two points, divided by the distance between the points (Pop et al., 2002). Its dimension is (cm/s)/cm or simply s^{-1} and it is proportional to flow rate in a tube (e.g., blood vessel). The lower shear rates correspond to the circulatory conditions in the venous circulation while higher shear rates characterize the arterial vessels. For the maximum mass flow rate, elevated deformation rates are obtained, and the viscous stress is directly proportional to the rate of deformation of the fluid element, justifying the validity of the Newtonian fluid hypothesis, as also discussed by Sun & Chaichana (2016).

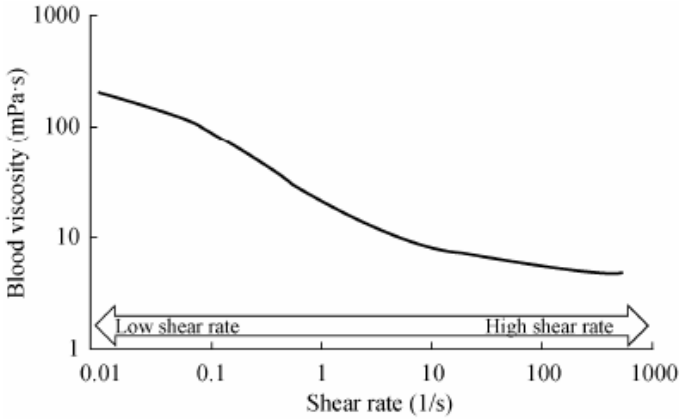

Figure 3.8 – The effect of shear rate on whole blood viscosity (Simmonds et al., 2013)

Others hypotheses considered were: (i) isothermal flow, since the body temperature is approximately constant (Hao, 2010). (ii) incompressible fluid, since under normal conditions at 37°C, the blood is quite similar to water and its compressibility can be neglected (Feijoo & Zouain, 1988; Li, 2004). (iii) constant molecular viscosity (Ranucci et al., 2014; Gomes, 2017; Gunning et al., 2014; Bunchmann et al., 2011). (iv) negligible gravity effects, since pressure variations are dominant over the force of gravity.(v) negligible flow rate through the coronaries, due to small flow during the systole period (Yoganathan et al., 1988; Suo et al., 2003).

Depending on the inertia force in comparison with the viscous force, the flow

can be behave as laminar or turbulent. When viscous forces are high, perturbations are damped and the flow behaves as laminar, with smooth variations. However, when the inertia forces dominate, perturbations are amplified, inducing the formation of vortices with a large variety of sizes, presenting a 3D and transient behavior. The ratio of these two forces can be measured by the Reynolds number

$$Re = \frac{\rho\ W_{in}\ D}{\mu} = \frac{4\ \rho\ Q_{in}}{\pi\ D\ \mu} \tag{3.1}$$

where ρ is the density, μ is the molecular viscosity, D is the inlet valve diameter, which is the effective valve diameter, i.e., the effective orifice that the jet pass through the valve (Flachskampf et al., 1990), W_{in} is the inlet normal velocity, Q_{in} is the inlet volumetric flow rate.

For the maximum systole flow rate selected to be studied, the inlet jet flow through the aorta´s orifice (Re > 2000), behaves like a turbulent jet (Sallam & Hwang, 1984; Davies et al., 1986), as measured by Gomes (2017), who studied the flow field inside an aorta´s model of a patient. Further, Celis Torres (2017) compared the turbulent numerical prediction for the same aorta´s presenting reasonable agreement.

To analyze a turbulent flow, there are different approaches with different levels of accuracy and computational effort: Reynolds-Averaged Navier-Stokes (RANS), Large-eddy simulation (LES) and Direct numerical simulation (DNS) (Pope, 2000).

DNS simply means directly solving the momentum and continuity equations without introducing any model, capturing all length and time scales present in the flow. Therefore, to apply this methodology, a very fine mesh must be specified with very small time steps. High order numerical schemes must be employed. The results are accurate, but with very large computing demand, not only time consuming, but the simulation requires large computer memory. In the present days, this approach is mainly applied to simple geometries, relatively low Reynolds number, focusing to understand the turbulent phenomena to help improved RANS and LES models.

LES is a computation where large vortexes (eddies) are computed directly, while small scale eddies are modeled, allowing to employ smaller number of grid points in relation to DNS. Consequently, LES is much more economical in terms of computational power required than DNS, but it is not as accurate. RANS offers the most economical approach for computing complex turbulent flows, and it is currently the most popular model employed by the industry. However, it must be

validated for each application.

RANS approach is based on the Reynolds average definition, i.e., any generic variable ϕ (like pressure or velocity) varies in a random form around a mean value Φ, as shown in Figure 3.9, and only the mean value is determined

$$\phi = \Phi + \phi' \quad ; \qquad \Phi = \frac{1}{\Delta t}\int_{\Delta t} \phi \, dt \tag{3.2}$$

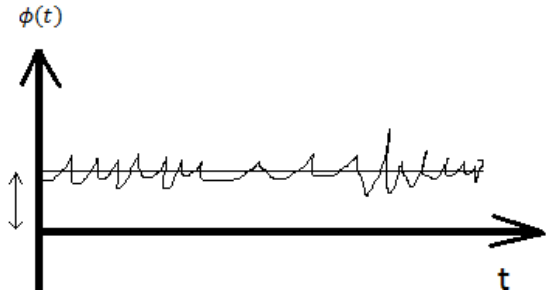

Figure 3.9 – Schematic variation of a random variable

To determine the mean flow field, time average conservation equations are solved. These equations are obtained by applying the Reynolds average (Eq. 3.2) to the original conservation equations. RANS approach models all scales, and requires additional closing equations to determine the turbulent shear stress, also called Reynolds stress. To define the Reynolds stress, a large variety of models are based on the Boussinesq approximation (Pope, 2000), which employs the concept of turbulent viscosity. Additional models are then defined to determine the turbulent viscosity, varying from one-equation models to n-equation models.

Over the years, several turbulence models have been proposed like $\kappa - \varepsilon$, originally proposed by Harlow & Nakayama (1968) and later by Jones & Launder (1972). Additional two-equation models have been proposed, most of which use the kinetic energy, κ, as one of the variables with a variety of choices for the second variable. Perhaps the most common of these is the $\kappa - \omega$ model proposed in 1988 by (Wilcox, 1988). A variation on the standard $\kappa - \omega$ model is the shear-stress-transport (SST) developed by (Menter, 1994). This model takes advantage of accurate formulation of the $\kappa - \omega$ model in the near-wall region with the free-stream independence of the $\kappa - \varepsilon$ model in the far field (Smith et al., 2017). This model is recommend for low Reynolds number situations, and was selected based of experimental data of Gomes (2017) and numerical investigation of Celis Torres (2017).

3.2.1. Conservation Equations

Based on the hypotheses presented in the previous section, the time average conservation of mass equation, also called continuity equation can be written for an incompressible fluid as

$$\frac{\partial u_i}{\partial x_i} = 0 \tag{3.3}$$

where x_i corresponds to coordinate direction *i* and u_i is the time average (mean) component of the velocity vector in the *i* direction.

The Reynolds Average Navier-Stokes, i.e., the time-average momentum conservation equation for a Newtonian fluid, considering the flow as steady flow, incompressible fluid and negligible gravity, can be written as

$$\frac{\partial \rho u_j u_i}{\partial x_j} = -\frac{\partial p}{\partial x_i} + \frac{\partial \tau_{ij}}{\partial x_j} - \frac{\partial \rho \overline{u_j' u_i'}}{\partial x_j} \tag{3.4}$$

where ρ is the density, p the pressure , τ_{ij} the viscous stress tensor, and $-\rho\overline{u_j' u_i'}$ the Reynolds stress tensor. The viscous stress tensor is always symmetric. For an incompressible Newtonian fluid is

$$\tau_{ij} = \mu 2 S_{ij} \tag{3.5}$$

where μ is the molecular viscosity, and S_{ij} is the strain rate tensor (or rate of deformation tensor, given by the symmetric part of the velocity gradient)

$$S_{ij} = \frac{1}{2}\left[\frac{\partial u_i}{\partial x_j} + \frac{\partial u_j}{\partial x_i}\right] \tag{3.6}$$

To model the Reynolds stress tensor, the Boussinesq approximation can be used, i.e, the turbulent stress is analogous to the viscous stress. In that way, the proportionality coefficient is replaced by the turbulent viscosity μ_t , which depends on the flow. For an incompressible fluid is

$$\rho\overline{u_j' u_i'} = \mu_t 2 S_{ij} - \frac{2}{3}\rho\kappa\delta_{ij} \tag{3.7}$$

The last term in the equation above represents the turbulent dynamic pressure, where κ is the turbulent kinetic energy, defined as

$$\kappa = \frac{1}{2}\overline{u_i' u_i'} \tag{3.8}$$

Substituting the Reynolds stress tensor and the constitutive equation in the momentum equation, one obtains

$$\frac{\partial \rho u_j u_i}{\partial x_j} = -\frac{\partial \hat{p}}{\partial x_i} + \frac{\partial}{\partial x_j}\left[(\mu + \mu_t)\left(\frac{\partial u_i}{\partial x_j} + \frac{\partial u_j}{\partial x_i}\right)\right] \tag{3.9}$$

where $\hat{p}$ is a modified pressure, which include the turbulent dynamic pressure

$$\hat{p} = p + \tfrac{2}{3}\rho\kappa \tag{3.10}$$

3.2.1.1. Turbulence Model

In order to determine the turbulent viscosity, the $\kappa - \omega$ SST model proposed by Menter (1994) was selected. The two-equation eddy-viscosity model with the shear stress transport (SST) formulation combines two of the best approaches in turbulence models. It is possible to integrate the robust and accurate formulation of the $\kappa - \omega$ model in the near wall region with the free-stream independence of the $\kappa - \varepsilon$ model in the far field. To achieve this, the $\kappa - \varepsilon$ model is converted into a $\kappa - \omega$ formulation.

The $\kappa - \omega$ SST turbulent eddy viscosity is computed from

$$\mu_t = \frac{\rho\kappa}{\omega}\xi \tag{3.11}$$

where ξ is a blending factor between $\kappa - \varepsilon$ and $\kappa - \omega$

$$\xi = \frac{1}{\max(1/\alpha^*, SF_2/(a_1\omega))} \tag{3.12}$$

S is the magnitude of the strain rate tensor

$$S = \sqrt{2S_{ij}S_{ij}} \tag{3.13}$$

α^* and F_2 are defined as

$$\alpha^* = \alpha_\infty^*\left(\frac{\alpha_0^* + \mathrm{Re}_t/\mathrm{Re}_\kappa}{1 + \mathrm{Re}_t/\mathrm{Re}_\kappa}\right) \tag{3.14}$$

$$F_2 = \tanh\left(\Phi_2^2\right) \quad ; \quad \Phi_2 = \max\left[2\frac{\sqrt{\kappa}}{0.09\omega y}, \frac{500\mu}{\rho y^2 \omega}\right] \tag{3.15}$$

being *y* the distance from the wall and the turbulent Reynolds number Re_t given as

$$\mathrm{Re}_t = \frac{\rho\kappa}{\mu\omega} \tag{3.16}$$

The empirical constants of the equations are: $a_1 = 0.31$; $\alpha_\infty^* = 1$; $\alpha_o^* = \beta_i / 3$; $\mathrm{Re}_\kappa = 6$, and

$$\beta_i = F_1\beta_{i,1} + (1 - F_1)\beta_{i,2} \tag{3.17}$$

$$F1 = \tanh\left(\Phi_1^4\right) \quad ; \quad \Phi_1 = \min\left\{\max\left[\frac{\sqrt{\kappa}}{0.09\omega y}, \frac{500\mu}{\rho y^2 \omega}; \frac{4\rho\kappa}{\sigma_{\omega,2} D_\omega^+ y^2}\right]\right\} \tag{3.18}$$

$$D_\omega^+ = \max\left[\frac{2\rho}{\omega\sigma_{w,2}}\frac{\partial\kappa}{\partial x_j}\frac{\partial\omega}{\partial x_j}, 10^{-10}\right] \tag{3.19}$$

with $\beta_{i,1} = 0.075$; $\beta_{i,2} = 0.0828$ and $\sigma_{\omega,2} = 1.168$.

To obtain κ and ω, their conservation equations need to be solved (Menter, 1994)

$$\frac{\partial(\rho u_j \kappa)}{\partial x_j} = \tilde{P}_\kappa - \rho\beta_i^* \omega\kappa + \frac{\partial}{\partial x_j}\left[\left(\mu + \frac{\mu_t}{\sigma_\kappa}\right)\frac{\partial\kappa}{\partial x_j}\right] \tag{3.20}$$

$$\frac{\partial(\rho u_j \omega)}{\partial x_j} = \frac{\rho\alpha}{\mu_t}P_\kappa - \rho\beta_i\omega^2 + \frac{\partial}{\partial x_j}\left[\left(\mu + \frac{\mu_t}{\sigma_\omega}\right)\frac{\partial\omega}{\partial x_j}\right] + 2(1 - F_1)\frac{\rho\sigma_{\omega 2}}{\omega}\frac{\partial\kappa}{\partial x_j}\frac{\partial\omega}{\partial x_j} \tag{3.21}$$

where

$\tilde{P}_\kappa$ is the limited production of turbulent kinetic energy P_κ

$$\tilde{P}_\kappa = \min\left(P_\kappa;\ 10\rho\beta_i^*\omega\kappa\right) \qquad P_\kappa = -\rho\overline{u_j u_i}\frac{\partial u_i}{\partial x_j} = \mu_t S^2 \tag{3.22}$$

and the adjustment parameter, β_i^*

$$\beta_i^* = \beta_\infty^*\left(\frac{4/15 + \left(\mathrm{Re}_t/\mathrm{Re}_\beta\right)^4}{1 + \left(\mathrm{Re}_t/\mathrm{Re}_\beta\right)^4}\right) \tag{3.23}$$

The empirical constants are: $\beta_\infty^* = 0.09$ and $\mathrm{Re}_\beta = 8$. The turbulent Prandtl

number for κ and ω are:

$$\sigma_\kappa = \left[F_1/\sigma_{\kappa,1} + (1-F_1)/\sigma_{\kappa,2}\right]^{-1} \qquad \sigma_\omega = \left[F_1/\sigma_{\omega,1} + (1-F_1)/\sigma_{\omega,2}\right]^{-1} \tag{3.24}$$

being $\sigma_{\kappa,1} = 1.176$; $\sigma_{\kappa,2} = 1.0$ and $\sigma_{\omega,1} = 2.0$. Finally, the α parameter of the ω production is

$$\alpha = \frac{\alpha_\infty}{\alpha^*}\left(\frac{\alpha_0 + \mathrm{Re}_t/\mathrm{Re}_\omega}{1+\mathrm{Re}_t/\mathrm{Re}_\omega}\right) \qquad \alpha_\infty = F_1\alpha_{\infty,1} + (1-F_1)\alpha_{\infty,2} \tag{3.25}$$

$$\alpha_{\infty,1} = \frac{\beta_{i,1}}{\beta^*_\infty} - \frac{k^2}{\sigma_{\omega,1}\sqrt{\beta^*_\infty}} \qquad \alpha_{\infty,2} = \frac{\beta_{i,2}}{\beta^*_\infty} - \frac{k^2}{\sigma_{\omega,2}\sqrt{\beta^*_\infty}} \tag{3.26}$$

where $k = 0.41$ and $\mathrm{Re}_\omega = 2.95$.

3.2.2. Boundary Conditions

To solve the differential equations presented, it is necessary to define the system of coordinates and the boundary conditions. Figure 3.10 shows two views of the geometry detailing the axes of reference system used.

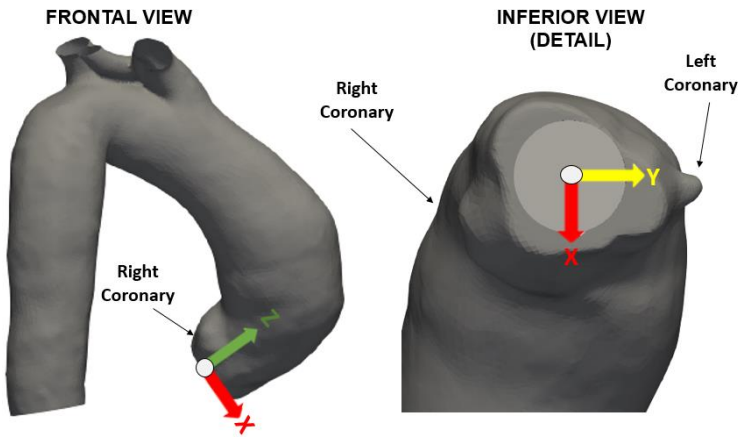

Figure 3.10 – Reference system

The domain of interest in the present analysis is given by the contour of the 3D model, presented in Figure 3.11. The blood flow from the heart enters the aorta through the aortic valve (Input), with effective diameter *D*. Part of the blood leaves to the upper arteries - brachiocephalic trunk (Output 2), left common carotid artery (Output 3) and left subclavian artery (Output 4) - and the rest flows through the descending part of the aorta (Output 1). The external boundary of the computational domain is the inner layer of the aorta, which is referred as aortic wall

and was considered rigid. The effective diameter of aortic valve varied for each patient.

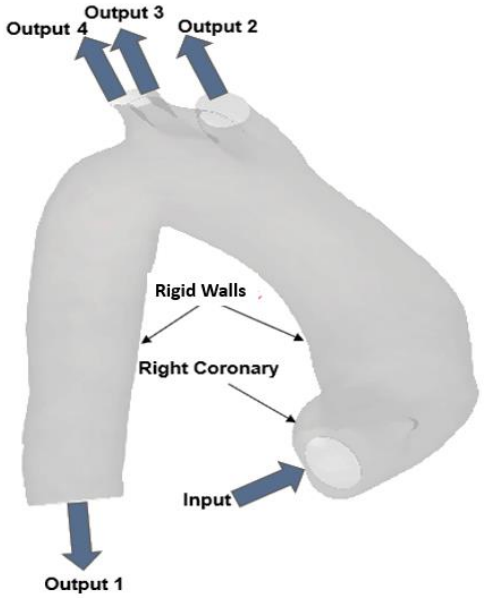

Figure 3.11 – Reference to define boundary conditions

At the input, the volumetric flow rate Q_{in} is defined with an uniform velocity profile. The inlet plane is perpendicular to the axial z coordinate and coincident to x-y plane. Thereby, the normal velocity component of the input plane, which is intrinsically the average inflow velocity, is defined as:

$$w_{in} = w_m = \frac{4\,Q_{in}}{\pi\,D^2} \tag{3.27}$$

At the inlet, the turbulent quantities κ_{in} and ω_{in} are also considered uniform. The turbulent kinetic energy, κ_{in}, is based on the inlet velocity and the turbulent intensity *I*.

$$\kappa_{in} = \frac{3}{2}(w_{in} I)^2 \tag{3.28}$$

The turbulence intensity was estimated based on the inlet Reynolds number (Eq. 3.1) as follows (Fluent Inc., 2018) :

$$I = 0.16\,\mathrm{Re}^{-1/8} \tag{3.29}$$

The specific dissipation, ω_{in}, is based on the empirical constant $C_\mu = 0.09$, and on a length scale ℓ, which was defined equal to the inlet diameter, $\ell = D$

$$\omega_{in} = \frac{\sqrt{\kappa_{in}}}{C_{\mu}^{1/4}\ell} \tag{3.30}$$

There are four outputs, as shown at Figure 3.11. At all output regions, a null diffusive flow condition was applied.

$$\frac{\partial}{\partial x_n} = 0 \tag{3.31}$$

being *n* the direction normal to the outflow plane.

At the aorta's surface, a non-slip condition was specified as a boundary condition:

$$u = v = w = 0 \tag{3.32}$$

The boundary condition of κ at the solid surface is also zero. Nonetheless, the boundary condition for the specific dissipation in the walls is given, according to Menter (1994),as a function of its dimensionless value defined as:

$$\omega^{+} = \frac{\omega_w \mu}{\rho(u^*)} \tag{3.33}$$

being u^* the friction velocity, defined as

$$u^* = \sqrt{\frac{\tau_w}{\rho}} \tag{3.34}$$

Where τ_w is the normal tangential gradient to the wall and ρ is the density. The dimensionless specific dissipation ω^{+} is evaluated taking into account the thickness of the molecular sub layer, characterized as

$$\omega^{+} = \min\left(2500, \frac{6}{\beta_{\infty}^{*}(y^{+})^2}\right) \tag{3.35}$$

where y^{+} is the dimensionless wall distance

$$y^{+} = \frac{\rho\, u^* y}{\mu} \tag{3.36}$$

Since the fluid was characterized as incompressible, the pressure level is not relevant. The solution was obtained as a function of a reference pressure defined

at the inlet, p_{in}, at the center of the aortic valve, which in turn is the geometric origin of the inlet plane.

3.3. Numerical Model

The conservation of mass, conservation of momentum and turbulence equations that delineate the study were solved using the finite volume method provided by the ANSYS Fluent software v18.1 (Fluent Inc.).

The Finite Volume Method (Patankar, 1980) is a discretization method, which guarantees global conservation of all variables of interest and therefore is highly recommended to solve fluid flow problems. The method consists on dividing the computational domain is small control volumes with an inner point called node. The discretized equations are obtained by integrating the differential equations on each control volume, and by applying different schemes to estimate the convective and diffusive fluxes through the control volumes faces, as well as source terms of the resulting balance equation (Tanyi & Thatcher, 1996; Maliska, 1995).

The mesh used in this work was not uniform, in other words, the control volumes sizes were smaller in regions of step gradients and courser otherwise. In this way, a smaller total number of grid points was employed, reducing the computational effort, without compromising the accuracy. More accurate results were generated in the fine-mesh regions where the parameters to be calculated have marked spatial variations. In regions where the parameters to be calculated undergo softer spatial variations, a courser mesh was defined, allowing to reduce the computational time.

The liquid flux through each control volume face has a convective and diffusive contribution. In order to estimate the flux, the power-law differencing scheme of Patankar (1980) was selected for all differential equation, due to its good accuracy and specially its stability characteristics (Vertsteeg & Malalasekera, 1995).

The Pressure-Velocity Coupling, that solves all momentum and turbulent quantities equations in a sequential form, and the pressure field is obtained to enforce mass conservation, was solved using the SIMPLE scheme. The acronym SIMPLE stands for Semi-Implicit Method for Pressure-Linked Equations. The algorithm was originally developed by Patankar and Spalding (1972) and consists a guess-and-correct procedure for the calculation of pressure by combining mass and momentum conservation equations (Vertsteeg & Malalasekera, 1995).

The system of algebraic conservation equation of each variable was solved with the Gauss-Seidel Line-by-Line, also called TDMA line-by-line (Patankar, 1980). The solution procedure consists in choosing a line of the computational mesh, which assumes known the values of the variable along the neighboring lines, and subsequently, a line chosen is solved directly with the TDMA method. The procedure is then repeated for all lines in a given direction until the results are converged. To accelerate convergence the additive multigrid method (Hutchinson & Raithby, 1986) was also considered.

Due the fact that conservation equations are non-linear, sub-relaxation was employed. Appropriate sub-relaxation factors decrease the oscillations of the variables. The sub-relaxation parameters were defined as: 0.7 for the momentum, 0.8 for the Turbulent Kinetic Energy (κ) and 0.8 for Specific Dissipation Rate (ω). The system was considered converged when the residual of all differential equations were inferior to 10^{-6}.

4
RESULTS AND DISCUSSION

This chapter reports results from the CFD analysis of three-dimensional aortic models from six different patients in two different times. The patients selected have been classified as having ascending aortic aneurysm with non-surgical indication. They were selected based on medical evaluation and exams of computational angiotomography, performed at the National Institute of Cardiology - Ministry of Health.

For each patient, two computational models were created, corresponding to each year and the flow field was numerically determined. The aorta´s geometry for each year was defined based on the exams, and it was considered that the aortic valve diameter did not vary during the time span between exams. It may be considered a limitation in the study, since calcifications may occur inside the aortic valve, do not behaving as a perfect circle. Respectively, each patient presented a different effective aortic valve diameter, as shown at Table 4.1. These diameters are the average of three measurements of the two different years of exam. The measurements from the digital images was made by the same examiner, with the expertise of the physicians who provided the exams.

Table 4.1 – Diameter of the effective aortic valve of each patient

Patient	**1**	**2**	**3**	**4**	**5**	**6**
Diameter (mm)	22.7	29.2	26.2	28.0	28.2	33.2

It was considered that no patient had previous disease or would be using some type of drug. In this way, typical values of dynamic viscosity and density found in the literature for in vitro simulations of blood flow (Gomes, 2017; Gunning et al., 2014; Bunchmann et al., 2011) were employed in the present analyzes. In this way, the dynamic viscosity was set as $\mu = 7.2\, cP$ and density as $\rho = 1054\ kg/m^3$.

The flow rate Q_{in} in the entry was defined as 25 lt/min, which corresponds to the maximum volumetric flow rate at systolic period.

With these parameters, the inlet Reynolds number varied from 2267 to 3421, indicating turbulent flow (Re > 2000). The inlet turbulent intensity was established as 5%, as indicated by Celis Torres (2017) and Salazar et al. (2008).

Since the fluid was considered incompressible and a steady state simulation was performed, the inlet flow rate must be equal to the sum of all outflow. For all cases, the same outlet flow rate distributions (percentage of the inflow) were imposed based on average values in the human body, according to Alastruey et al. (2017). Figure 4.1 presents the outflow boundary condition at the descending aorta (output 1 – 69.1%), the brachiochephalic artery (output 2 – 19.3%), left carotid artery (output 3 - 5.2%) and left subclavian artery (output 4 – 6.4%).

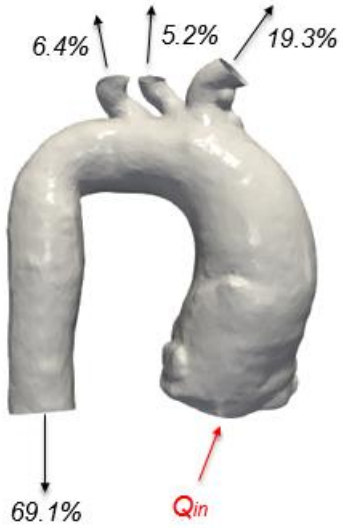

Figure 4.1 – Percentage of outflow distribution

The aorta has a very complex geometry and all relevant geometric details must be well represented to generate a reliable solution. A mesh must be defined to provide a correct solution in all points. To determine the mesh, a grid test was performed (presented in Appendix A1 in order to facilitate the read), aiming to obtain a mesh independent solution. Based on the grid test results, a domain with 400.000 nodes was applied to all the cases studied in the present work.

To visualize the internal fields, a central plane, normal to the inlet plane and oriented perpendicular to the right coronary artery was select for each patient, as shown in Figure 4.2 (a) and Figure 4.2 (b). According to Figure 4.2 (a), the left wall corresponds to the posterior wall of the aorta and the right wall is referred as anterior wall. To aid the analysis of the flow field, planes parallel to the inlet plane were also defined. These transverse planes were distributed every 10 mm from the entrance, covering 60mm of ascending aorta, as displayed in Figure 4.2 (c).

To generalize the results, it is convenient to normalize the flow variables. The selected reference variables were the inlet axial velocity w_{in} and inlet valve diameter *D.* The system coordinates, velocity, pressure and turbulent quantities were normalized as

$$X_i = \frac{x_i}{D} \;\; ; \;\; U_i = \frac{u_i}{w_{in}} \;\; ; \;\; P = \frac{p - p_{in}}{\rho w_{in}^2/2} \;\; ; \;\; K = \frac{\kappa}{w_{in}^2} \;\; ; \;\; \Omega = \frac{\omega D}{w_{in}} \tag{4.1}$$

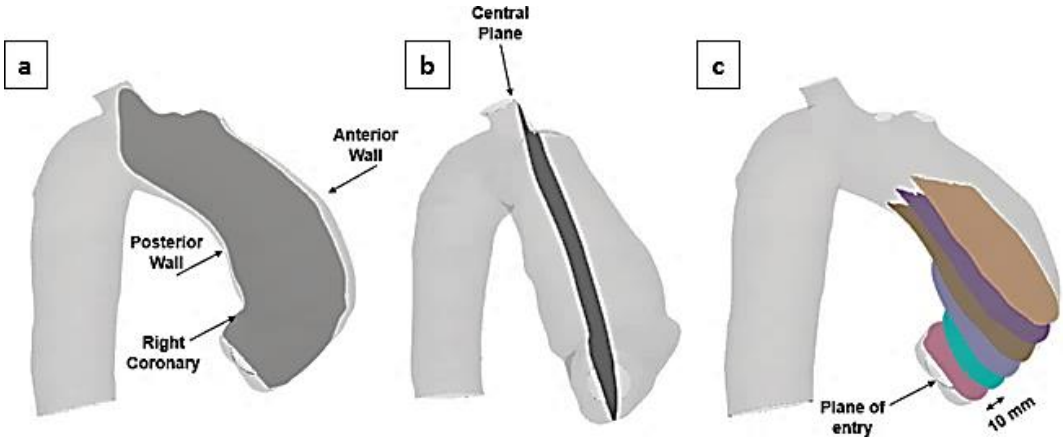

Figure 4.2 – Planes used to evaluate numerical results. (a) Central Plane. (b) Central plane. (c) Parallel planes of entry

Before analyzing the flow field in the interior of the six patients' aortas, the distribution strain rate magnitude, $\dot{\gamma}$, was examined to verify if the hypothesis of Newtonian fluid is adequate. The strain rate magnitude is defined as

$$\dot{\gamma} = \sqrt{\frac{1}{2}\dot{\gamma}_{ij}\,\dot{\gamma}_{ij}} \qquad ; \quad \dot{\gamma}_{ij} = 2\,S_{ij} \tag{4.2}$$

Patient 3 was selected to illustrate the results, since it has an intermediate valve diameter (intermediate Reynolds number), and the strain rate depends directly on the Reynolds number. The results obtained, with the aorta corresponding to the second exam (second year) are shown in Figure 4.3. Two plane were selected to visualize the $\dot{\gamma}$ distribution: a plane parallel to the inlet plane and the central plane illustrated in Fig. 4.2. Note, that the strain rate distribution is superior to 50 s^{-1}, indicating that for the cases of interest the hypothesis of Newtonian fluid is satisfactory.

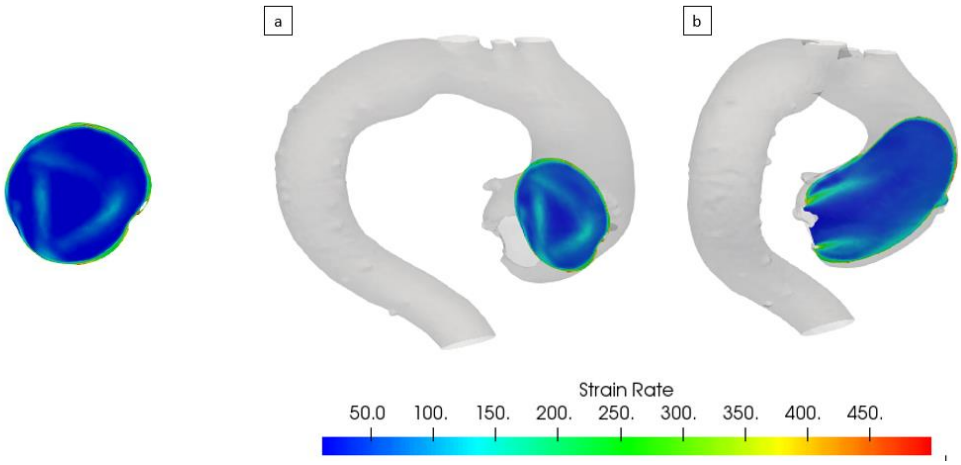

Figure 4.3 – Strain Rate distribution of Patient 3, year 2.

4.1. Patients Classification

The images, obtained with the angiotomography scan, of the six patients selected to be examined, indicated the presence of aneurysms. Since the main purpose of the present study is to identify differences in flow characteristics of patients that presented aneurysm with and without growth, it was necessary to classify the patients in these two categories. To this end, a procedure was developed to classified the patients, by comparing the aorta's geometry of the two different years. The parameter selected to aid this classification was the volume. According to Raghavan et al. (2000), the volume is a better measurement parameter than the measurement of the aneurysm diameter. This last measurement may contain errors since it is not possible to select exactly same plane to measure the diameter, in two different models.

To evaluate the volume, first the region of interest of each patient was selected, as indicated in Figure 4.4. This region was defined as the region of the ascending aorta up to the root of the brachiocephalic artery, which was already selected as a reference to create the computational domain of the aorta of two different years (Fig. 3.6). Figure 4.5 shows the area of interest selected for the same patient. Figure 4.5 (a) illustrates the 3D aorta obtained in first year, while Fig. 4.5 (b) shows the 3D aorta corresponding to the second year. This procedure was repeated for all six patients and the selected region volume was determined. Table 4.2 presents the percentage of the difference of the volume and the time interval between the angiotomography scans of each patient.

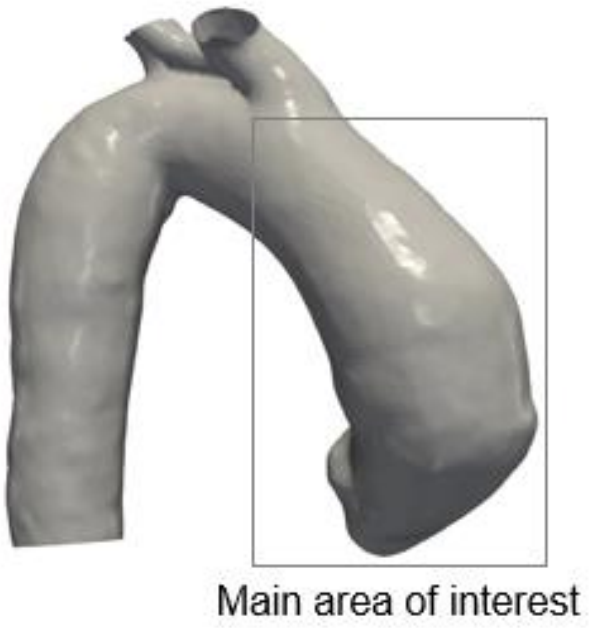

Figure 4.4 – Main area of interest to evaluate volume

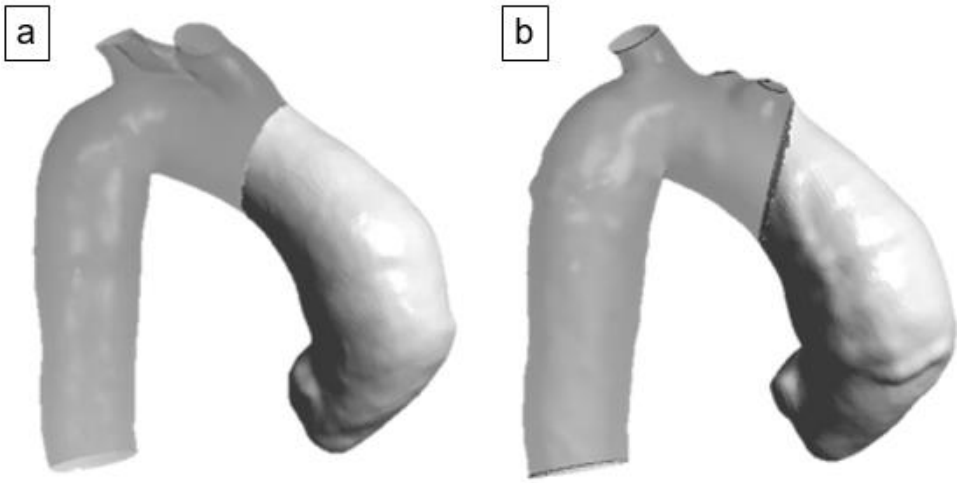

Figure 4.5 – Volume measured. (a) First Year. (b) Second Year.

Table 4.2 – Percentage of the volume difference between the two angiotomography scans and the time interval in years between scans, sex and age of patients

Patient	**1**	**2**	**3**	**4**	**5**	**6**
Volume variation (%)	18.0	10.0	15.6	10.5	0.5	-4.5
Time interval between scans (years)	2	1	2	3	1	2
Sex	M	F	M	M	F	F
Age (years)	77	60	70	63	63	52

Table 4.2. indicates that patients 1,2,3 and 4 have a dilation in the ascending portion of the aorta between 10% and 18%, while patient 5 had a dilation of only 0.5%. The measurement of the volume of the region of interest for patient 6 indicated a contraction of 4.5%, which can be explained due to the fact that the angiotomography scan was not trigged with the heart rate. This fact may have affected the accuracy of measurements. The exams were performed by clinical practice and not specifically by the present study. Not only the exams were performed with different equipment and physicians, but with different time intervals between the patient's exams. These facts may represent limitations of the current work. However, here, based on the variation of the aorta's volume measurement, patients with a volume variation equal or superior to 10% were considered as having an increase of the aneurysm and below this threshold value, the aneurysm was considered as not having presented a growth. In this way, patients 1, 2, 3 and 4 were classified as having presented a growth of the aneurysms, while it was considered that for patients 5 and 6, the aneurysms did not grow.

Table 4.3 – Patients classified

Patients	***Aneurysm grew***	***Aneurysm did not grow***
	1, 2 3, 4	5, 6

During the segmentation of the aortas, the great variety in the anatomical formats was perceived. It was noted that patients who presented aneurysmal growth in the ascending part of the aorta, had a greater angulation between the plane of entry with the beginning of the brachiocephalic trunk. Thus, the angle of entry with the beginning of the brachiocephalic trunk of all the aortic geometries in lateral view was evaluated, being denominated Angle I. When placing the anterior wall of the aorta in front view, a second angle, being called Angle II, was also defined. This angle measures the angle between the plane of entry with the central part of the brachiocephalic trunk, and are shown in Fig.4.6-4.11.

Measurements from the images of Angle I and Angle II corresponding to the first and second year are listed in Table 4.4, while Table 4.5 shows the average angle between the two years. Also, Figs. 4.6 through 4.11 show these angles of each patient, where (a) e (b) corresponds to the first year measurement and (c) and (d) refers to the second year. Further (a) and (c) present the measurement of Angle I, while Angle II is shown in (b) and (d).

Analyzing Figs 4.6-4.11 and Table 4.4, one can observe that there is no pattern in relation to the increase or reduction of both angles of the patients of the two group. However, examining Table 4.5, it can be seen that the four patients identified with a growth of the aneurysm, presented large mean Angle I (greater than 100º), and smaller mean Angle II in relation to the patients classified with a stable aneurysm (without growth, mean Angle II smaller than 60º). This result is interesting since it can be one factor easy to verify, to indicate the possibility of an aneurysm growth.

Table 4.4 – Aorta´s Angle I and Angle II of two measurements

Patient	Year	1	2	3	4	5	6
Angle I	**1**	128.52º	114.74º	143.34º	126.68º	77.24º	81.37º
	2	140.56º	104.37º	141.26º	124.33º	80.32º	92.31º
Angle II	**1**	53.25º	58.65º	45.12º	55.37º	88.22º	65.45º
	2	58.65º	53.28º	51.25º	57.94º	90.55º	69.34º

Table 4.5 – Average aorta´s Angle I and II of two measurements

Patient	1	2	3	4	5	6
Angle I	134.5º	109.6º	142.7º	125.5º	78.8º	86.8º
Angle II	56.0º	56.1º	48.2º	56.7º	89.34	67.4º

In the next sections, the flow field (velocity, shear stress and pressure) as well as turbulent quantities are examined, aiming to identify a particular flow behavior related with the two different groups.

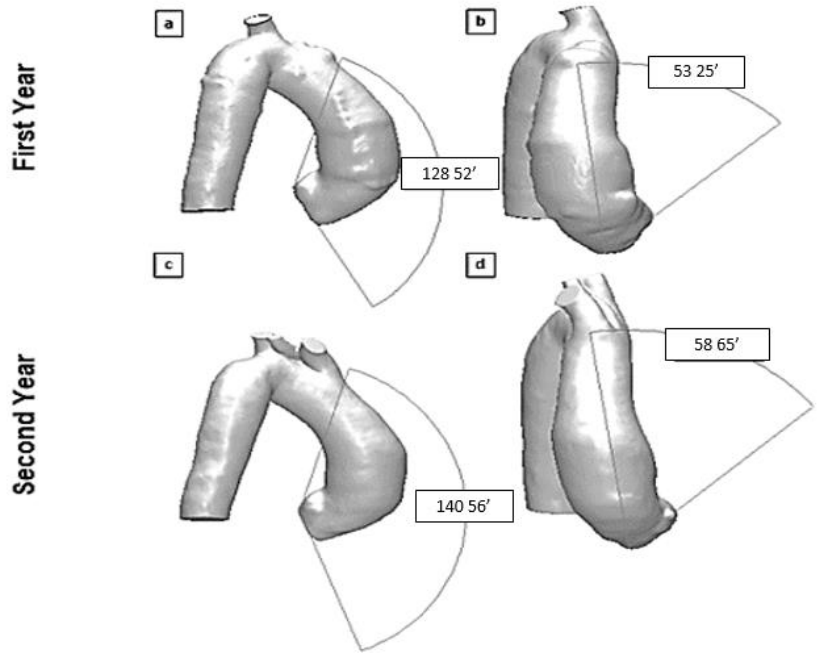

Figure 4.6 – Angles measurements of Patient 1. (a) Angle I (first year). (b) Angle II (first year). (c) Angle I (second year). (d) Angle II (second year).

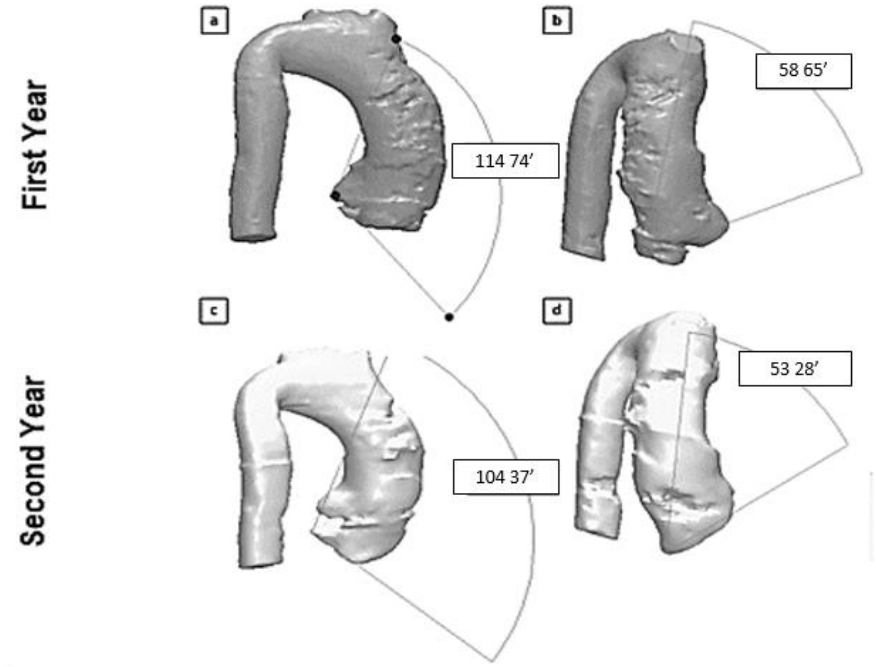

Figure 4.7 – Angles measurements of Patient 2. (a) Angle I (first year). (b) Angle II (first year). (c) Angle I (second year). (d) Angle II (second year).

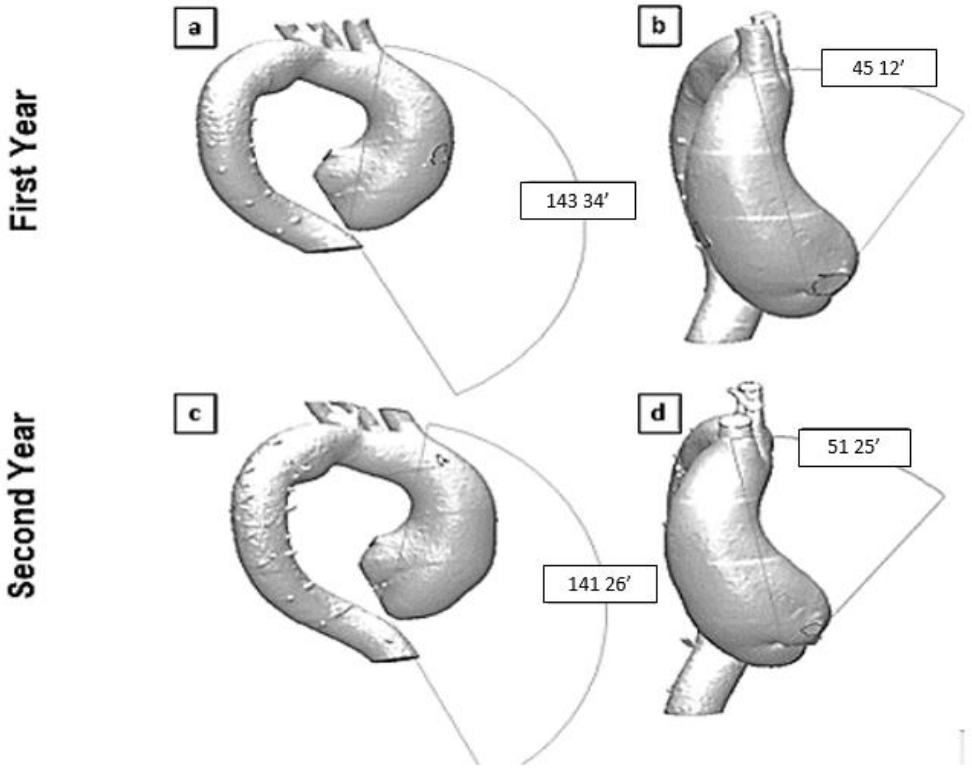

Figure 4.8 – Angles measurements of Patient 3. (a) Angle I (first year). (b) Angle II (first year). (c) Angle I (second year). (d) Angle II (second year).

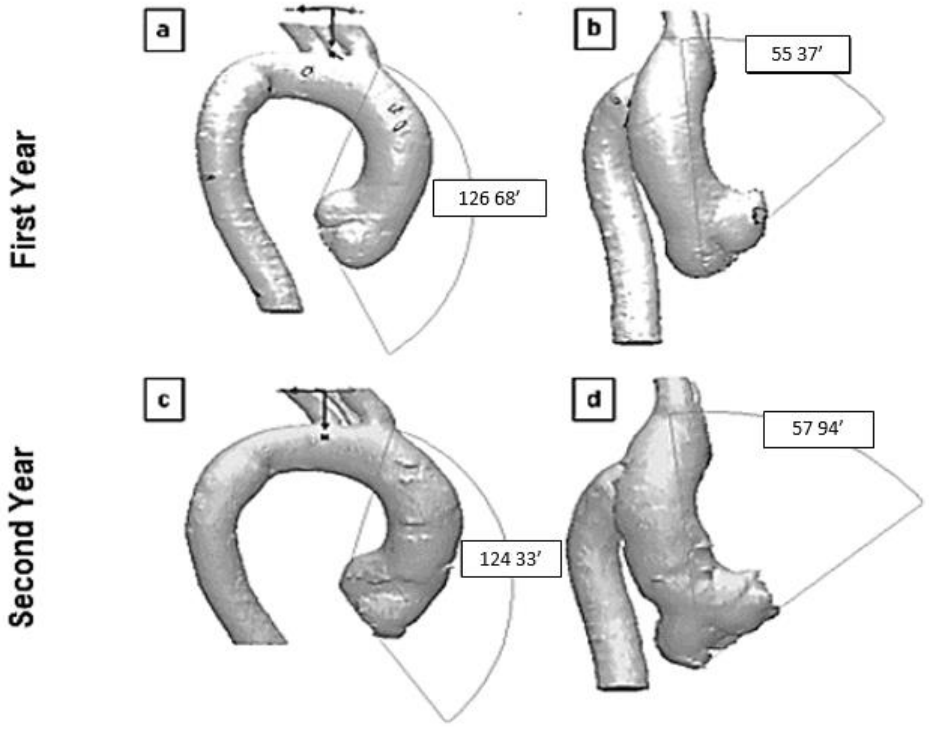

Figure 4.9 – Angles measurements of Patient 4. (a) Angle I (first year). (b) Angle II (first year). (c) Angle I (second year). (d) Angle II (second year).

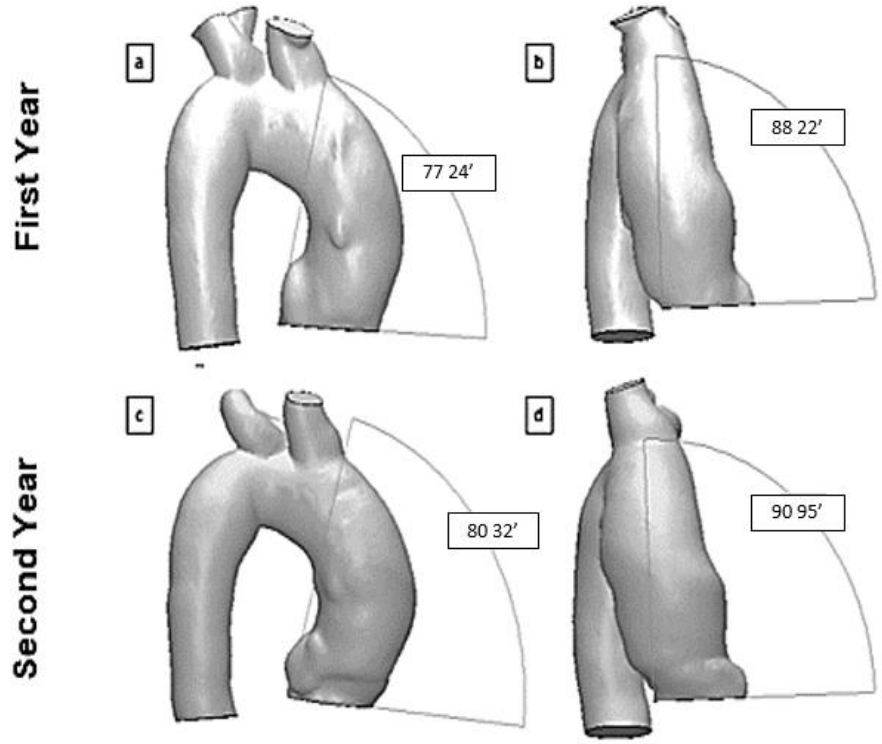

Figure 4.10 – Angles measurements of Patient 5. (a) Angle I (first year). (b) Angle II (first year). (c) Angle I (second year). (d) Angle II (second year).

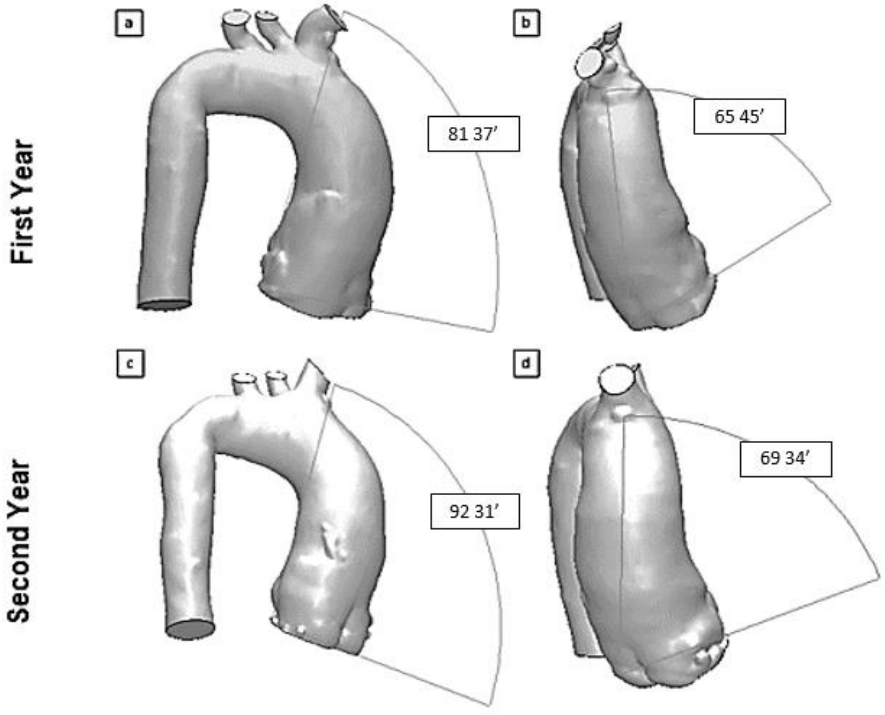

Figure 4.11 – Angles measurements of Patient 6. (a) Angle I (first year). (b) Angle II (first year). (c) Angle I (second year). (d) Angle II (second year).

4.2. Velocity Field

As mentioned, the present analysis was realized assuming steady state flow and the mass flow rate corresponding to the systolic peak was imposed. Since each patient has a different effective aortic valve diameter, the inlet axial velocity was different for each patient. Table 4.6 presents the inlet axial velocity w_{in} values of each patient.

Table 4.6 – Inlet axial velocity of each patient

Patient	**1**	**2**	**3**	**4**	**5**	**6**
Inlet velocity (m/s)	1.03	0.62	0.69	0.73	0.67	0.46

As discussed in Chapter 2, two types of hemodynamic phenomenas have been identified in patients: the eccentricity of blood flow, when the jet hits the aorta wall and the helical systolic flow, when the ejected flow form spirals. The visualization of the velocity might help identify these types of flow.

In this section, the data obtained with the simulations performed is presented. Results as iso-surface of axial velocity component (normal to the inlet plane), and streamlines are presented, as well as contours of the velocity components in the X, Y and Z (axial) directions. The coordinate system position in the aorta is shown in Fig. 3.10, where the z-axis is normal to the inlet plane, which corresponds to a x-y plane.

For all patients, the results are presented in a similar format. In the top part of the figures, the visualization of the results corresponding to the aorta´s images of first year exam are shown and in bottom, the results obtained with the aorta´s images of the second exam, realized in a later year. More than one angle of visualization is employed to help the analysis of the data.

4.2.1. Iso-Surface of Axial Velocity

A good way to visualized the main flow behavior resulting of the inlet jet is to exam an axial velocity iso-surface. To this end, the iso-surface corresponding to 50% of inlet axial velocity was selected. Figures 4.12, 4.13, 4.14 and 4.15, show an axial velocity iso-surface for the patients classified with aneurysm growth, while the results for the patients that the aneurysm did not grow are shown in Figs. 4.16 and 4.17. For this variable, three angles of visualization of the flow were defined. On the left side a front view of the aorta is shown, a lateral view can be seen in the middle, and on the right, a posterior aorta´s view.

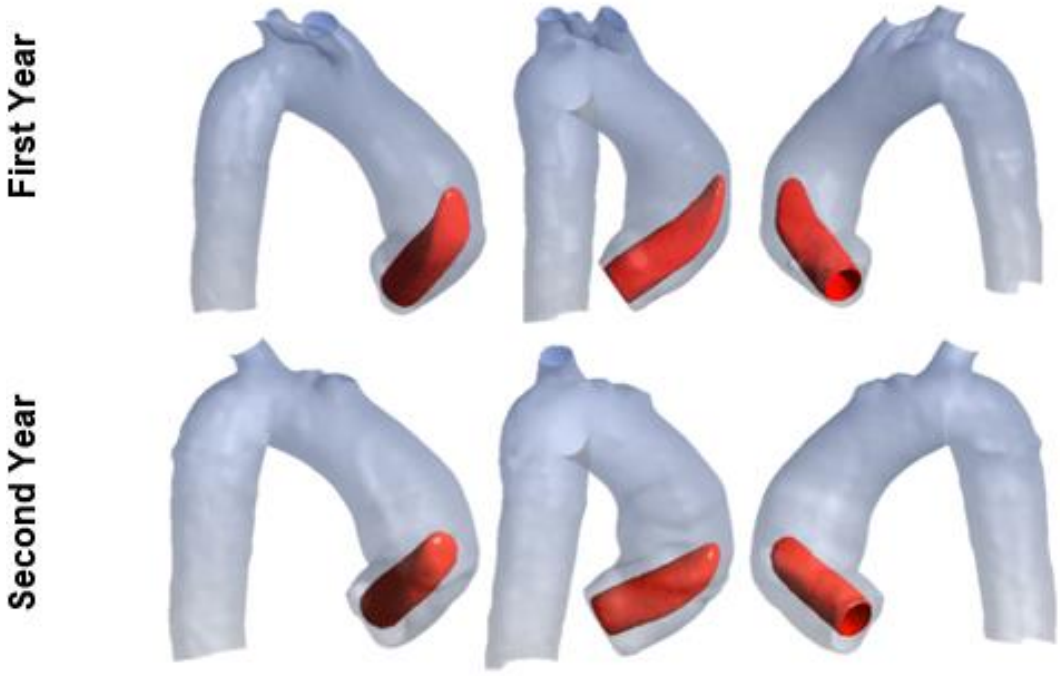

Figure 4.12 – Axial-velocity Iso-surface (w/w_{in}=0.5) of Patient 1

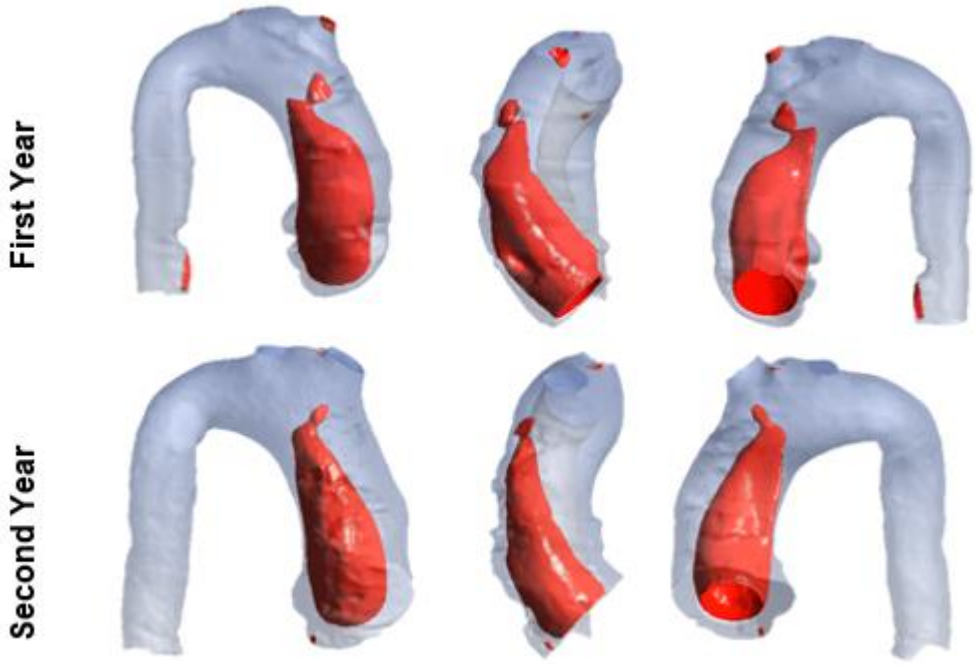

Figure 4.13 – Axial-velocity Iso-surface (w/w_{in}=0.5) of Patient 2

Analyzing the figures, it can be clearly seen that for all four patients with aneurysm growth, the inlet jet is directed towards the anterior aortic wall. For the patients whose aneurysm did not grow (Figs. 4.16 and 4.17), since Angle II (Table 4.5) is larger, the resulting flow field is more centered in the aorta's interior.

Therefore, the jet does not behave in the same way, since it does not imping at the lateral aorta´s surface, and it extends along it.

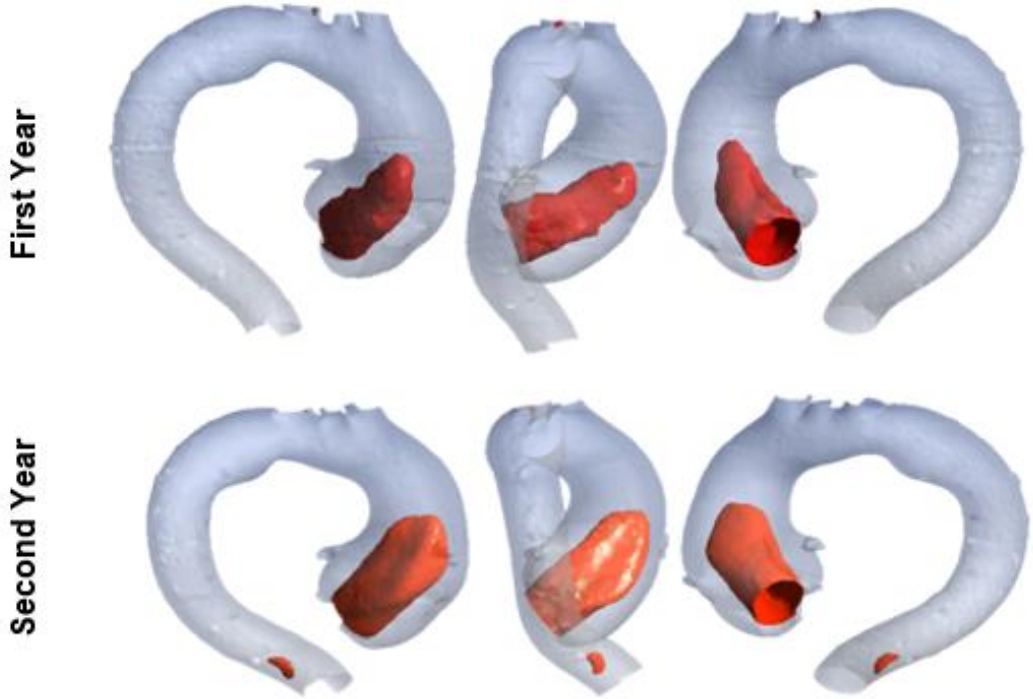

Figure 4.14 – Axial-velocity Iso-surface (w/w_{in}=0.5) of Patient 3

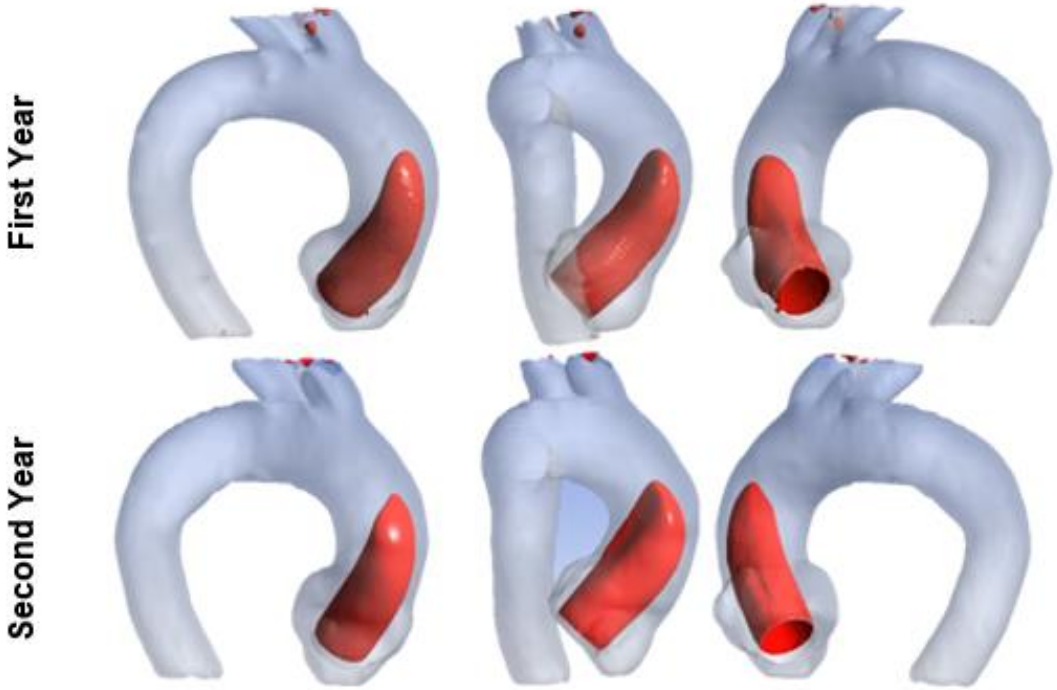

Figure 4.15 – Axial-velocity Iso-surface (w/w_{in}=0.5) of Patient 4

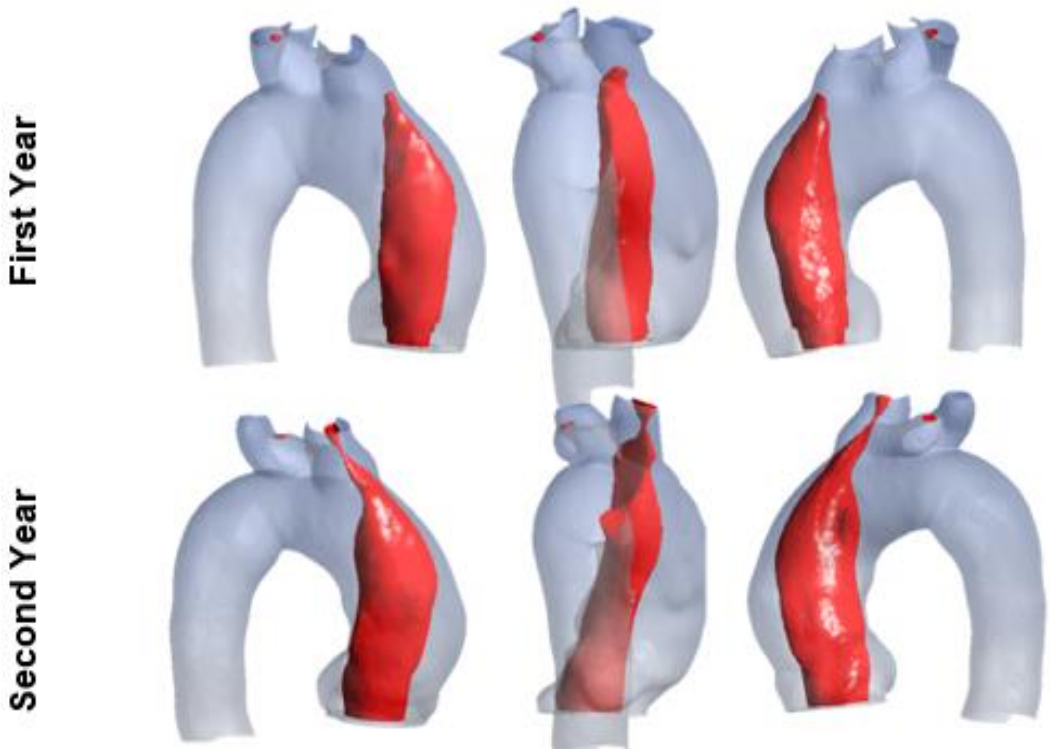

Figure 4.16 – Axial-velocity Iso-surface (w/w_{in}=0.5) of Patient 5

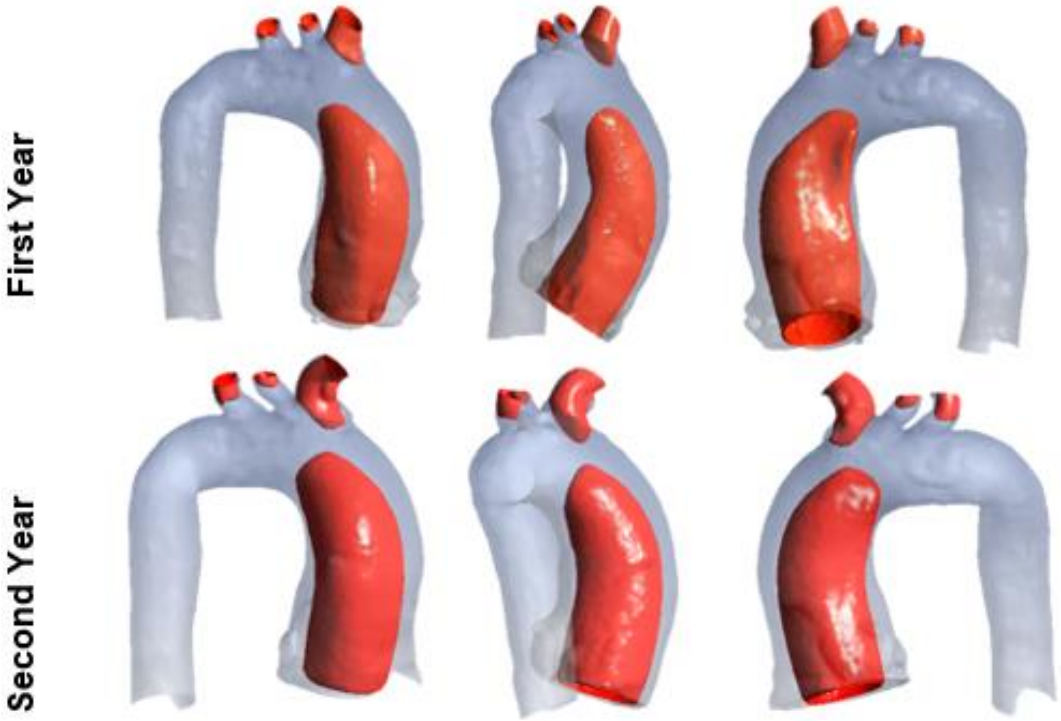

Figure 4.17 – Axial-velocity Iso-surface (w/w_{in}=0.5) of Patient 6

4.2.2. Streamlines

Another variable that can help visualized the flow behavior is the streamline, i.e., a line tangent to the velocity vector. For all patients and for the aortas corresponding to the two exams in different years, the streamlines are shown in Figs. 4.18-21 (patients with aneurysm growth) and 4.22-23 (patient without aneurysm growth). The streamlines were colored with the dimensionless modulus of the velocity vector, and the scale is represented in the lower part of the figures.

It can be seen, analyzing the streamlines in Fig. 4.18-21 for the four patients with aneurysm growth, as already observed with the iso-surface of axial velocity, that the inlet jet impinges the anterior aorta wall. Here, it is possible to visualize flow recirculation regions near the posterior part of the jet. Patient 1, Fig. 4.18, shows higher velocities near the inlet, as a consequence of the smaller valve aortic effective diameter and corresponding larger inlet velocity (Table 4.6). Patient 2, Fig. 4.19, presents a less steep curvature of the streamlines at the ascending aorta, but it is possible to visualize the jet being directed towards the anterior wall. For this patient, an increase in the flow velocity can be observed at the descending part of the aorta (not focus of the present work), due to the smaller diameter. The curvature of the aorta´s arch is much more stronger for Patient 3, Fig. 4.20, but a similar streamline distribution can be seen, as the others patients with aneurysm growth. Although Patient 4, Fig. 4.21, presents the inlet jet being directed to the wall, this patient does not present as many recirculation on the back of the jet as the others patients. In the first year, a recirculation in the frontal part of the aorta, near the region where the aneurysm is formed can be seen. However, this strong recirculation disappears in the second year. This can be explained by the increase in diameter, as a consequence of the aneurysm growth in this region, reducing the flow velocity, and may have caused this recirculation to disintegrate and disappear in the second year of the examination.

The streamlines of the patients without aneurysm growth are shown in Fig. 4.22-23. For Patient 5, Fig. 4.22, although the jet is directed to the posterior part of the aorta and strikes the wall, the impinging point is far from the inlet, where the speed of the jet has already diminished considerably, and the recirculation's on the front of the jet has low velocities. The streamlines of Patient 6, Fig. 4.23, are centered in the ascending part of the aorta, without being directed to the wall, and small recirculation with low velocities can also be seen.

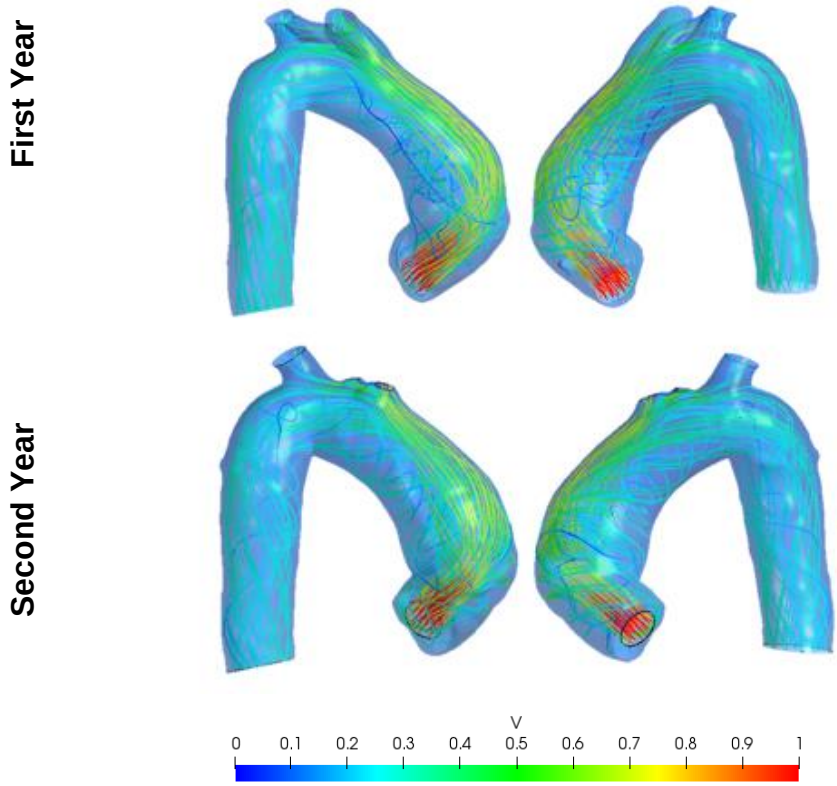

Figure 4.18 – Streamlines of Patient 1

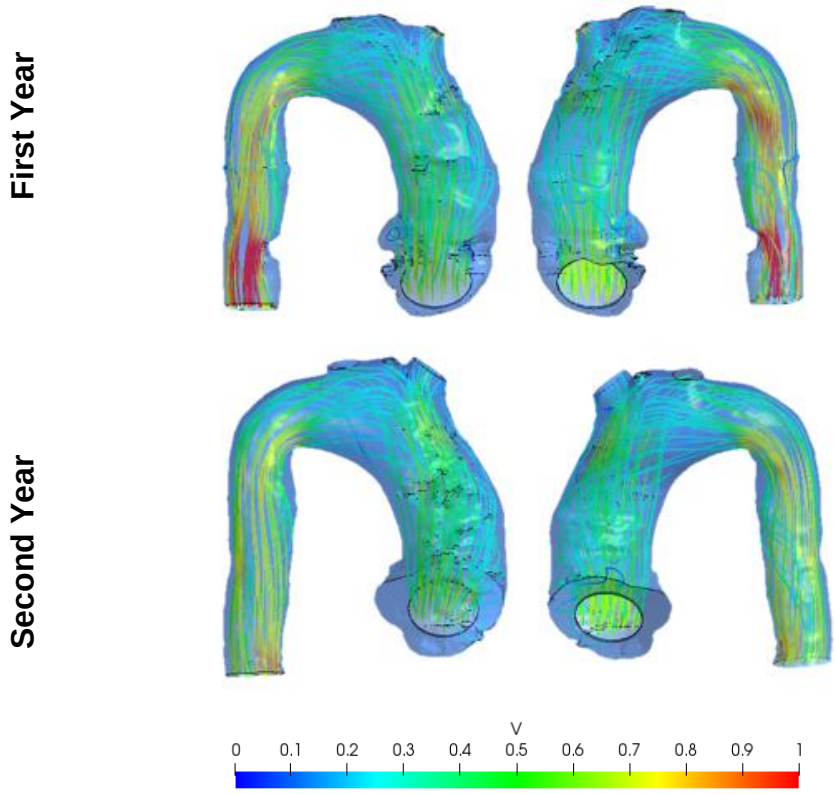

Figure 4.19 – Streamlines of Patient 2

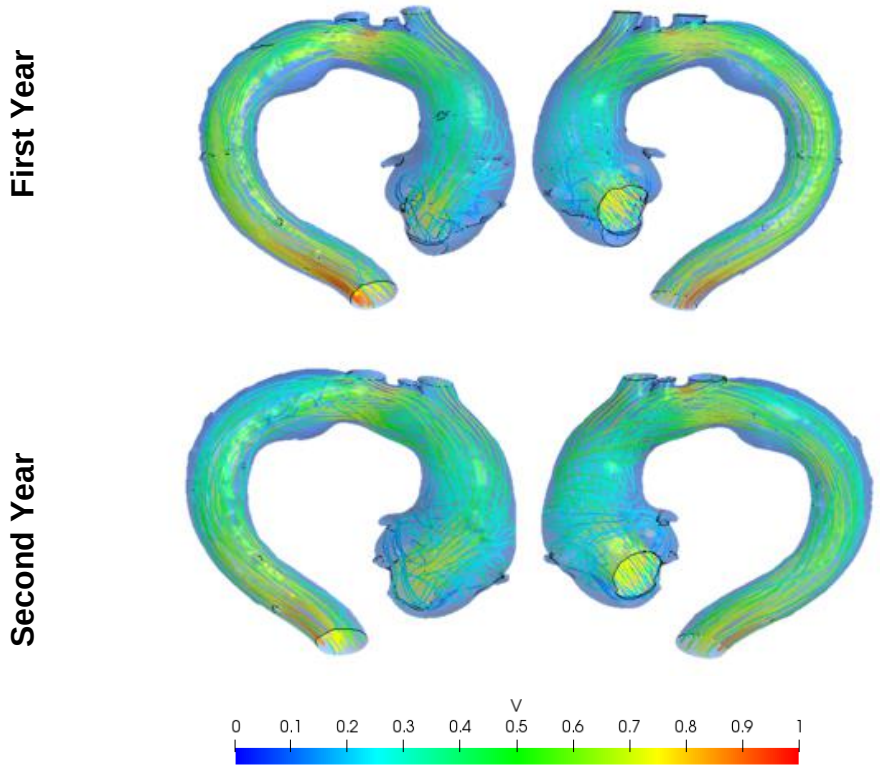

Figure 4.20 – Streamlines of Patient 3

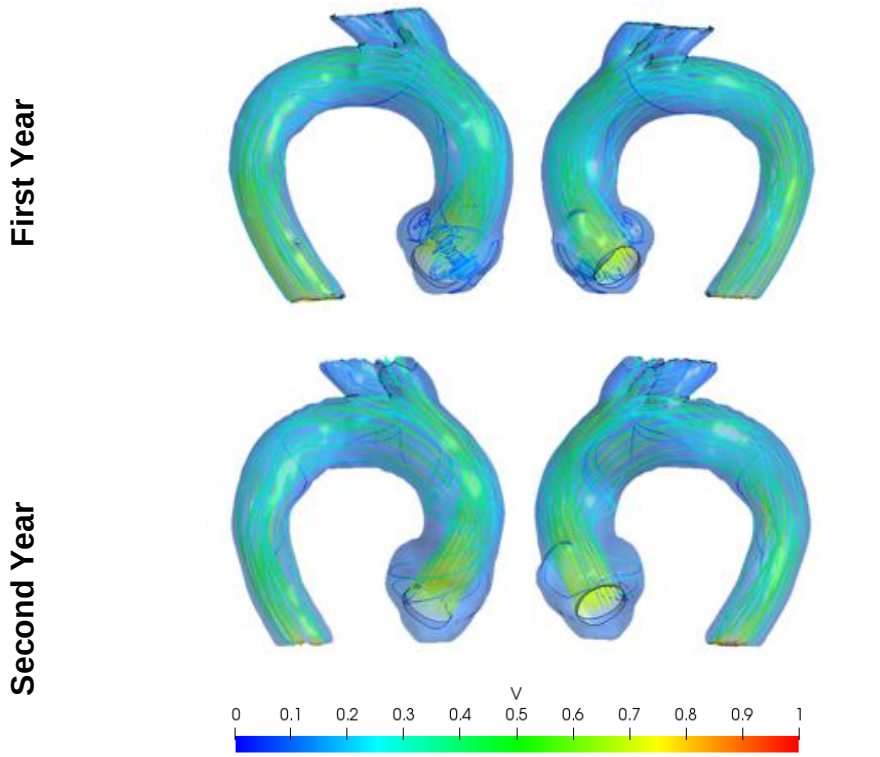

Figure 4.21 – Streamlines of Patient 4

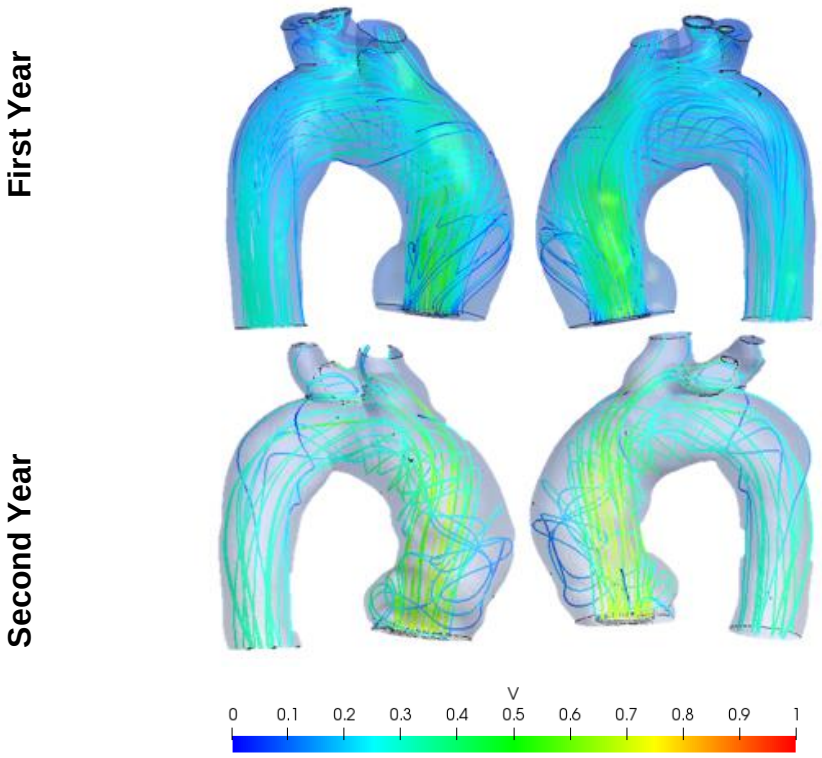

Figure 4.22 – Streamlines of Patient 5

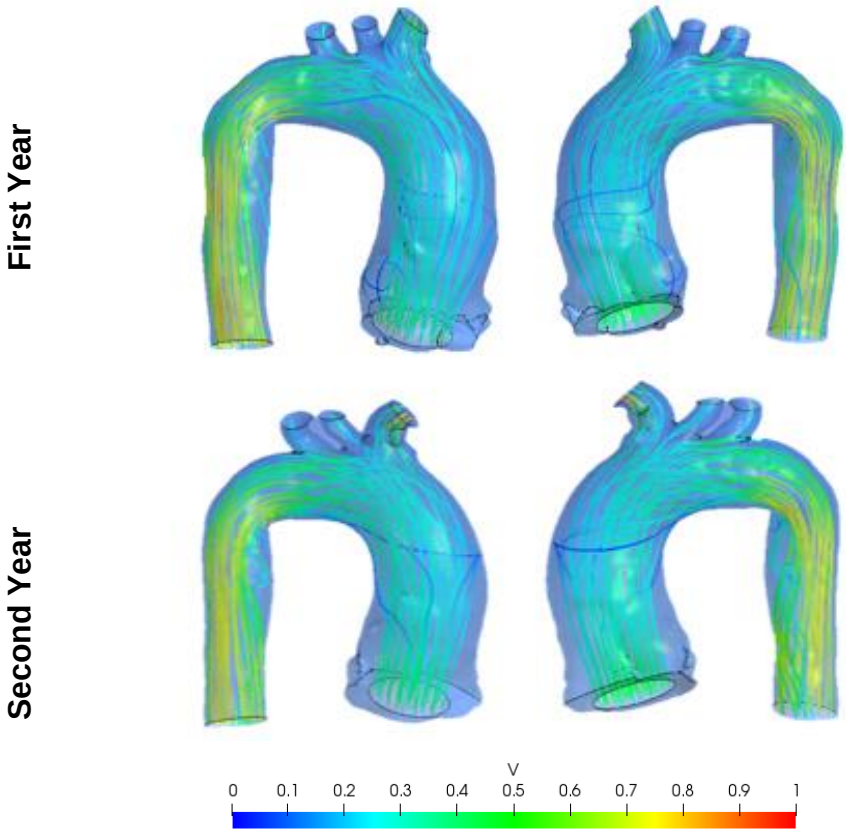

Figure 4.23 – Streamlines of Patient 6

4.2.3. Velocity Components

All three dimensionless velocity components are examined here. Initially velocity contours at the planes indicated in Fig. 4.2 are examined. Then, to allow to perform a quantitative analyze, the velocity components profiles were plotted along the central z-axis for each aorta, from the origin until it reaches the aortic wall. Figure 4.24 illustrates the line in which these profiles were drawn.

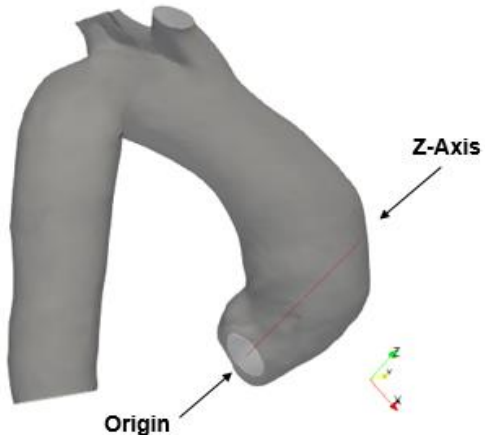

Figure 4.24 – Example of z-axis where profiles were drawn

4.2.3.1. Z Velocity

Initially Patients 1 and 6 were selected to be examined. These two patients were chosen because they represent, respectively, an example of a patient who the aneurysm grew and did not grow, respectively. The dimensionless axial velocity contour of Patient 1 is presented in Fig. 4.25, and Patient 6 in Fig. 4.26. In these figures, the sub-figure (a) shows the velocity distribution in perspective in x-y planes, (b) corresponds to the central plane and (c) shows the x-y planes without perspective, with the plane on the left closest to the entrance and the plane on the right, the farthest.

Examining Fig. 4.25 for Patient 1, with aneurysm growth, the displacement of the main jet to the anterior aorta's wall, can be visualized in Figs (c). Further, as a consequence of the aneurysm increase (larger diameter), a longer jet was obtained in the second year. For Patient 6, Fig. 4.26, the flow distributions of both years are similar, with a centered jet. This was already expected, since the size of the aorta was maintained approximately constant. The reduction of the axial velocity as one moves away from the inlet can be clearly seen in all figures of the transverse planes, for both years and both patients.

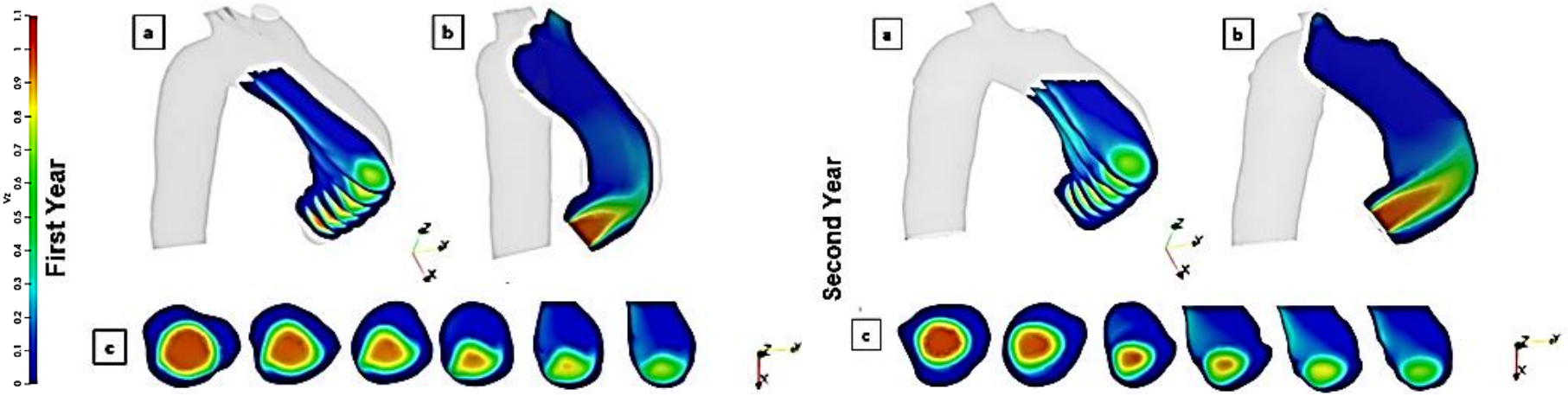

Figure 4.25 – Contours of Axial Velocity of Patient 1. (a) Transverse planes. (b) Central plane. (c) Cross-sectional individual plans

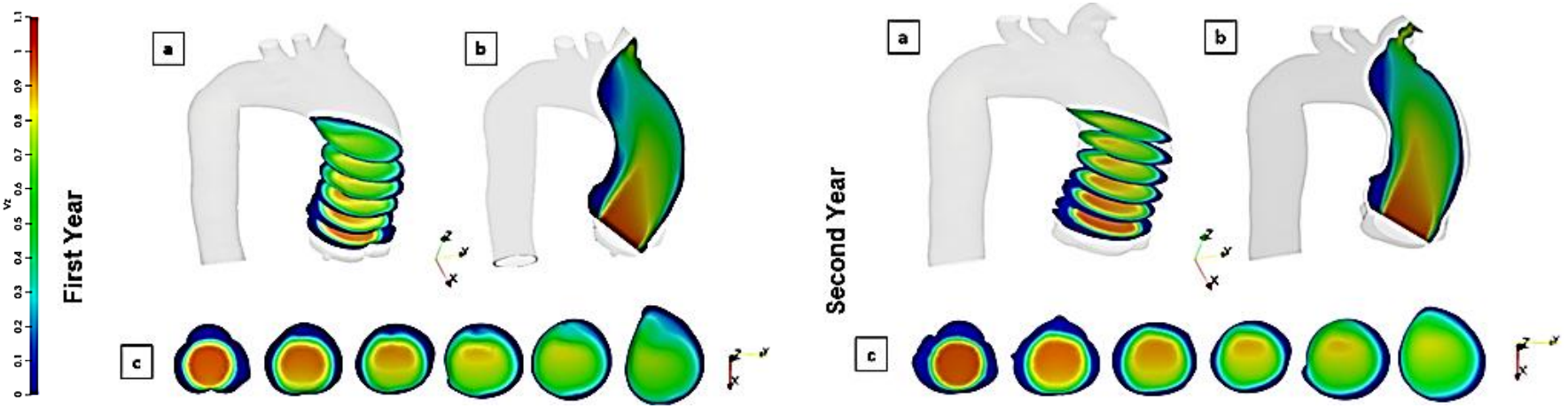

Figure 4.26 – Contours of Axial Velocity of Patient 6. (a) Transverse planes. (b) Central plane. (c) Cross-sectional individual plans

To corroborate the flow similarities among the patients of the two groups, Figs. 4.27 and 4.28 present the axial velocity contours for Patients 2, 3, 4 and 5. A combined analysis of all planes allows to say that for the patients, which the aneurysm grew, Patient 2 and 3 (Fig. 4.27) and Patient 4 (Fig. 4.28), the axial velocity distribution is similar to the one shown for Patient 1, i.e., inlet jet is directed to the anterior aorta's wall. Further, for Patient 5 (Fig. 4.28), who the aneurysm did not grow, although the jet is more central, it impinges the posterior wall.

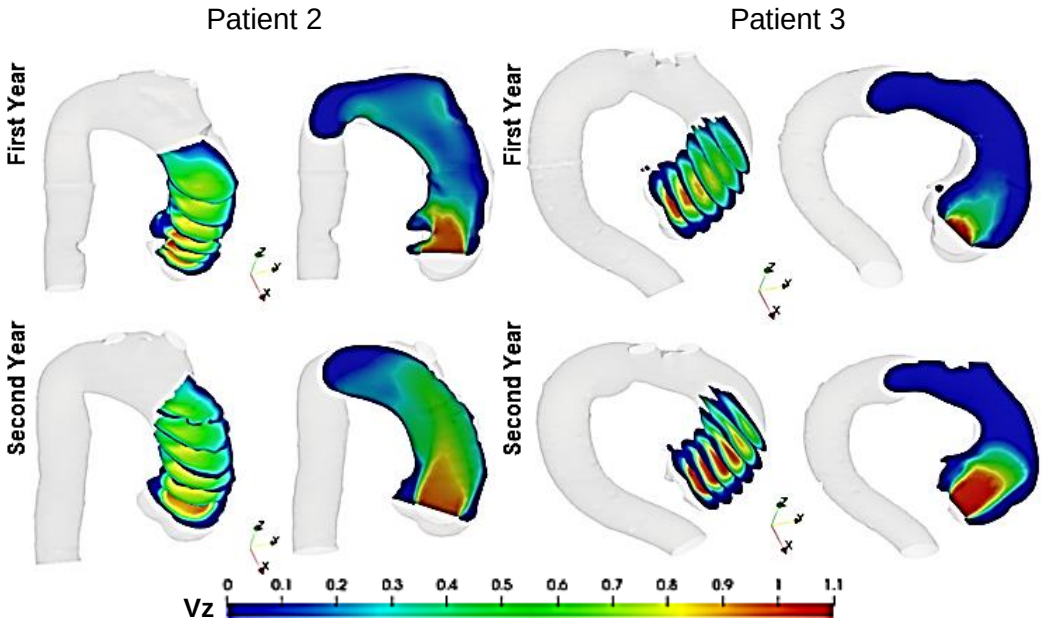

Figure 4.27 – Contours of Axial Velocity of Patient 2 and 3 (aneurysm grew).

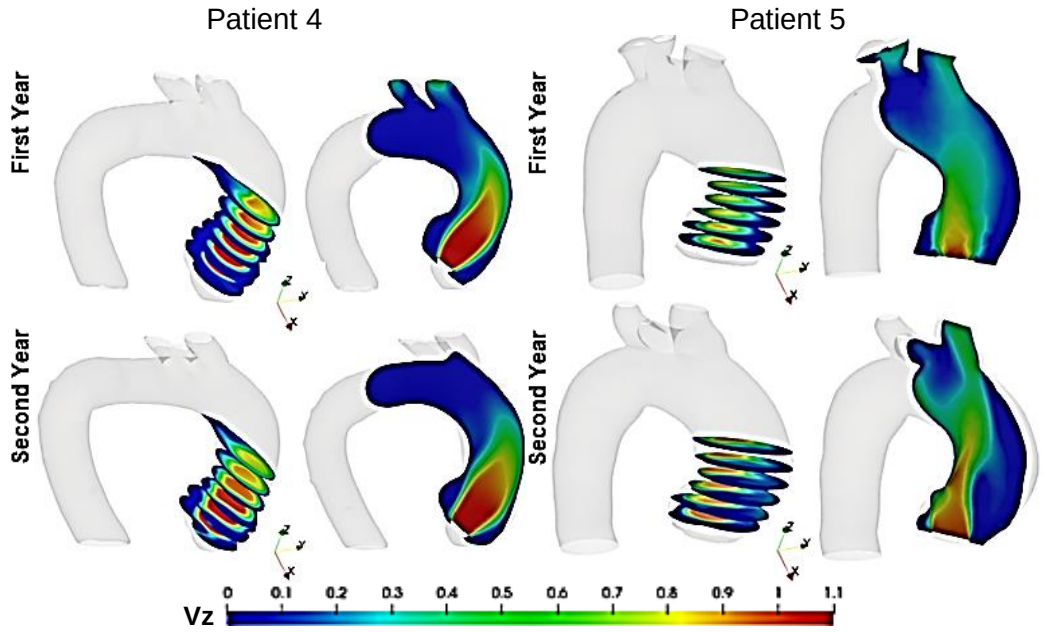

Figure 4.28 – Contours of Axial Velocity of Patient 4 (aneurysm grew) and Patient 5 (aneurysm did not grow)

The dimensionless axial velocity profile along the central z-axis is shown in Figure 4.29 and 4.30, for the two groups of patients. In these figures, the abbreviation F corresponds to the flow field obtained in the aorta generated with the images of the first year angiotomography exam, and the symbol S, corresponds to the results obtained with the images of the second year exam.

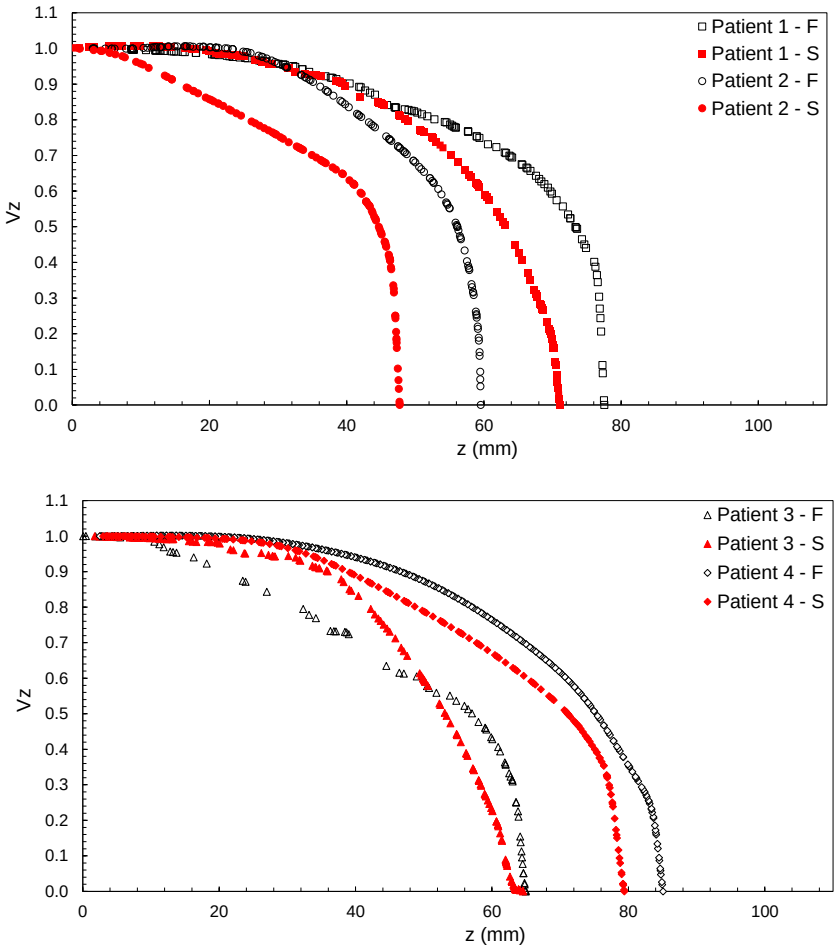

Figure 4.29 – Axial Velocity component along z-axis of patients with aneurysm growth (Patient 1, 2, 3 and Patient 4)

Analyzing Fig.4.29, which corresponds to the results of the patients for whom the aneurysm grew, it can be seen that the position where the jet impinges the aorta's wall (where the z-velocity goes to zero) occurs in a smaller z position in the second year in relation to the first year. These results indicate that the jet becomes more proximal, with higher velocities near the inlet, and consequently near the anterior wall. For patients, for whom the aneurysm did not grow (Fig. 4.30), the opposite behavior can be seen, i.e., the impinging point occurs in a larger z-position in the second year in relation to the first year, indicating that the jet becomes more distal, which hinders high jet velocities to reach the anterior wall.

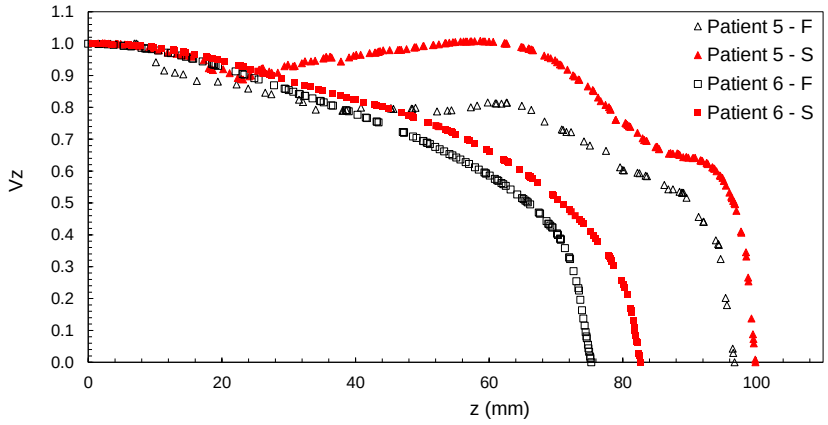

Figure 4.30 – Axial Velocity component along z-axis of patients without aneurysm growth (Patient 5 and 6)

Note that Patient 1, with the smaller z-impingement position, presented the larger volume growth (Table 4.2), and also the largest Angle I (Table 4.5). On the other extreme is Patient 5, with the largest z-position of the impinging jet, who presented an approximately constant volume of the selected ascending aorta's region, with the smallest Angle I. The second largest impinging position in the first year corresponds to Patient 6, also classified as not having an increase on his aneurysm. As the impinging point is farther from the inlet, due to the reduction of the strength of the jet with the distance, it seems that the impinging jet is less likely to induce an aneurysm growth. Finally, it can be observed that as a consequence of the aneurysm growth, the jet becomes closer to the inlet, due to the aorta´s arch curvature, Angle I. This fact results in exposure of the proximal aorta segments to high mechanical stresses, which may favor the aortic remodeling process.

4.2.3.2.X- and Y- Velocity Components

The x- and y- velocity components distributions can help to visualized the flow field structure inside the aorta. The dimensionless velocity contours of the x- and y-velocity components of Patient 1, with aneurysm growth and Patient 6, without aneurysm growth were selected to illustrate the flow field, in the same planes selected to analyze the axial component. Figs. 4.31 and 4.32 correspond to x-component and y-component, respectively, of Patient 1. These fields are analyzed together to aid identify the presence of regions with recirculating flow, around the axial inlet jet. The same type of results is shown in Figs. 4.33 and 4.34, which corresponds to Patient 6. However, due to the large differences in velocity levels, different scales were employed for each patient.

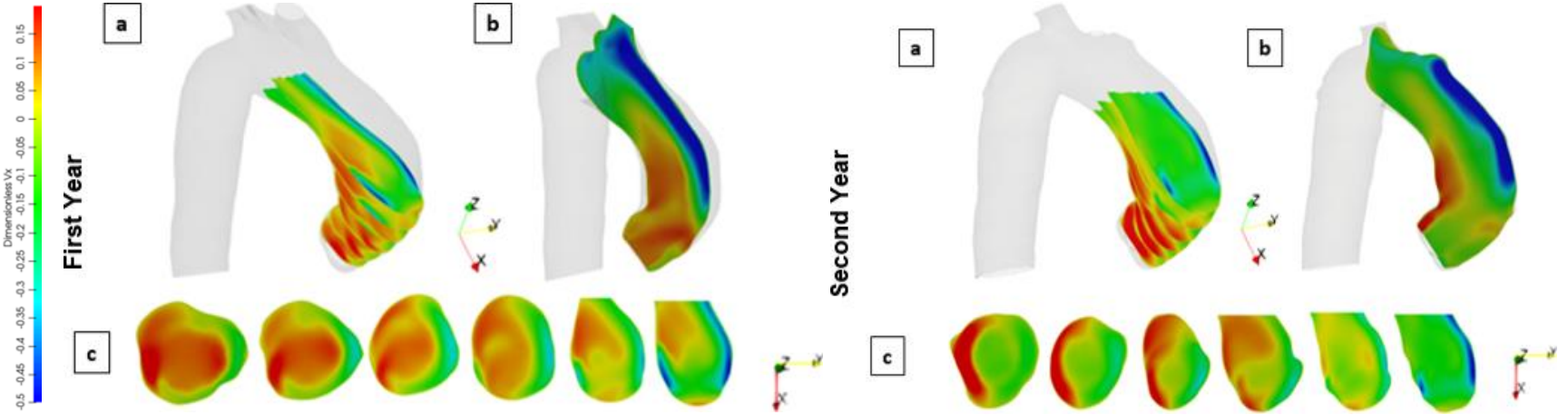

Figure 4.31 – Contours of X Velocity of Patient 1. (a) Transverse planes. (b) Central plane. (c) Cross-sectional individual planes.

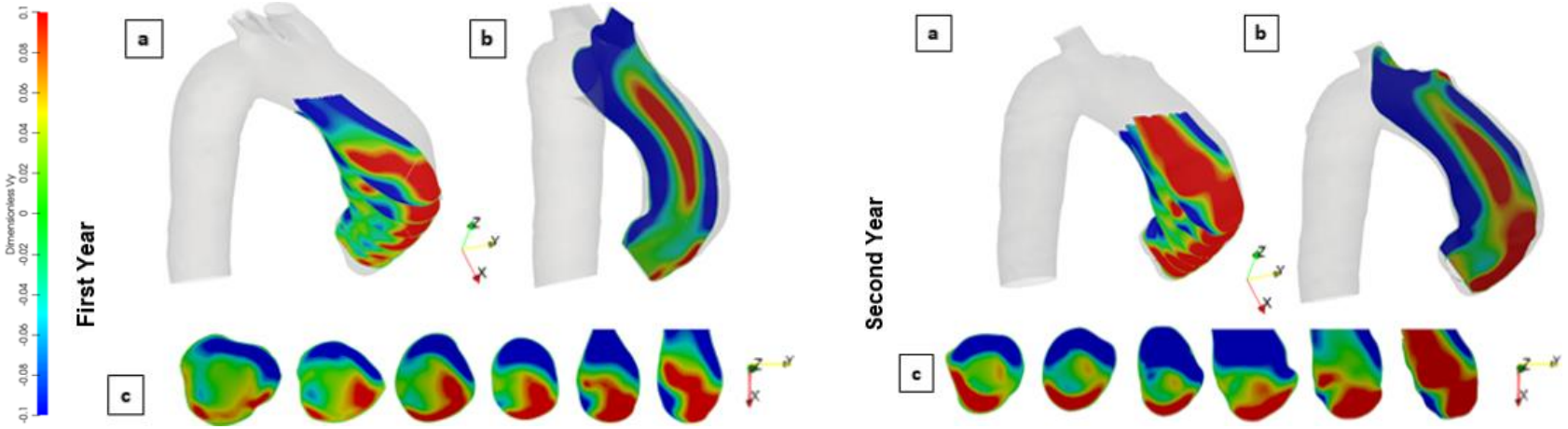

Figure 4.32 – Contours of Y Velocity of Patient 1. (a) Transverse planes. (b) Central plane. (c) Cross-sectional individual planes

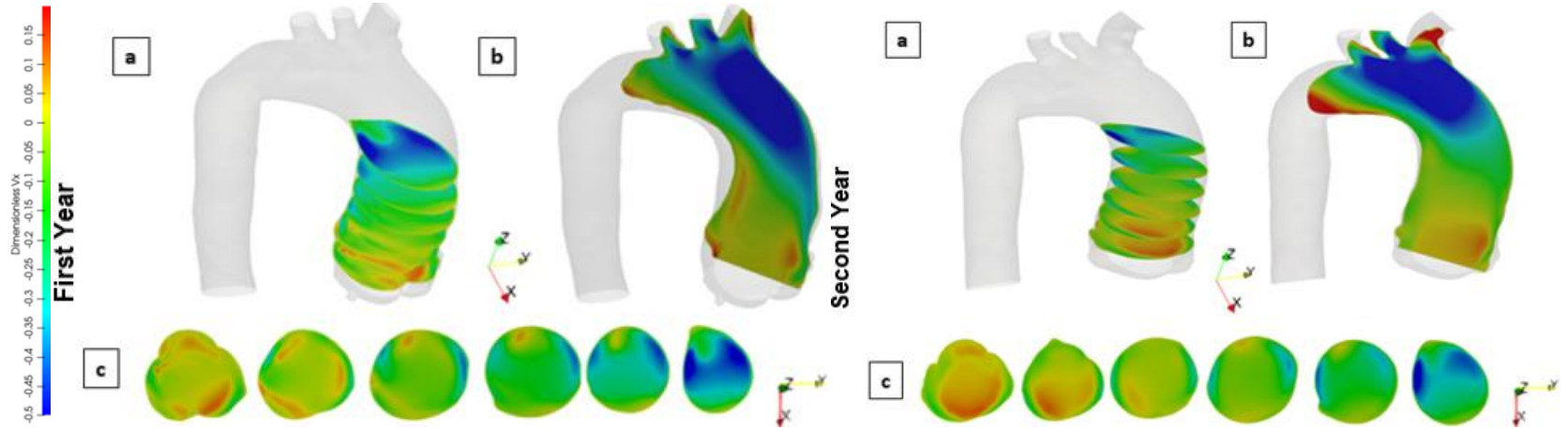

Figure 4.33 – Contours of X Velocity of Patient 6. (a) Transverse planes. (b) Central plane. (c) Cross-sectional individual planes

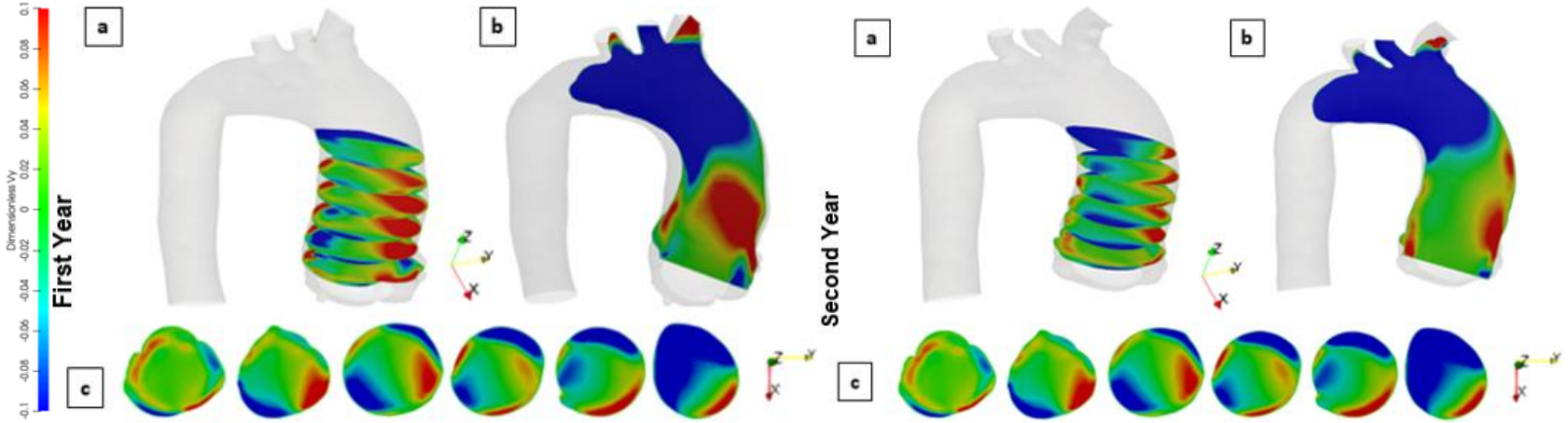

Figure 4.34 – Contours of Y Velocity of Patient 6. (a) Transverse planes. (b) Central plane. (c) Cross-sectional individual planes

The overall-behavior of the x- and y- velocity components for both patients is similar. When analyzing the x-component contour in the central plane, Figs. (b), it is possible to identify fluid flowing down (in the negative x-direction) near the right wall, and positive (going up) near the left wall. At the same time, the y-component is negative near the wall, and positive in the central region, indicating that the fluid is being directed to the center of the aorta. The velocities contour in Figs. (a) and (c) show more clearly, at the aorta´s cross section, the formation of recirculating flow round the main jet. The flow is directed to the anterior wall from the left side (x- velocity positive) e returns on the right side (y-velocity) negative. Analyzing the y-component, it can be seen that it flows from right to left at the posterior region (y-velocity negative) and return near the anterior region (y-velocity positive).

Focusing in Patient 1 (Fig. 4.31), it is perceived the strong near-wall recirculation caused by the velocity component at x in the two analyzed years. Comparing the individual transverse planes, there is a decrease in the high values presented by the velocity component x of the first year.

It is observed that the flow field of Patient 6 presents positive values of the velocity component x only in the first and second transverse planes (Fig. 4.33). In the second year, the positive values extend beyond the first two planes, indicating an increase of the recirculation caused by the x-velocity component.

It can also be mentioned that for both Patient 1 and Patient 6, the transverse planes showed regions with high values of component y-velocity close to the anterior aortic wall. In any case, Patient 1, Fig. 4.32, have a larger region of high y-velocity values (and displaced to the upper part of the aorta), when compared to Patient 6, Fig. 4.34. These results indicate the presence of stronger recirculation in case of aneurysm growth.

Proceeding in an analogous as presented for z-velocity (axial) component for different patients, the dimensionless x-velocity and y-velocity components were plotted along the central z-axis of each aorta. Figure 4.35 presents the results for patients with aneurysm growth (Patient 1, 2, 3 and 4) and Fig. 4.36 for patients with no growth of the aneurysm (Patients 5 and 6). In all cases, the flow behavior is qualitatively similar, i.e., as one moves along the z-axis, both velocity components are very small. Due to the aortic arch, as the z-axis approaches the anterior aorta wall, se x- component becomes negative, increasing its value in modulus, and then it goes to zero at the wall. An opposite behavior can be seen with regard to the y-velocity component.

As already mentioned, for the patients who presented an aneurysm growth, the inlet jet impinges the aorta in a smaller z position in the second year in relation to the first year and the opposite was observed for patients for who the aneurysm did not grow. However, analyzing both x- and y- velocity components of all patients in the two years it was not possible to identify a clear difference between the flow field of the two groups with and without aneurysm growth.

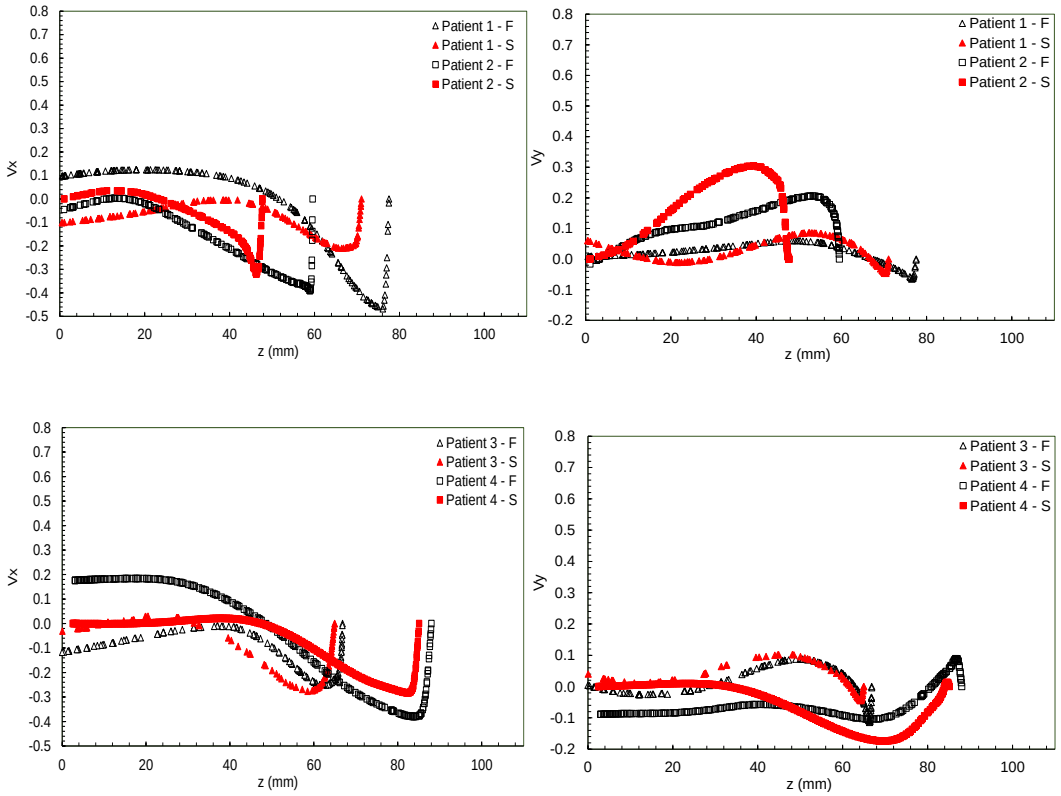

Figure 4.35 – X- and Y-Velocity components along z-axis. Patient 1, 2, 3 and 4 (with aneurysm growth)

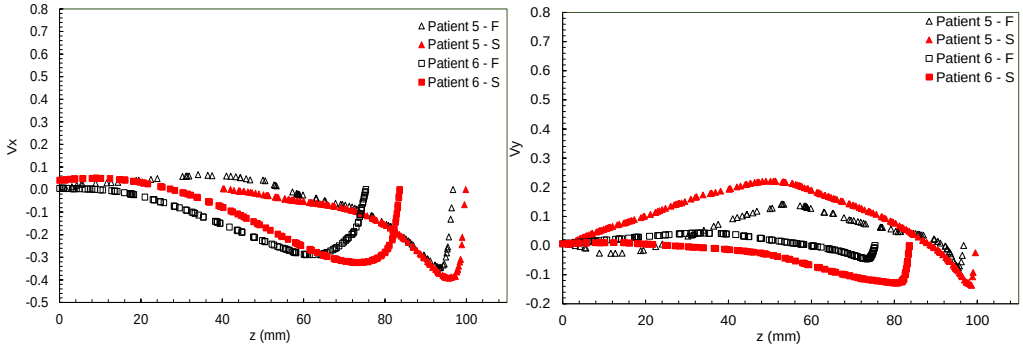

Figure 4.36 – X- and Y-Velocity components along z-axis. Patient 5 and 6 (with aneurysm growth)

4.3. Pressure

Pressure level, as well as pressure distribution is crucial for a heathy human being, and it can play an important hole inducing an aneurysm growth. From the fluid mechanical point of view, a sudden increase in diameter leads with a separation of the boundary layer and a separation bubble, generating a region with high pressure loss. Further, low pressure regions can be correlated with turbulent coherent structures. On the other hand, when the incoming jet from the aortic valve impinges at the aortic surface, it generates a high-pressure region. These phenomena may influence an aneurysm growth (Gülan et al., 2018).

Once again, Patients 1 and 6 were selected to illustrate the flow behavior for patients with growth and no growth of an aortic aneurysm. The differential pressure in relation to the valve inlet ($p - p_{in}$) corresponding to Patient 1 is shown in Fig. 4.37 and for Patient 6 in Fig 4.38. In these figures, the same layout is employed for the velocity components distributions are applied. Sub-figure (a) shows the pressure distribution in perspective in x-y plans, sub-figure (b) corresponds to the central plane and sub-figure (c) shows the x-y planes without perspective, with the plane on the left closest to the entrance and the plane on the right, the farthest.

Analyzing Fig. 4.37 of Patient 1, with aneurysmal growth, it is possible to notice that the region with high-pressure, which is close to the anterior wall, has increased from the first to the second year. Patient 6, Fig. 4.38, although also presenting this high pressure region near the wall, shows no significant difference between the first and second year. In addition, while Patient 1 has a pressure increase in relation to the inlet up to 100 Pa, for Patient 6 the pressure at the impinging region is 50 Pa larger than the inlet. Due to the jet expansion near the aortic valve, there is a region of pressure loss (blue color). Comparing the pressure distribution of both patients in Figs 4.37 and 4.38, a slightly larger region can be observed for Patient 1, who presented a growth of the aneurysm.

Dimensionless pressure P, along the z-axis was plotted for all patients. Figure 4.39 presents the results for patients with aneurysm growth (Patient 1, 2, 3 and 4) while Fig. 4.40 for patients with no aneurysm growth (Patients 5 and 6). As expected, at the impingement point at the aortic wall, a peak of pressure is obtained for all cases. It can also be observed, that a very small pressure drop was obtained near the aortic valve for all cases.

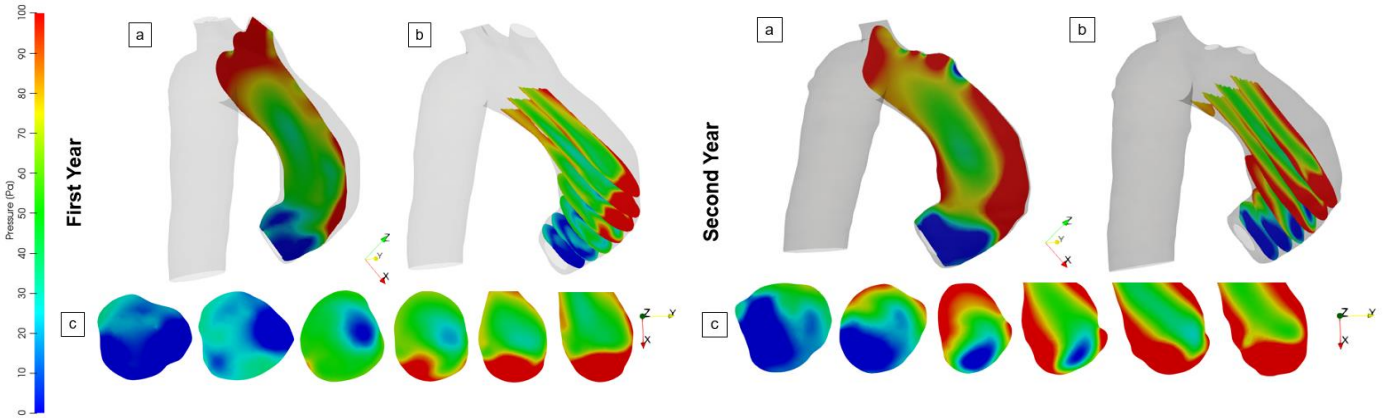

Figure 4.37 – Contours of Pressure of Patient 1. (a) Transverse planes. (b) Central plane. (c) Cross-sectional individual plans

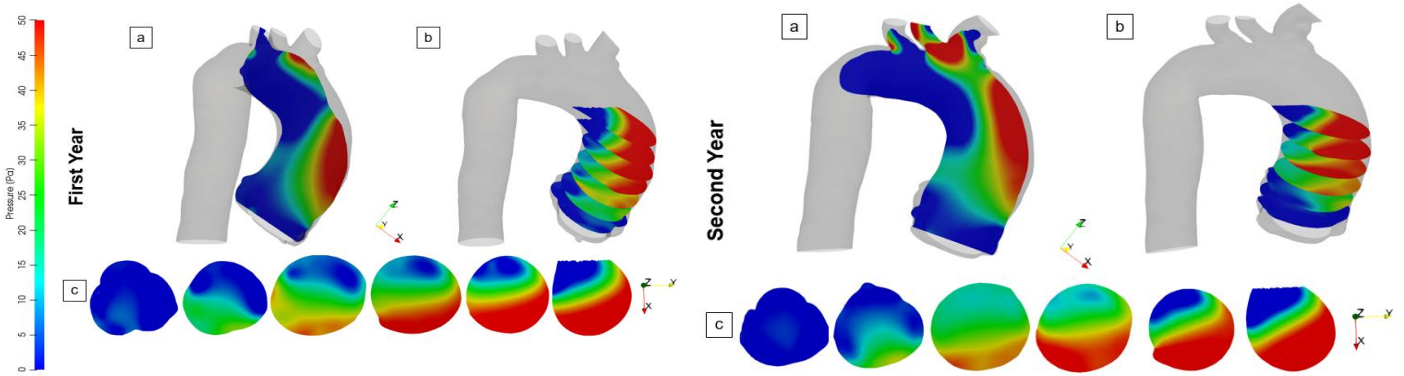

Figure 4.38 – Contours of Pressure of Patient 6. (a) Transverse planes. (b) Central plane. (c) Cross-sectional individual plans

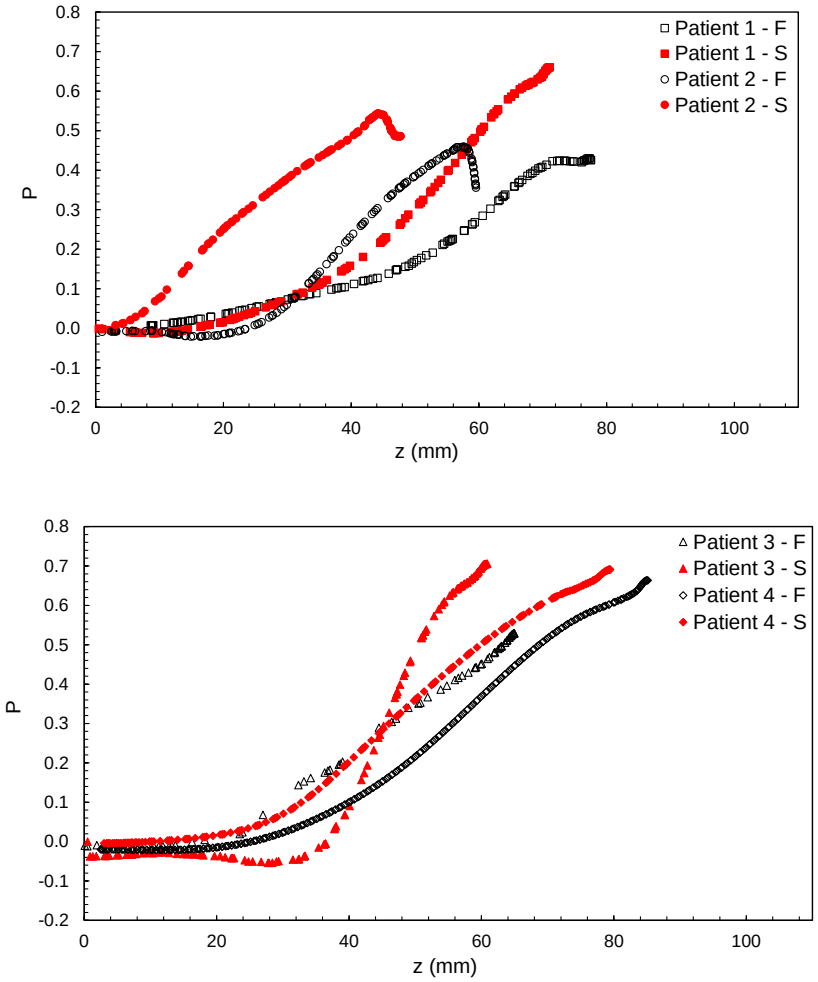

Figure 4.39 – Pressure along z-axis of patients with aneurysm growth (Patient 1, 2, 3 and Patient 4)

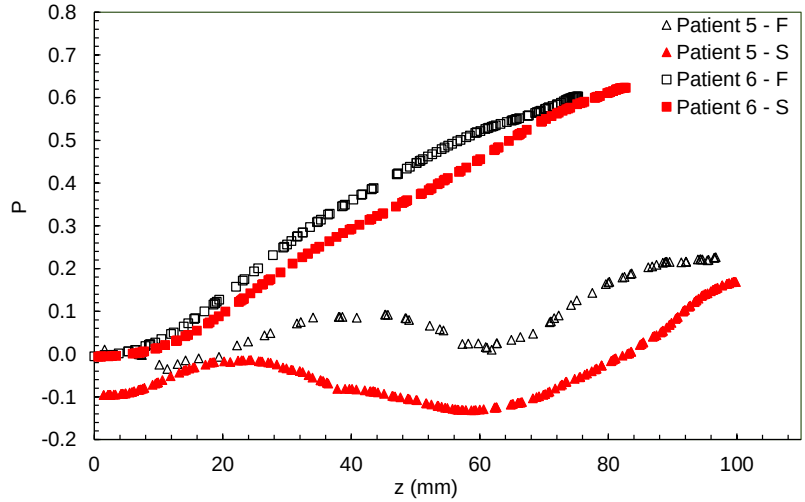

Figure 4.40 – Pressure along z-axis of patients without aneurysm growth (Patient 5 and 6)

It can be observed in Figs. 4.39, that Patients 1, 2, 3 and 4 present higher pressure levels corresponding to the simulation obtained with the second year exam in relation to the first year. The opposite behavior can be seen for Patients 5 and 6 (Fig. 4.40), who show a decrease on the pressure level from the first to the second year results. These pressure distributions agree with the previous observations made with regard to the axial velocity profile.

By the results obtained, the pressure drop near the valve due to the flow expansion was equivalent for both patients. However, the observation regarding the pressure distribution of patients who had aneurysm growth with those who did not, allows us to corroborate the fact that high pressure may collaborate to increase an aneurysm, since patients who presented growth in the aneurysm presented a larger pressure variation over the years.

4.4.Turbulent Variables

In this section, different quantities related to the flow turbulence are discussed. Initially the turbulent kinetic energy is presented, followed by the turbulent shear stress tensor. Finally, coherent structures of the flow are discussed, with the aid of the Q-criteria.

4.4.1. Turbulent Kinetic Energy

The turbulent kinetic energy (TKE) κ represents the ‘strength’ of the turbulence in the flow, and caries the information of the three normal Reynolds stress tensor (Eq. 3.8). Patient 1 and Patient 6 were once again chosen to represent respectively, a case where there was of growth of the aneurysm and one that the aneurysm did not grow.

Figure 4.41 shows the turbulent kinetic energy distribution obtained corresponding to Patient 1. High turbulence values can be perceived near the entry and along the jet, until reaches the anterior wall, where aorta dilatation occurs. In addition, the region with high turbulent kinetic energy levels increases from the first to the second year. On the other hand, while examining the turbulent kinetic distribution corresponding to Patient 6 in Fig. 4.42, it can be seen low values of turbulent kinetic energy near the anterior wall and high values close to the posterior part of the aorta, do not accompanying the jet. Further, lower κ values are observed for Patient 6 when compared with Patient 1, and different scales had to be employed.

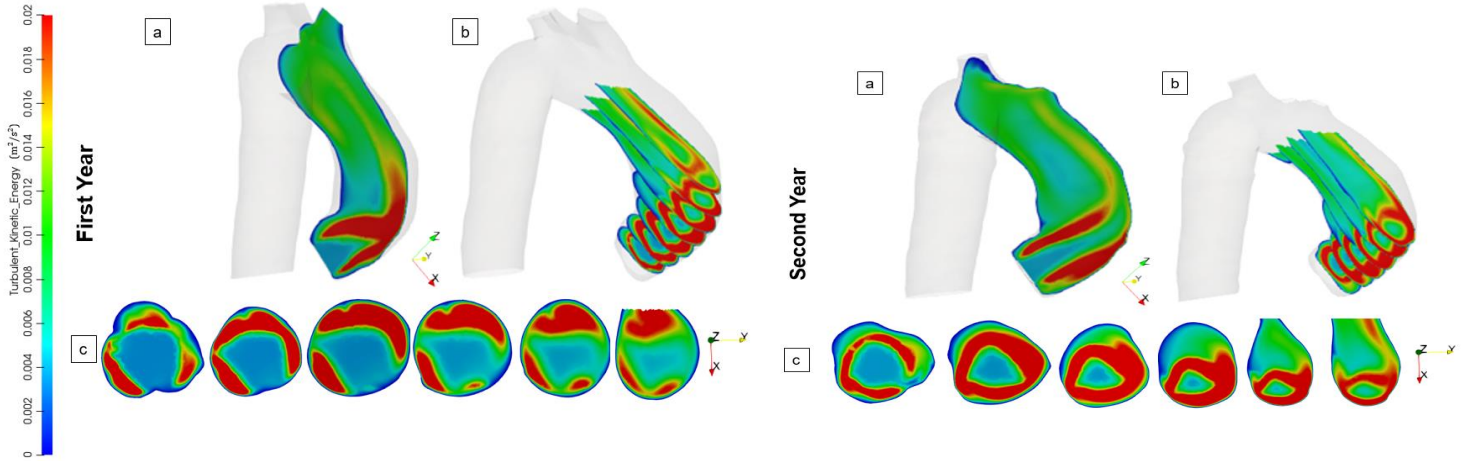

Figure 4.41 – Contours of Turbulent Kinetic Energy of Patient 1. (a) Transverse planes. (b) Central plane. (c) Cross-sectional individual plans

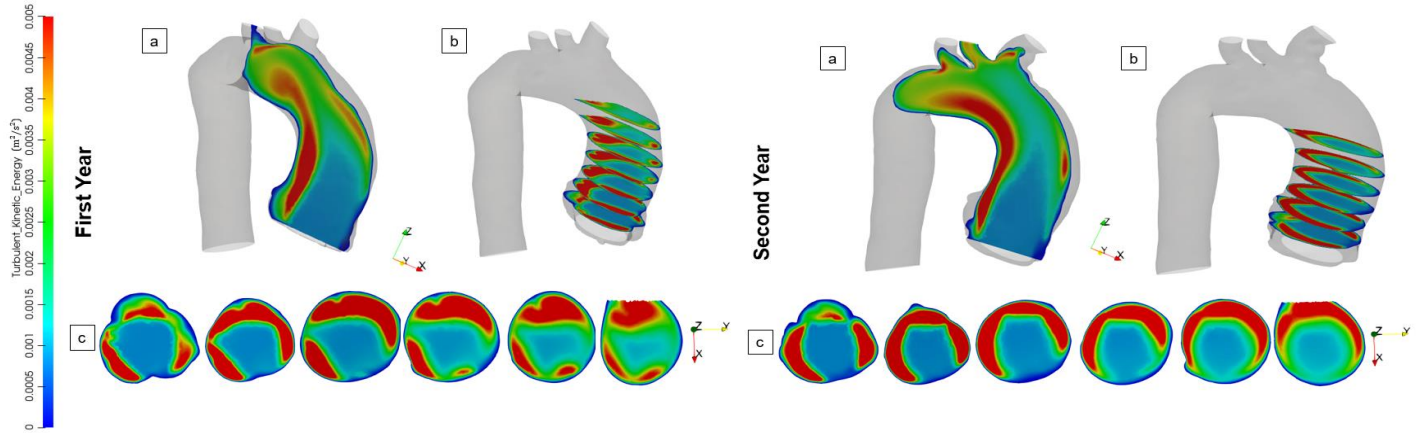

Figure 4.42 – Contours of Turbulent Kinetic Energy of Patient 6. (a) Transverse planes. (b) Central plane. (c) Cross-sectional individual plans

High shear rate leads to increase of the turbulent kinetic energy. Thus, it is expected to find high turbulent kinetic energy levels around the incoming jet, as well as near the aorta's surface. It has been observed by the results that for Patient 1 (with aneurysm growth), that because of the jet oriented to the anterior wall, both phenomena combined led to a high κ level at that region, where a larger aorta's dilatation occurs. For Patient 6, without aneurysm growth, since the incoming jet is more central, there is no combination of the phenomena that induce an increase of κ, resulting in lower κ values inside the domain and near the anterior wall.

An iso-surface of turbulent kinetic energy equal to κ=0.03 m^2/s^2 was created for Patient 1 and equal to κ=0.007 m^2/s^2 for Patient 6 and are shown in Fig.4.43. Analyzing Fig. 4.43, is possible to verify in the results for Patient 1, corresponding to the first year, that the iso-surface of high κ value is around the jet and it is directed to the anterior wall. This patient presented an aneurysm growth, i.e., an increase of the dilatation of the aorta's diameter was observed in the second year, and as a result, the high κ value iso-surface disappears from the anterior wall and it acquires a ring shape around the incoming jet. Patient 6 also shows the high κ iso-surface around the jet, but since the jet is more central, the high κ iso-surface does not reach the anterior surface, in fact, it is closer to the posterior wall, and similar formats can be seen in the results obtained for both years.

Turbulent kinetic energy is generated by the product of turbulent shear and deformation rate (Eq. 3.22), thus, high κ values near the anterior aortas wall can indicate a potential candidate to have an aneurysm increase.

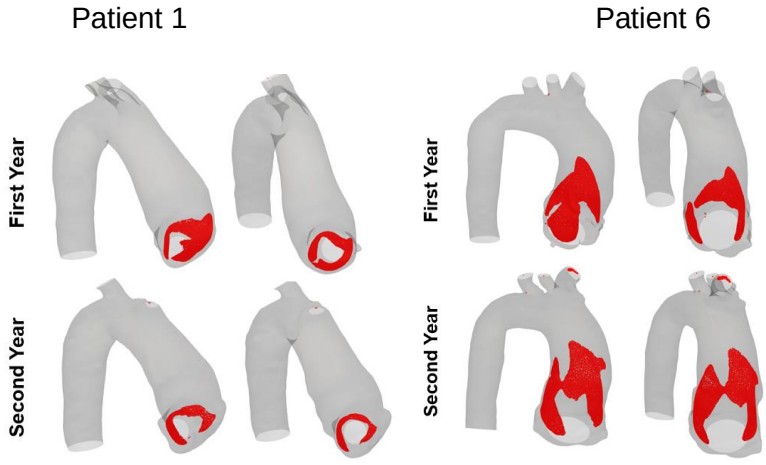

Figure 4.43 – Iso-surface of Turbulent Kinetic Energy of Patient 1 (κ=0.03 m^2/s^2) and Patient 6 (κ=0.007 m^2/s^2)

4.4.2. Turbulent Shear Stress

High levels of stress on the bloods cells are responsible for hemolysis and platelet activation (de Tullio et al., 2009). The level responsible of incipient hemolysis ranges from 400 N/m² to 5 000 N/m² (Sallam & Hwang, 1984). The investigation on the stress distribution is extremely important to evaluate its correlation to aneurysm growth.

As shown in Chapter 2, the stress distribution presents two contributions: the molecular diffusion, and the turbulent diffusion, represented by the turbulent Reynolds stress tensor, which is the dominant part. The Reynolds stress tensor presents six components and it varies at each point of the domain. However, when written in the principal coordinate system, it can be express in diagonal form, with only three principal normal stress σ_1, σ_2 and σ_3, ordered as $\sigma_1 \geq \sigma_2 \geq \sigma_3$. The identification of the principal normal stresses requires the solution of a third-order polynomial equation

$$\sigma^3 - I_1\sigma^2 + I_2\sigma - I_3 = 0 \tag{4.3}$$

where I_1, I_2 and I_3 are the three stress invariants of the tensor

$$I_1 = \overline{u'u'} + \overline{v'v'} + \overline{w'w'} \tag{4.4}$$

$$I_2 = \overline{u'u'} * \overline{v'v'} + \overline{v'v'} * \overline{w'w'} + \overline{u'u'} * \overline{w'w'} - \overline{u'v'}^2 - \overline{v'w'}^2 - \overline{u'w'}^2 \tag{4.5}$$

and I_3 is the determinant of the Reynolds stress tensor and *u'*, *v'* and *w'* the fluctuations in velocity vector components in the three Cartesian directions.

The maximum turbulent shear stress acting on a surface element (Malvern, 1977) is written as

$$TSS_{\max} = \frac{\sigma_1 - \sigma_3}{2} \tag{4.6}$$

In order to verify the existence of a correlation between the maximum turbulent shear stress distribution with a growth of the aorta's aneurysm, Patient 1 and Patient 6 were once more selected to represent both groups (with and without aneurysm growth). The TSS_{max} distribution is shown for both years in Figs. 4.44 and 4.45, corresponding to Patient 1 and 6, respectively.

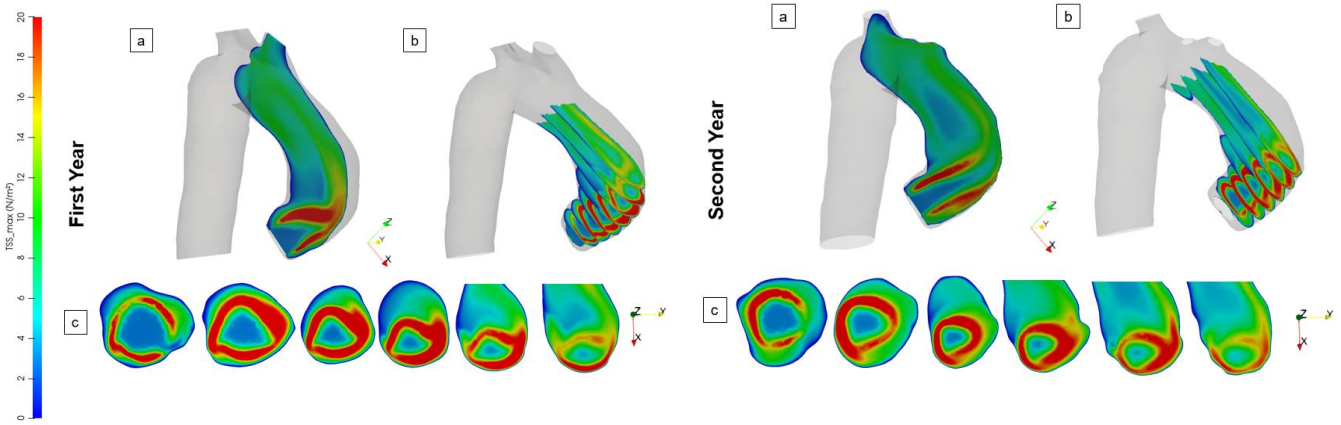

Figure 4.44 – Contours of Maximum Turbulent Shear Rate of Patient 1. (a) Transverse planes. (b) Central plane. (c) Cross-sectional individual plans

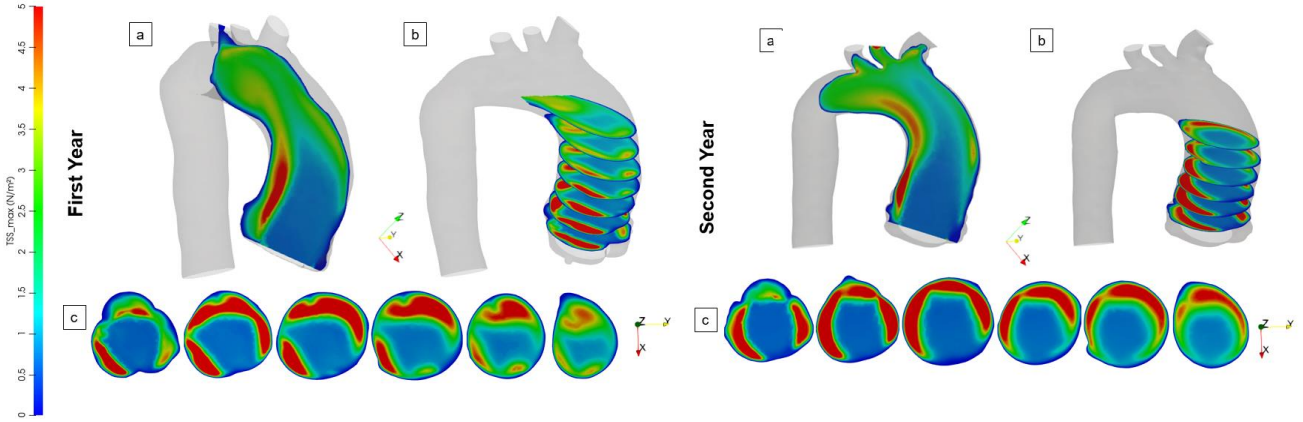

Figure 4.45 – Contours of Maximum Turbulent Shear Rate of Patient 6. (a) Transverse planes. (b) Central plane. (c) Cross-sectional individual plans

Patient 1 (Fig. 4.44) shows higher values of TSS_{max} near the anterior aorta wall, where the aneurysm growth is significant, while for Patient 6 (Fig. 4.45) the maximum value occurs in a region near the posterior wall. High values of turbulent shear stress caused by the frictional force acting on the endothelial cell surface, according to Malek et al. (1999), may contribute to aneurysm's growth or rupture of the wall.

To complement the information presented in the previous figures, a high value iso-surface of the maximum turbulent shear stress was plotted for each patient, corresponding to the results of both years. Figure 4.46 presents the iso-surface equal to $TSS_{max} = 20$ Pa for Patient 1. Since lower levels of TSS_{max} were observed for Patient 6, the iso-surface equal to $TSS_{max} = 5$ Pa was selected. In all results, it can be seen that the maximum turbulent shear stress occurs at the periphery of the inlet jet, near the aortic valve. Since the inlet jet is directed to the anterior wall for Patient 1, the surface with $TSS_{max} = 20$ Pa presents a ring shape slightly displaced toward that region. On the other hand, the TSS_{max} iso-surface of Patient 6 shows the maximum turbulence shear stress acting at the posterior part of aorta.

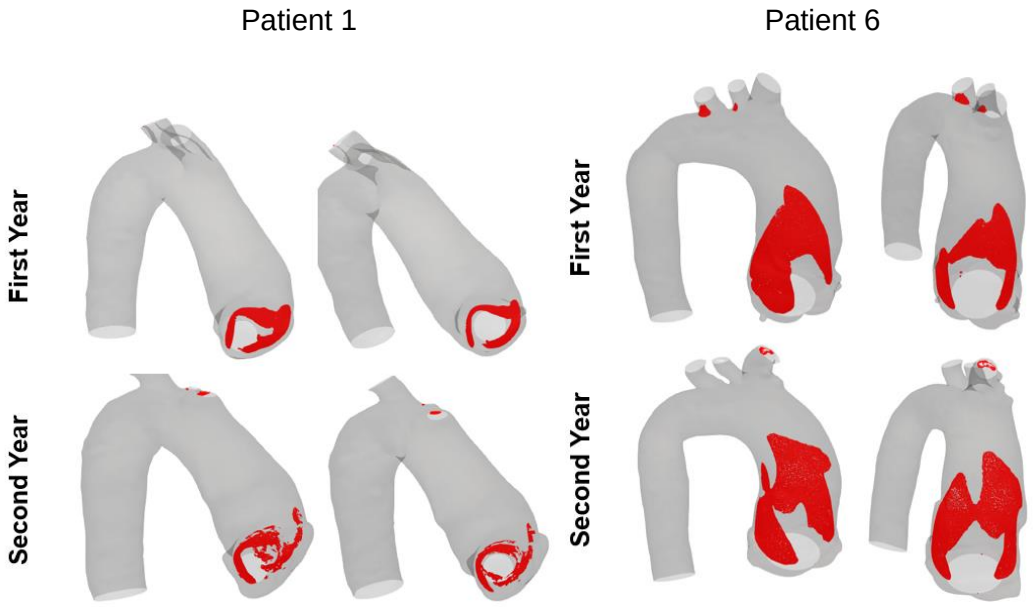

Figure 4.46 – Iso-surface of Maximum Turbulent Shear Rate of Patient 1 and 6

The results presented of the turbulent shear rate for Patients 1 and 6 are quite similar to the results presented in the turbulent kinetic energy section. Les et al. (2010) established the relationship between the two variables. Turbulence kinetic energy and the Reynolds stresses both rely on a decomposition of the flow field into an average and fluctuating part, but the Reynolds stress computation is

the ensemble of different components of the fluctuating velocity field $\sigma_{Re} = \rho\,\overline{u_i'\,u_j'}$. When turbulence is high, it can be assumed that the fluctuating velocity fields are similar in magnitude ($|u_x'| \approx |u_y'| \approx |u_z'|$). In this way, according to Les et al. (2010) the turbulent kinetic energy κ can relate to σ_{Re} as

$$\kappa = \frac{1}{2}\rho\left(\overline{u_x'^2} + \overline{u_y'^2} + \overline{u_z'^2}\right) \approx \frac{3}{2}\left(\rho\,\overline{u_i'^2}\right) = \frac{3}{2}\,\sigma_{\mathrm{Re}} \tag{4.7}$$

Thus, the identification of regions with peaks of the turbulent kinetic energy can be related to the appearance of peaks of the maximum turbulent shear stress.

4.4.3. Coherent Structures: Q-criterion

Biasetti et al. (2011) have correlated the presence of vertical structures with high shear stress in patients with abdominal aortic aneurysm. Thus, the purpose of this section is to visualize coherent structures inside the ascending aorta. The differences in the flow structure of the patients of the two different groups (with and without aneurysm growth) may indicate a particular behavior that might help to identify the possibility of aneurysm growth. To this end, one good parameter to visualized turbulent coherent structures is the Q-criterion.

The Q-criterion is obtained from the flow field, depending both on the strain rate tensor S_{ij} (Eq. 3.6) and vorticity tensor Ω_{ij}, corresponding to the symmetric and anti-symmetric part of the velocity gradient tensor. It is defined as

$$Q = \frac{1}{2}\left(\Omega_{ij}\;\Omega_{ij} - S_{ij}\;S_{ij}\right) \tag{4.8}$$

where Ω_{ij} is

$$\Omega_{ij} = \frac{1}{2}\left(\frac{\partial u_i}{\partial x_j} - \frac{\partial u_j}{\partial x_i}\right) \tag{4.9}$$

A positive *Q* means a domination of the vorticity magnitude over the strain rate. Low pressure regions can also be related to a coherent structure, and the Q-criteria can be related to the pressure through its Poisson equation, obtained by a combination of the conservation equations of mass and momentum for an incompressible fluid, as

$$Q = \frac{1}{2\rho}\nabla^2 p \tag{4.10}$$

Figures 4.47 and 4.48 present Q iso-surface plotted with different positive values that made possible to visualize the coherent structures within the aorta, for all cases. Figure 4.47 corresponds to patients with aneurysm growth and 4.48 for patients without growth. Each Q iso-surface was colored with the dimensionless modulus of the velocity vector, on a scale represented on the right side of the figures.

Analyzing Fig. 4.47 corresponding to Patient 1, structures that can be identified as hairpin vortex can be seen hitting the distal wall for both years. The angular curvature of Patient 1 may cause the formation of a detached vortex. Patient 2 does not have such an angular curvature, but also presents a noticeable growth in the volume of the aneurysm. This patient presents a toroidal vortex next to the wall with medium velocity values. The same phenomenon occurs for Patient 3. Examining the Q iso-surface for Patient 4, it can be seen that the flow field obtained with the first exam presents a toroidal vortex form with high velocities. It is important to mention that in the second year the coherent structures present a different form, it is possible to perceive a beginning of hairpin close to the wall, as it has been shown for Patient 1.

Those patients showed that the flow remained attached to the walls during the systole. As discussed in Chapter 2, as well as mentioned in the study of Weigang et al. (2008), it is possible to visualize for some aneurysmal grew cases, a formation of large rotational regions, forming a vortex ring, with a central jet and two large vortices.

Figure 4.48 corresponds to the flow field obtained for the patients that the aneurysm did not grow. Similar structures can be seen for both years, for both patients, i.e., coherent structures in a toroidal format are present around the inlet jet. Lower velocities levels were achieved in these structures when compared with patients with aneurysm growth.

Since the vortex stretching with higher values is stronger and occurs in the patients that aneurysm grew, is possible to infer that in these cases the flow is likely to be more disturbed. Another possible consideration is that the flow inside the aneurysm contains dominant regions of flow separation, which is responsible for composing coherent structures presents along the aorta. In disturbed cases, that separation occurs in regions closer to the entrance of the jet.

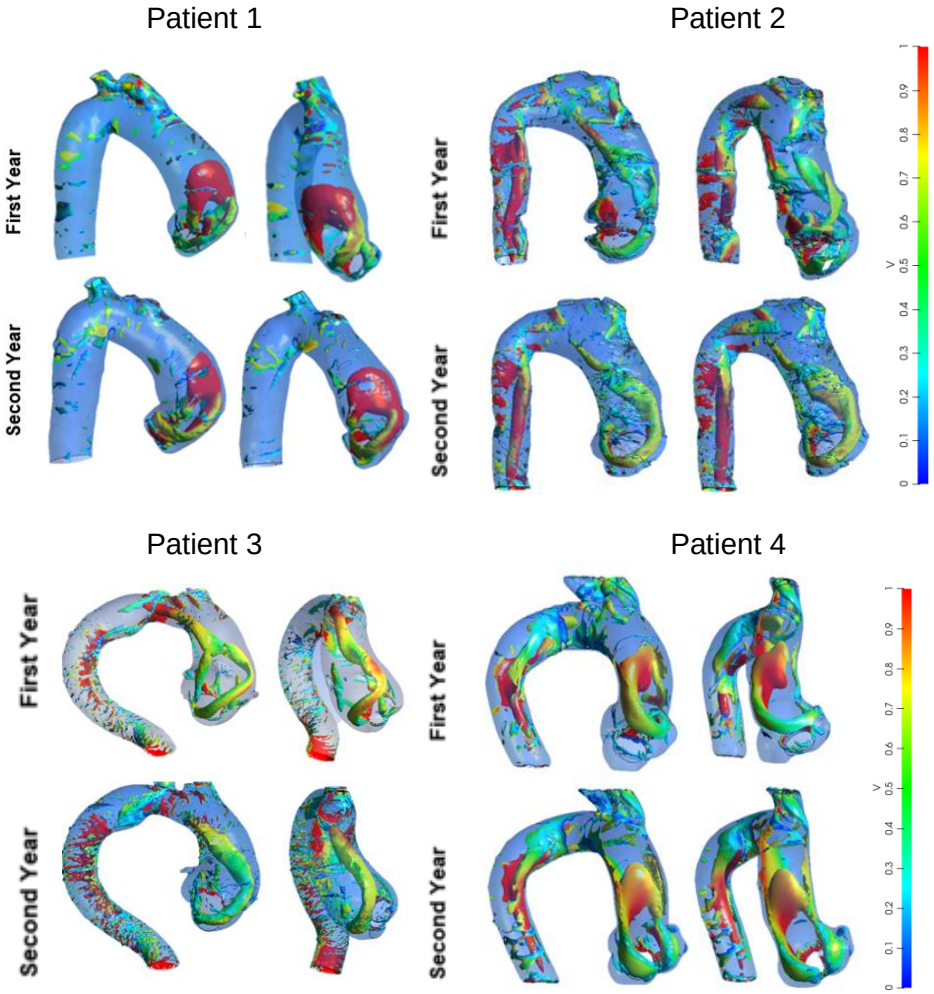

Figure 4.47 – Iso-surface of Q-criterion for Patient 1, 2, 3 and 4 (with aneurysm growth)

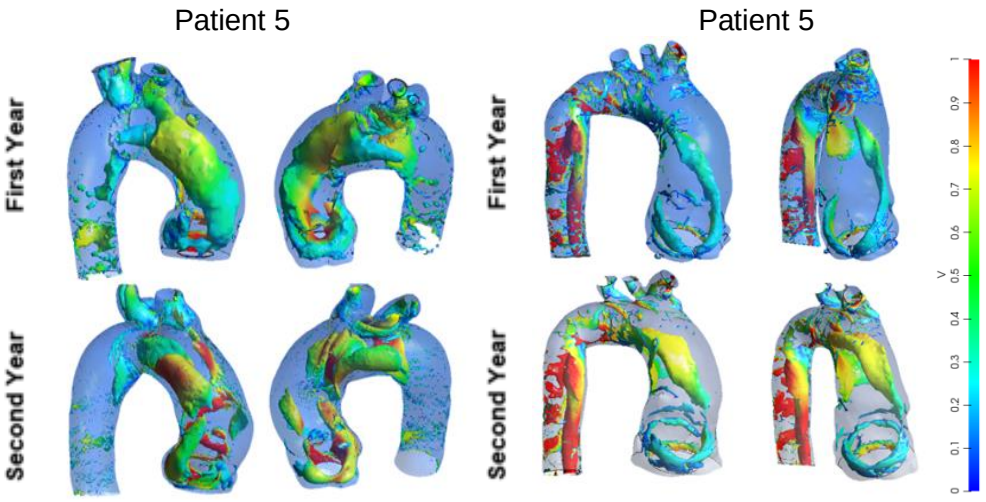

Figure 4.48 – Iso-surface of Q-criterion for Patient 5 and 6 (without aneurysm growth)

4.5. Aortic Wall Stresses

In this section tangential and normal stresses at the aorta's wall are presented. First, the tangential contribution is presented, i.e., the wall shear stress (WSS) defined as the gradient of the tangential velocity component to the wall in the normal wall direction as

$$\tau_w = \mu \frac{\partial u_t}{\partial n}\bigg|_w \tag{4.11}$$

Then, the normal contribution (pressure) distribution is examined.

To aid to identify similar distributions related to the two groups of patients, average values at the main area of interest of the ascending aorta, A_{ref}, (as defined in Fig. 4.4) are determined as

$$\phi_{av} = \frac{1}{A_{ref}} \int_{A_{ref}} \phi \, dA \tag{4.12}$$

Here, A_{ref} is the superficial aorta's area in the region of interest.

4.5.1. Wall Shear Stress

As mentioned in Chapter 2, the effects of WSS can be related to aortic dilatation. In order to evaluate the variations of shear stress at the aortic wall, the wall shear stress distributions were analyzed for each patient in Figs. 4.49 and 4.50, corresponding to the groups with and without aneurysm growth, respectively.

Analyzing the WSS distribution in Fig. 4.49, corresponding to the Patient 1, with aneurysm growth, a large region with high values of WSS is observed in anterior wall of the aorta for both years. It can also be clearly observed an increase in the size of the high WSS regions at the ascending aorta. Patient 2 presents a more non-uniform WSS distribution, with peaks of high shear. The same can also be observed along the surface of the aorta of patients 3 and 4. However, due to the strong curvature of the aorta of Patient 3, the region with high WSS is displaced upwards, near the brachiochephalic artery. Further, both patients 2 and 3, present a much larger ascending aorta diameter than their descending part. Thus, due to the smaller diameter at the descending aorta, high velocities are obtained and consequently high WSS due to higher velocity gradients.

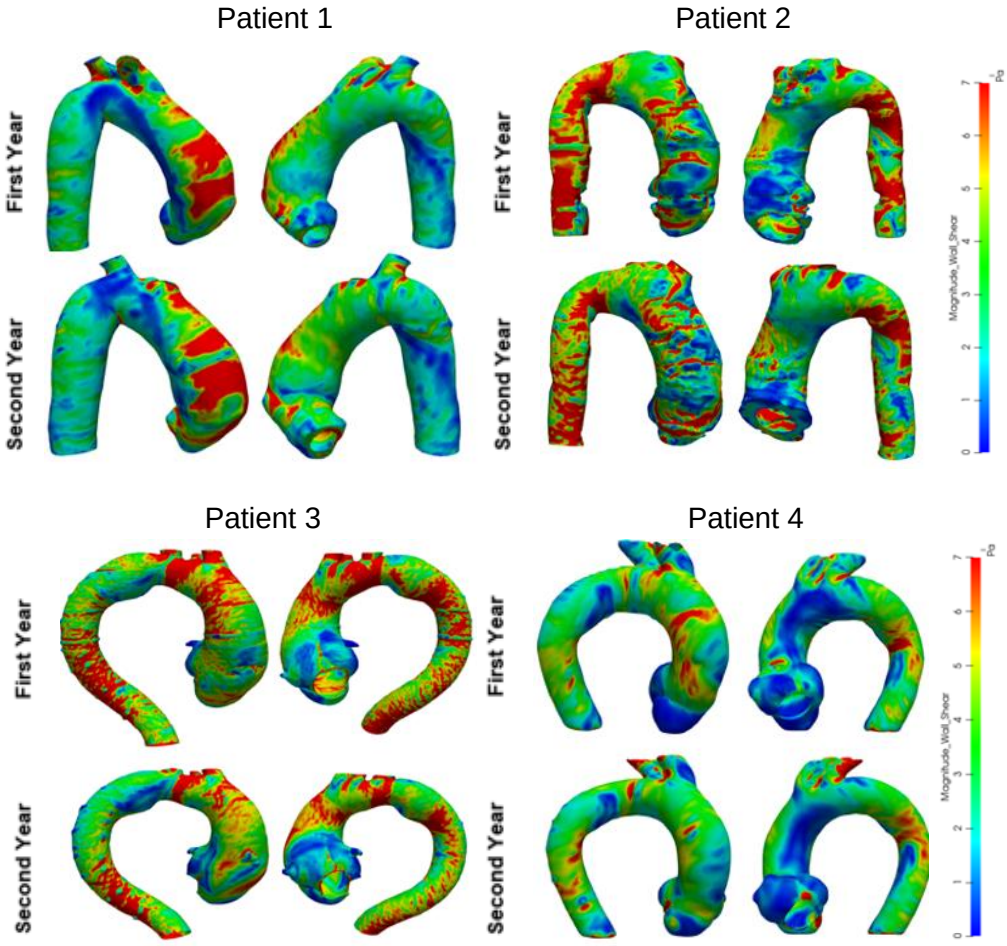

Figure 4.49 – Contours of Wall Shear Stress (WSS) for Patient 1, 2, 3 and 4 (with aneurysm growth)

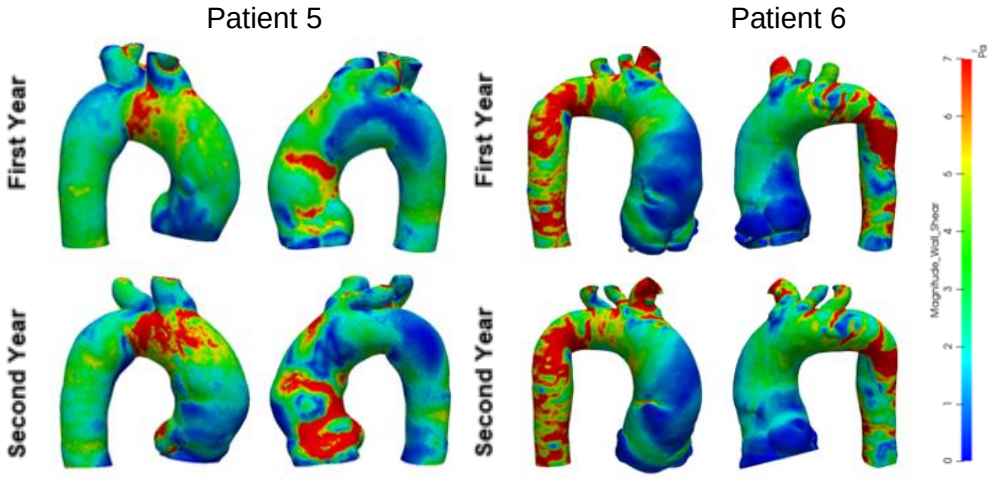

Figure 4.50 – Contours of Wall Shear Stress for Patient 5 and 6 (without aneurysm growth)

Analyzing the WSS distribution of the patients who did not present an aneurysm growth in Fig. 4.50, there are two different observations that can be made. First, it can be observed that Patient 5 presents high WSS in the aorta

posterior wall, as well as, high WSS at the upper part of the aorta, near the brachiochephalic artery. For this patient, due to the strong aorta's curvature near the entrance, the incoming jet impinges at higher positions and it is also directed to the posterior wall. Patient 6 presents low WSS values in the main area of interest. Due to the smaller diameter of the descending aorta, high WSS values are observed in this region, but since the aneurysm typically occurs at the ascending part, this region is not relevant for the present study.

Aiming to identify some similarities between the patients of each group, the size of the area with high shear rate in the region of interest was determined for each case. To this end, the ratio of the superficial area with WSS within a certain range to the area of interest of each particular patient was determined, and the results are shown in Fig. 4.51. Three ranges were defined: high WSS, for values above 7 Pa, low WSS for values below 5 Pa and intermediate values between 5 and 7 Pa. The symbol F corresponds to the results obtained with the aortas corresponding to the first year of scan and S for the second year.

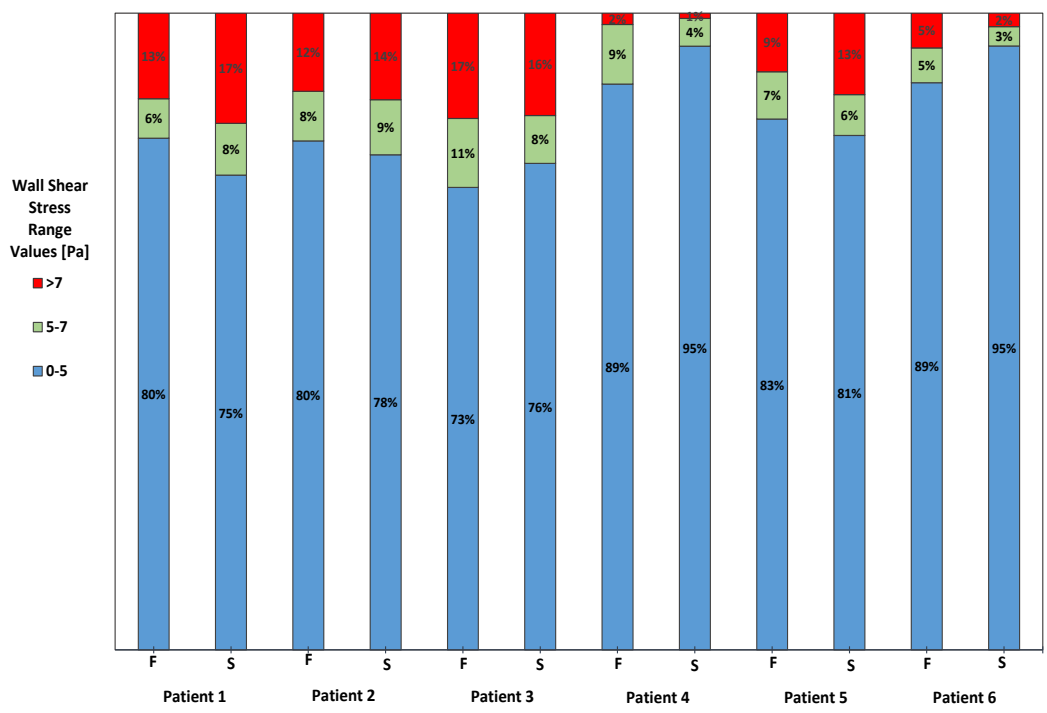

Figure 4.51 – Percentage distribution of WSS on main area of interest of patients in first (F) and second (S) years of examination

Figure 4.51 shows that Patients 1, 2 and 3 have high values of WSS distributed in the more than 12% of the main area of interest during the first year. The area WSS area increases in the second year for Patients 1 and 2, and it is almost constant for Patient 3. Although Patient 4 has been classified as presenting

an aneurysm growth, this patient does not present a significant region with high WSS, but the percentage size of the area with intermediate WSS is equivalent to the other 3 patients with aneurysm. Patient 5 presents a large percentage area with high WSS, equivalent to the size of the area of patients with aneurysm. However, the high WSS region is located in the posterior part of the aorta. Finally, only at a small area of the ascending aorta of Patient 6, high WSS can be found.

To better quantify the differences on the WSS levels of each patient corresponding to the first and second year, the average value at the superficial area of interest was determined and it is shown in Table 4.7, which also presents the percentage variation from the WSS values obtained during the first year in relation to the second year.

Table 4.7 – Mean WSS at the area of interest of each patient

Patient	**Year**	**1**	**2**	**3**	**4**	**5**	**6**
$\overline{WSS}$ [Pa]	**F**	3.79	3.37	3.85	2.35	2.54	1.58
	S	4.15	3.88	3.66	2.35	3.34	1.46
Δ [%]		9.7	14.9	-5.0	0.0	31.8	-7.7

Patients 1, 2 and 3, who were identified as presenting an aneurysm growth presented an average WSS value of about 3.5 Pa during the first year, but lower level was measured for Patient 4. Patient 5 without aneurysm growth presented an equivalent average WSS value than Patient 4, and the smallest WSS average value of obtained for Patient 6. Comparing the average WSS variation between the two years of all patients, not conclusive results were obtained since the WSS level has increased for some patients, has decreased for another, independent if the patient presented or not an aneurysm growth.

4.5.2. Wall Pressure

The pressure distribution at the aortic wall is examined in this section for all patients, in an analogous form as it was done with the WSS in the previous section. Initially, contours of relative pressure in relation to the valve inlet ($p - p_{in}$) are presented for both years in Figs. 4.52 and 4.53, corresponding to the two groups of patients. Then, the size of the area with high pressure in the region of interest is presented in Fig. 4.54. Finally, average pressure values are shown in Table 4.8.

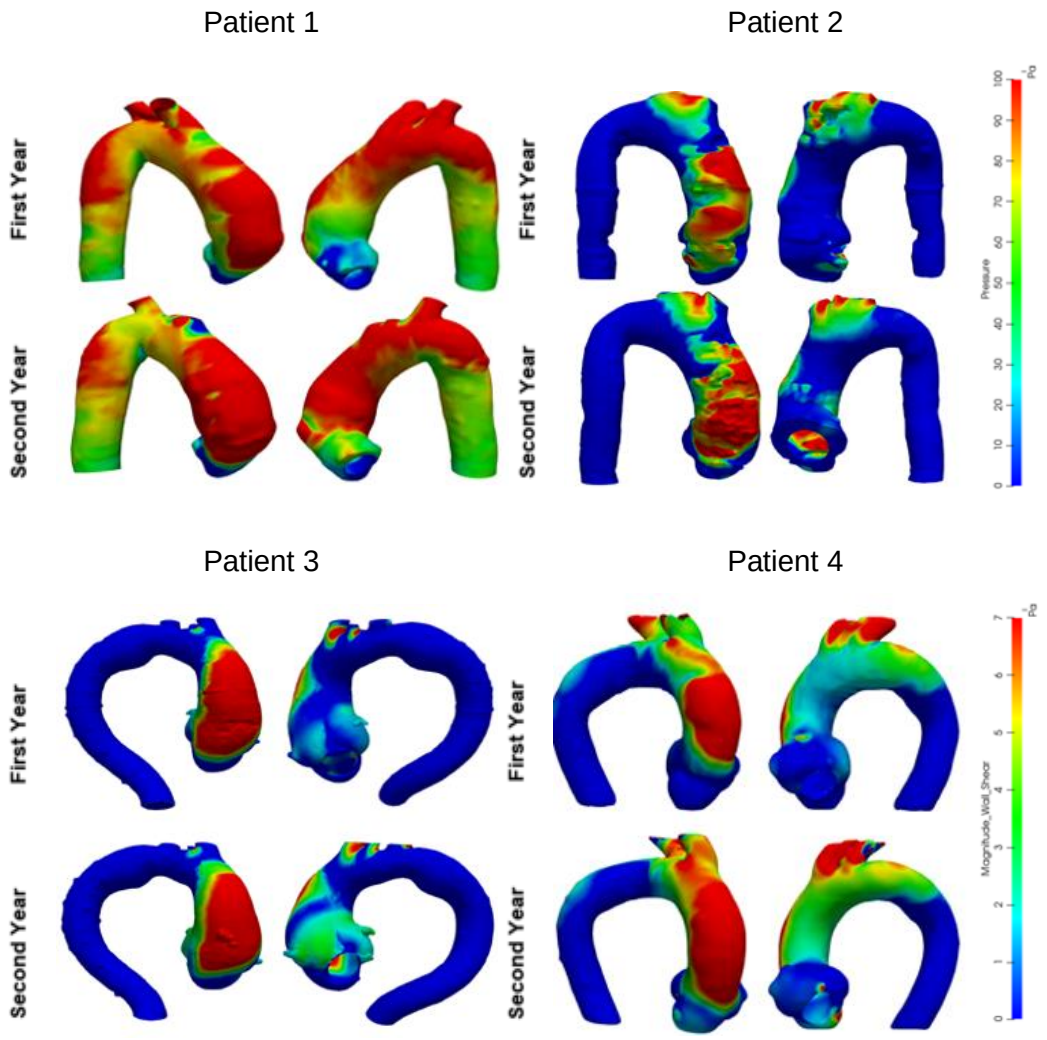

Figure 4.52 – Contours of Wall Pressure for Patient 1, 2, 3 and 4 (with aneurysm growth)

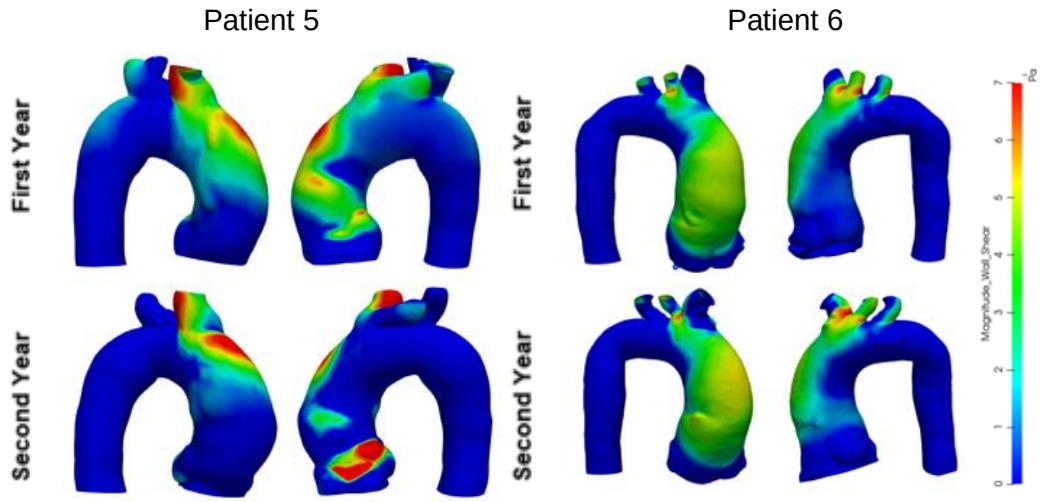

Figure 4.53 – Contours of Wall Pressure for Patient 5 and 6 (without aneurysm growth)

Figure 4.52 shows the relative pressure at the aortic wall of all patients that presented an aneurysm growth. It can be seen for all patients, high pressure values at the ascending part of the aorta, which is mainly due to the aortic wall jet impingement. It can also be seen for all patients, low pressure values very close the aortic root, due to the jet expansion after leaving the aortic valve. Larger pressure values can be seen for Patient 1, and equivalent distributions for the other three patients.

Figure 4.53 shows the wall pressure distribution for Patients 5 and 6, who did not present aneurysm growth. Lower values were obtained when compared with the pressure levels of the other group. Patient 5 has high pressure near the arch and in the posterior wall, corroborating what was presented in WSS section. Patient 6 did not present high pressure levels in the region of interest, since his aortic valve presented the largest diameter, leading to smaller velocities, shear rate and pressure.

The pressure ranges were also defined to evaluate the size of the superficial area with pressure with a certain range. The small pressure levels were considered for relative pressure inferior to 50 Pa, intermediate between 50 and 100 Pa and large values above 100 Pa. Once again, the symbol F indicated results related to the first year exam and S for the second year. Examining the Fig.4.54, it can be seen that Patients 5 and 6, without aneurysm growth presented the smallest areas with high pressure. Patients 1, 3 and 4 present more than 18% of the area of interest with high pressure values. Although for the threshold of 100 Pa, the percentage of the ascending aorta of Patient 2 is equivalent to the patients without aneurysms growth, when the intermediate range is also considered, all patients with aneurysm growth present a much larger superficial area with high pressure than the patients without aneurysm growth. Small variation of the percentage area of high pressure (above 100 Pa) was obtained for all cases, between the results of the exams realized in different years, with the size increasing or decreasing from one year to the other, without a clear pattern. However, if the area of intermediate pressure level is also accounted for, then the size of the region with critical pressure is larger for patients with aneurysm growth, further the size of the area increases from one year to the other, while the percentage area size decreases for the patients of other group, without growth.

The average relative wall pressure at the area of interest of the ascending aorta is presented in Table 4.8. Analyzing the results, it is important to emphasize that all patients diagnosed with increased aortic dilatation had also an increase in wall pressure values from one year to another. Patients 5 and 6, without aneurysm

growth, presented a reduction of the mean pressure between the two years results. The wall pressure distribution and its level seems to be a very important variable to be controlled to aid in the diagnostic of possible growth of the aortic aneurysm.

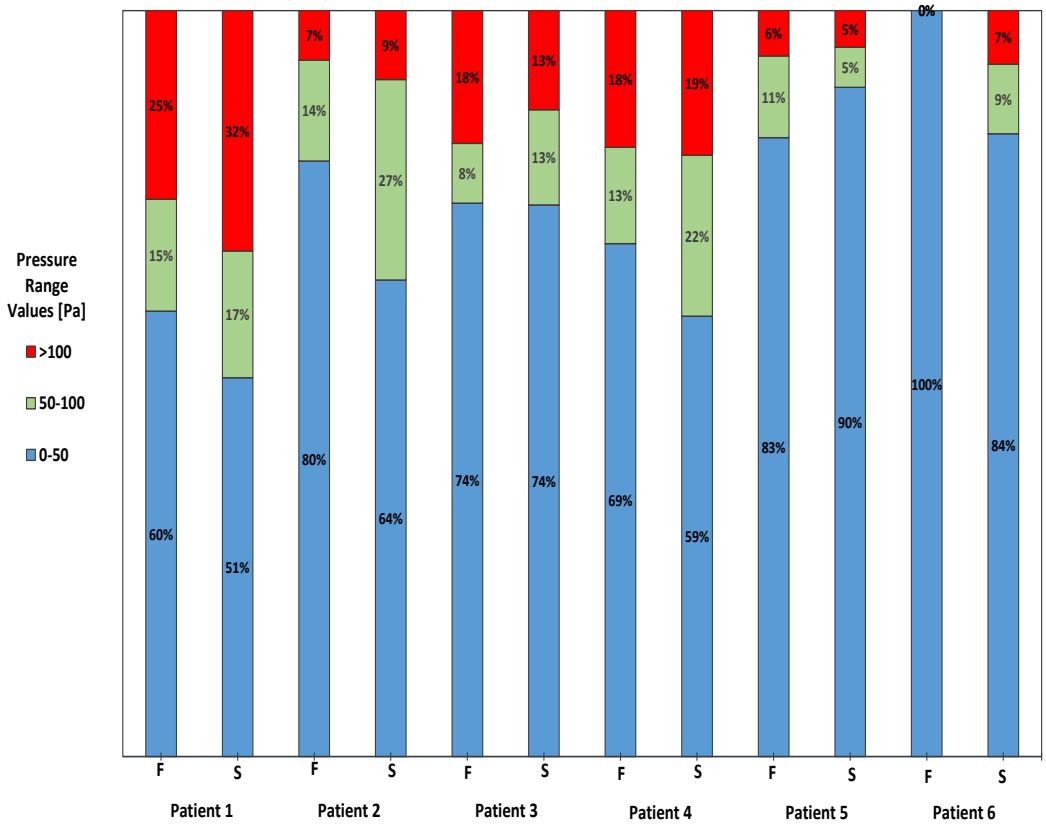

Figure 4.54 – Percentage distribution of wall relative pressure on main area of interest of patients in first (F) and second (S) years of examination

Table 4.8 – Mean relative wall pressure at the area of interest of each patient

Patient	Year	1	2	3	4	5	6
$\bar{P}$ [Pa]	F	91.2	13.3	31.0	40.0	18.4	22.6
	S	110.0	32.8	41.2	46.0	8.4	22.4
Δ [%]		20.6	147.0	32.8	15.0	-54.1	-2.1

5
FINAL REMARKS

The main purpose of the present work is to identify some flow characteristic that might be associated with the growth of an ascending aortic aneurysm (AAoA). To this end, the blood flow in the ascending aorta of six different patients with aneurysmal dilatation, at two different years, has been numerically investigated. The 3D modeling of each geometry was performed from images obtained by angiotomography exams. The patients were classified in two groups depending if a growth of the ascending aorta's aneurysm had been identified or not during the time interval of the exams. To define the computation domain, first a segmentation of each image had to be performed, and then a mesh was generated.

The focus of the study is to analyze a critical situation during the cardiac cycle in the systolic period. The critical condition corresponds to the peak of the flow rate through the aortic valve, when high shear rates are expected. Further, during mostly of the whole systolic period, the aorta presents its maximum distension, with less complacency. Therefore, in accordance with that situation, the present analysis was performed considering a steady state regime at the critical flow rate, the aortic wall assumed as rigid and the blood was modeled as a Newtonian fluid.

From the results obtained it was observed that patients with growth in the aorta had the jet directly impacting the anterior wall, while those without growth, the jet followed along the aorta or it was directed to the posterior wall. It was also observed that patients with aortic growth have shown strong recirculation in the back of the jet. Another observation was that after the time interval of the exams, patients with aneurysmal growth presented the jet being more proximal to the inlet valve, resulting in higher axial velocity impacting the aortic wall. Patients who the aneurysm did not grow had the jet more distal from the inlet jet. The analysis of the x- and y- velocity components did not present any major difference between the results obtained from the two exams of the two different years for both patients' group.

For all patients, it was shown similarities of maximum Reynolds shear stress and turbulent kinetic energy distributions. High turbulent kinetic energy was observed around the inlet jet and near the aortic wall. For the group of patients who

presented aneurysm growth, since the incoming jet impinges more strongly at the anterior wall, both effects are combined inducing higher level of turbulent near the anterior wall.

An important result of the analysis was the different coherent structures between the patients of the two groups. Toroidal structures with low velocities were observed for the patients who did not present an aneurysm growth. Two types of structures were identified in the group of patients who presented aneurysm growth: hairpin structures and toroidal structures with high velocities.

At the ascending aorta's area of interest, high values of WSS at the anterior wall were observed in the patients that the aneurysm grew. The mean WSS variation form one year to the next was not conclusive, with the mean value increasing or decreasing for patients of both groups.

The pressure loss due to the jet expansion as soon as it enters the aorta was equivalent among all patients. For all patients, it was also observed high pressure at the impinging jet region of the aorta's wall, due to the fact that at the stagnation point, the pressure is maximum. In this incident jet region, the shear stresses are not high. However, at the boundary of the high-pressure region, the shear stress presents a growth, influenced by the presence of the recirculation regions next to the aortic valve. At the recirculation regions, the flow velocity is low, the velocity vector changes direction, impacting on the aortic wall. Higher pressures, especially at the anterior wall, were observed for the patients who presented an aneurysm growth in relation to those that did not present. Further, patients who presented an increase of the aneurysm diameter, showed a pressure level increase between the time interval of the two exams, while it has decreased for the other group.

One interesting parameter to aid identify in which group it is expected to find a patient is the angle of entry of the aortic geometry with the branchiocephalic trunk, which is directly linked to the patient's anatomy. It was observed that for patients with angulation greater than 100º after the onset of the aneurysm, growth was positive over the years. The format of the aorta is directly connected to the flow, since due to the aorta's shape, the incoming jet can be imping at the anterior wall. This fact raise the levels of pressure and shear stress, inducing the formation of hairpin structures with high levels of turbulence. It could be associated with flow recirculation. These phenomena were observed in the group who presented aortic aneurysm increase, thus it might contribute to the aortic remodeling process.

At Table 5.1 the main conclusions related to each group of patients are presented schematically.

Table 5.1 – Schematically conclusions of each group of patients

Patients that aneurysm grew	***Patients that aneurysm did not grow***
Inlet jet directed to the wall, hairpin vortices located closer to the wall and toroidal structures with high velocities	Inlet jet is not directed to the wall, vortices in a toroidal form with low velocity
Jet being more proximal to the inlet valve: resulting in higher impact to the aortic wall	The jet gets more distal from the inlet jet
Significant higher pressure levels and larger superficial area with high pressure, resulting in a pressure increase between time interval	Neglible or decreased pressure variation
Strong recirculation in the back of the jet	
High levels of turbulent kinetic energy and maximum turbulent shear stress near the anterior wall	
High values of WSS at the anterior wall	

Based on the results obtained, in order to improve the prognosis of patients, it is necessary to consider several factors that may influence the growth of the aortic aneurysm. The angle between the aortic inlet and the brachiocephalic trunk could be an important feature to be considered, as well, the considerations by the physician about the age and the medicine that patient takes. Then, by numerically determining the flow field, the existence of all factors mentioned should be examined in order to signal the mechanical stimulus of aortic remodeling process.

To conclude, it can be remarked that this research has the potential in several aspects to generate subsequent works, for example, establish threshold values of angulation, pressure and shear stress. It is recommended that the

present type of analysis should be applied to a greater number of cases. Some of the hypothesis made to simplify the problem in order to obtain a solution in a viable time could be relaxed. Per example, the influence of different additional parameters such as elasticity, transient flows (how occurs the flow during the diastole period) and the blood constitutive equation can be examined. Future studies with a larger number of patients and longer follow-up time are needed to define the relationship between blood flow pattern and aortic remodeling. All these aspects can contribute to a better prognosis in medicine and the development of bioengineering.

REFERENCE

ADRIAN, R.J. **Hairpin vortex organization in wall turbulence**. Physics of Fluids, v. 19, n. 4, 041301, 2007.

AKHMETOV, D.G. **Vortex rings***.* 1. ed. Berlin: Springer, 2009.

ALASTRUEY, J.; XIAO, N.; FOK, H.; SCHAEFFTER, T.; FIGUEROA, C.A. **On the impact of modelling assumptions in multi-scale, subject-specific models of aortic haemodynamics.** J. R. Soc. Interface, v. 119, n. 13, 20160073, 2017.

ALBUQUERQUE, L.C.; PALMA, J.H.; BRAILE H. **Diretrizes para a cirurgia das doenças da aorta**. Arq Bras Cardiol, v. 82, n. 5, p. 35-50, 2004.

ASAKURA, T.; KARINO T. **Flow patterns and spatial distribution.** Circulation Research, v. 4, n. 66, p.1054-1066, 1990.

BÄCK, M.; GASSER, T.C.; MICHEL, J.B.; CALIGIURI, G. **Biomechanical factors in the biology of aortic wall and aortic valve diseases**. Cardiovascular Research, v.99, n.2, p. 232-241, 2013.

BALLYK, P.D.; STEINMAN, D.A.; ETHIER, C.R. **Simulation of non-Newtonian blood flow in an end-to-end anastomosis**. Biorheology, v. 31, n. 5, p. 555-586, 1994.

BARBEE, J.H. **The effect of temperature on the relative viscosity of human blood.** Biorhelogy, v.10, n.1, p. 1-5, 1973.

BENIM, A. C.; NAHAVANDI, A.; ASSMANN, A.; SCHUBERT, D.; FEINDT, P.; SUH, S.H. **Simulation of blood flow in human aorta with emphasis on outlet boundary conditions**. Applied Mathematical Modelling, v. 7, n. 35, p. 3175-3188, 2011.

BETTS, J.; **Anatomy & physiology**. OpenStax College, Rice University, p. 787-846, 2013

BIASETTI, J.; HUSSAIN, F.; GASSER, T.C.; **Blood flow and coherent vortices in the normal and aneurysmatic aortas:** A fluid dynamical approach to intra-luminal thrombus formation. J.R. Soc. Interface, v. 8, n. 63, p. 1449-1461, 2011.

BIEGING, E.T.; FRYDRYCHOWICZ, A.; WENTLAND A.; LANDGRAF, B.R.; JOHNSON, K.M.; WIEBEN, O.; FRANÇOIS, C.J. **In vivo three-dimensional mr wall shear stress estimation in ascending aortic dilatation**. Journal of Magnetic Resonance Imaging, v.33, n.3, p. 589-597, 2011.

BODNÁR, T.; SEQUEIRA, A; PROSI, M. **On the shear-thinning and viscoelastic effects of blood flow under various flow rates**. Applied Mathematics and Computation, v. 217, n. 11, p. 5055-5067, 2011.

BORAZJANI, I.; GE, L.; SOTIROPOULOS, F. **Curvilinear immersed boundary method for simulating fluid structure interaction with complex 3D rigid bodies**. Journal of Computational Physics, v. 227, n. 16, p. 7587-7620, 2008.

BUNCHMANN, N.A.; ATKINSON, C.; JEREMY, M.C. **Tomographic particle image velocimetry investigation of the flow in a modeled human carotid artery bifurcation**. Experiments in Fluids, v. 50, n. 4, p. 1131-1151, 2011.

BÜRK, J.; BLANKE, P.; STANKOVIC, Z.; BARKER, A.; RUSSE, M.; GEIGER, J.; FRYDRYCHOWICZ, A.; LANGER, M.; MARKL, M. **Evaluation of 3D blood flow patterns and wall shear stress in the normal and dilated thoracic aorta using flow-sensitive 4D CMR**. Journal of Cardiovascular Magnetic Resonance, v. 14, n. 1:84, p.1-11, 2012.

CARO, C.G.; FITZ-GERALD, J. M.; SCHROTER, R.C. **Atheroma and arterial wall shear observation, correlation and proposal of a shear dependent mass transfer mechanism for atherogenesis**. Proceedings of the Royal Society of London, v. 1046, n. 177, p. 109-159, 1971.

CECCHI, E.; GIGLIOLI, C.; VALENTE, S.; LAZZERI, C.; GENSINI, G.F.; ABBATE, R.; MANNINI, L. Role of hemodynamic shear stress in cardiovascular disease. Atherosclerosis, v. 214, n. 2, p. 249-56, 2011.

CELIS TORRES, D.F. **Numerical study of the influence of tilt valve angle on blood flow in a aortic model**. 2017. 115 f. Master Thesis. Departamento de Engenharia Mecânica, Pontifícia Universidade Católica do Rio de Janeiro, Rio de Janeiro, 2017.

CHEN, L.; WANG, X.; CARTER, S.A.; SHEN, Y.H.; BARTSCH, H.R.; THOMPSON, R.W.; COSELLI, J.S.; WILCKEN, D.L.; WANG, X.L.; LEMAIRE, S.A. **A single nucleotide polymorphism in the matrix metalloproteinase 9 gene (−8202A/G) is associated with thoracic aortic aneurysms and thoracic aortic dissection**. The Journal of Thoracic and Cardiovascular Surgery, v. 131, n. 5, p. 1045-1052, 2006.

CHIEN, S.; USAMI, S.; DELLENBACK, R. J.; GREGERSEN, M. I. **Shear-dependent deformation of erythrocytes in rheology of human blood.** American Journal of Physiology, v. 219, n. 1, p. 136-142, 1970.

CHO, Y.I.; KENSEY K.R. **Effects of the non-Newtonian viscosity of blood on flows in a diseased arterial vessel**. Part 1: Steady flows. Biorheology, v. 28, n. 3-4, p. 241-62, 1991.

CRISCIONE, R. **Ascending aorta parametric modeling and fluid dynamics analysis in a child patient with congenital BAV and ascending aorta aneurysm**. 2013. 123 f. Master Thesis. Genie Biomedical, Université de Montréal, Montréal, 2013.

CROWLEY, T.A.; PIZZICONI, V. **Isolation of plasma from whole blood using planar microfilters for a lab-on-a-chip applications**. Lab on a Chip, v. 5, n. 9, p.922-929, 2005.

DATASUS. **Departament of Informatic of the Unified Health System of Health Ministry from Brazil**. Brazil, 2016.

DAVIES, P.F.; REMUZZI, A.; GORDON, E.J.; DEWEY, C.F.; GIMBRONE, M.A. **Turbulent fluid shear stress induces vascular endothelial cell turnover in vitro.** Proceedings of the National Academy of Sciences of the United States of America, v. 83, n. 7, p. 2114-2117, 1986.

DE LEVAL, M.R.; MIGLIAVACCA G.;DUBINI, F.; JALALI, H.; CAMPORINI, G.; REDINGTON, A.; PIETRABISSA, R. **Use of computational fluid dynamics in the design of surgical procedures:** Application to the study of competitive flows in cavopulmonary connections. The Journal of Thoracic and Cardiovascular Surgery, v. 111, n. 3, p. 502-513, 1996.

DE TULLIO, M.D.; CRISTALLO, A.; BALARAS, E.; VERZICCO, R. **Direct numerical simulation of the pulsatile flow through anaortic bileaflet mechanical heart valve.** J. Fluid Mech., v. 622, p. 259-290, 2009.

DEUTSCH, S.; TARBELL, J.M.; MANNING, K.B.; ROSENBERG, G.; FONTAINE, A.A. **Experimental fluid mechanics of pulsatile artificial blood pumps.** Annual Review of Fluid Mechanics, v.38, p. 65-86, 2006.

EHRLICH, M.P.; ARISAN ERGIN, M.; MCCULLOUGH, J.N.; LANSMAN, S.L.; GALLA, J.D.; BODIAN, C.A.; APAYDIN, A.; GRIEPP, R.B. **Results of immediate surgical treatment of all acute type A dissections**. Circulation, v. 102, n.3, p.248-252, 2000.

ELEFTERIADES, J.A. **Natural history of thoracic aortic aneurysms:indications for surgery, and surgical versus nonsurgical risks**. Ann Thorac Surg, v.74, n. 5, p. 1877-80, 2002.

ERBEL, R.; ALFONSO,F.; BOILEAU, C.; DIRSCH, O.; EBER, B.; HAVERICH, A.; RAKOWSKI, H.; STRUYVEN, J.; RADEGRAN, K.; SECHTEM, U.; TAYLOR, J.; ZOLLIKOFER, C.; KLEIN, W.W.; MULDER, B. PROVIDENCIA, L.A. **Diagnosis and management of aortic dissection**. European Heart Journal, v. 22, n. 18, p. 1642-81, 2001.

FAGGIANO, E.; ANTIGA, L.; PUPPINI, G.; QUARTERONI, A.; LUCIANI, G.B.; VERGARA, C. **Helical flows and asymmetry of blood jet in dilated ascending**

aorta with normally functioning bicuspid valve. Biomechanics and Modeling in Mechanobiology, v. 12, n. 4, p. 801-813, 2013.

FEIJOO, R.A.; ZOUAIN, N; **Formulations in rates and increments for elastic-plastic analysis.** International Journal for Numerical Methods in Engineering, v. 26, n. 9, p. 2031-2048, 1988.

FELDMAN, C.L.; ILEGBUSI, O.J.; HU, Z.; NESTO, R.; WAXMAN, S.; STONE, P.H. **Determination of in vivo velocity and endothelial shear stress patterns with phasic flow in human coronary arteries**: a methodology to predict progression of coronary athersclerosis. American Heart Journal, v. 143, n. 6, p.931-939, 2002.

FLACHSKAMPF, F.; WEYMAN, A.; GUERRERO, J.; THOMAS, J. **Influence of orifice geometry and flow rate on effective valve area:** An in vitro study. JACC, v. 15, n. 5, p. 1173-1180, 1990.

FLUENT INC. **Fluent Flow Modeling Software**. <https://www.ansys.com/Products/Fluids/ANSYS-Fluent>

FLUENT INC. **Fluent 18.1 – User's Guide**, 2018.

FRIEDMAN, M.H.; HUTCHINS, G.M.; BARGERON, C.B.; DETERS, O.J.; MARK, F.F. **Correlation between intimal thickness and fluid shear in human arteries**. Atherosclerosis, v. 39, n.3, p. 425-436, 1981.

FRY, D.L. **Acute bascular endothelial changes associated with incread blood velocity gradients**. Circ.Res., v. 22, n.2, p. 165-197, 1968.

GEERS, A.J.; MORALES, H.G.; FRANGI, A.F. **Comparison of steady-state and transient blood flow simulations of intracranial aneurysms.** Edited by 32nd Annual International Conference of the IEEE EMBS. Buenos Aires, Argentina: 32nd Annual International Conference of the IEEE EMBS, p. 2622-25, 2010.

GIJSEN, F.J.H.; VAN DE VOSSE, F.N.; JANSSEN, J.D. **The influence of the non-Newtonian properties of blood on the flow in large arteries**: steady flow in a carotid bifurcation model. Journal of Biomechanics, v. 32, n.6, p. 601-608, 1999.

GOLDSMITH, H.L.; SKALAK, R. **Hemodynamics**. Annual Review of Fluid Mechanics, v. 7, p. 213-247, 1975.

GOMES, B.A.A. **Simulação *in vitro* do fluxo sanguíneo em modelo aórtico tridimensional de paciente submetido a implante valvar percutâneo***.* 2017. 134 f. Doctoral Thesis (in Portuguese). Faculdade de Medicina, Universidade Federal do Rio de Janeiro, Rio de Janeiro, 2017.

GÜLAN, U.; CALEN, C.; DURU, F.; HOLZNER, M. **Blood flow patterns and pressure loss in the ascending aorta**: A comparative study on physiological and aneurysmal conditions. Journal of Biomechanics, n. 76, n.25, p. 152–159, 2018.

GUNNING, P. S.; SAIKRISHNAN, N.; MCNAMARA, L. M.; YOGANATHAN, A. P. **An in vitro evaluation of the impact of eccentric deployment on transcatheter aortic valve hemodynamics**. Annals of Biomedical Engineering, v. 42, n. 6, p. 1195-1206, 2014.

GUZZARDI, D.G.; BARKER, A.J.; VAN OOIJ, P.; MALAISRIE, S.C.; PUTHUMANA, J.J.; BELKE, D.D.; MEWHORT, H.E.; SVYSTONYUK, D.A.; KANG, S.; VERMA, S.; COLLINS, J.; CARR, J.; BONOW, R.; MARKL, M.; THOMAS, J.D.; MCCARTHY, P.M.; FEDAK, P.W.M. **Valve-related hemodynamics mediate human bicuspid aortopathy**: insights from wall shear stress mapping. Journal of the American College of Cardiology, v. 66, n. 8, p. 892-900, 2015.

HA, H.; KIM, G.B.; KWEON, J.; LEE, S.J.; KIM, N.; YANG, D.H. **The influence of the aortic valve angle on the hemodynamic features of the thoracic aorta**. Scientific Reports, v. 6, 32136, 2016.

HAGAN, P.G.; NIENABER, C.A.; ISSELBACHER, E.M.; BRUCKMAN, D.; KARAVITE, D.J.; RUSSMAN, P.L.; EVANGELISTA, A.; FATTORI, R.; SUZUKI, T.; OH, J.K.; MOORE, A.G.; MALOUF, J.F.; PAPE, L.A.; CAGA, C.; SECHTEM, U.; LENFERINK, S.; DEUTSCH, H.J.; DIEDRICHS, H.; MARCOS Y ROBLES, J.; LLOVET, A.; GILON, D.; DAS, S.K.; ARMSTRONG, W.F.; DEEB, G.M.; EAGLE, K.A. **The international registry of acute aortic dissection (irad):** new insights into an old disease. JAMA, v. 283, n. 7, p. 891-903, 2000.

HALLER, G. **An objective definition of a vortex.** J. Fluid Mech. v. 525, p. 1-26, 2005.

HANSEN, J.T. **Netter's clinical anatomy**. 3 ed. Philadelphia: Elsevier, 2014.

HAO, Q. **Modeling of flow in an in vitro aneurysm model**: a fluid-structure interaction approach. 2010. 111f. Doctoral Thesis. Biomedical Engineering, University of Miami, Coral Gables, 2010.

HARLOW, F.;. NAKAYAMA, P. **Transport of turbulence energy decay rate**. Los Alamos, NM: Los Alamos Scientific Laboratory, p.1-7, 1968.

HOLMÉN, V. **Methods for vortex identification.** 2012. 46f. Master Thesis. Mathematical Sciences, Lunds Universitet, Lunds, 2012.

HOPE, M.D.; WRENN, J;. SIGOVAN, M.; FOSTER, E.; TSENG, E.E.; SALONER, D. **Imaging biomarkers of aortic disease:** increased growth rates with eccentric systolic flow. Journal of the American College of Cardiology, v. 60, n. 4, p. 356-357, 2012.

HOPE, T.A.; MARKL, M.; WIGSTROM, L.; ALLEY, M.T.; MILLER, D.C.; HERFKENS, R.J. **Comparison of flow patterns in ascending aortic aneurysms and volunteers using four-dimensional magnetic resonance velocity mapping**. Journal of Magnetic Resonance Imaging, v. 26, p. 1471-1479, 2007.

HUNT, J.C.; WRAY, A.; MOIN, P. **Eddies, stream, and convergence zones in turbulent flows**. Studying Turbulence Using Numerical Simulation Databases, 2. Proceedings of the 1988 Summer Program, p 193-208, 1988.

HUNTER, P.J.; PULLAN, A.J.; SMAIL, B. H. **Modeling total heart function**. Annu. Rev. Biomed. Eng., v. 5, p. 147-77, 2003.

HUTCHINSON, R.B.; RAITHBY, D.G. **The Additive Correction Multigrid strategy**. Numerical Heat Transfer, v. 5, n. 9, p. 511-37, 1986.

ISSELBACHER, E.M. **Thoracic and abdominal aortic aneurysms**. Circulation, v. 111, n. 6, p. 816-828, 2005.

JAPANESE CIRCULATION SOCIETY JOINT WORKING GROUPS. **Guidelines for diagnosis and treatment of aortic aneurysm and aortic dissection**. Official Journal of the Japanese Circulation Society, v. 77, p. 789-828, 2013.

JIN, S.; OSHINSKI, J.; GIDDENS, D.P. **Effects of wall motion and compliance on flow patterns in the ascending aorta**. Journal of Biomechanical Engineering, v. 125, n. 3, p. 347-354, 2003.

JOHNSON, R.W. **The handbook of fluid dynamics.** Heidelberg Germany: CRC Press Springer, 1998.

JOHNSTON, B.M.; JOHNSTON, P.R.; COURNEY, S.; KILPATRICK, D. **Non-Newtonian blood flow in human right coronary arteries:** Transient simulations. Journal of Biomechanics, v. 39, n. 6, p. 1116-1128, 2006.

JOHNSTON, B.M.; JOHNSTON, P.R.; COURNEY, S.; KILPATRICK, D. **Non-Newtonian blood flow in human right coronary arteries:** steady state simulations. Journal of Biomechanics, v. 37, n. 5, p. 709-720, 2004.

JONES, W.; LAUNDER, B. **The prediction of laminarization with a two-equation model of turbulence**. International Journal of Heat and Mass Transfer, v. 15, n. 2, p. 301-314, 1972.

KATO, K.; OGURI, M.; KATO, N.; HIBINO, T.; YAJIMA, K.; YOSHIDA, T.; METOKI, N.; YOSHIDA, H.; SATOH, K.; WATANABE, S.; YOKOI, K.; MUROHARA, T.; YAMADA, Y. **Assessment of genetic risk factors for thoracic aortic aneurysm in hypertensive patients**. American Journal of Hypertension, v. 21, n. 9, p. 1023-1027, 2008.

KU, D.N.; GIDDENS, D.P.; ZARINS, C.K.; GLAGOV, S. **Pulsatile flow and atherosclerosis in the human carotid bifurcation.** Arteriosclerosis, v. 5, n. 3, p. 293-302, 1985.

KUZMIK, G.A.; SANG, A.X.; ELEFTERIADES, J.A. **Natural history of thoracic aortic aneurysms**. J Vasc Surg, v. 56, n.2, p. 565-571, 2012.

LANDENHED, M.; ENGSTRÖM, G.; GOTTSÄTER, A.; CAULFIELD, M. P.; HEDBLAD, B.; NEWTON-CHEH. C.; MELANDER, O.; SMITH, J.G. **Risk profiles for aortic dissection and ruptured or surgically treated aneurysms**: a prospective cohort study. Journal of the American Heart Association: Cardiovascular and Cerebrovascular Disease, v. 4, n. 1, e001513, 2015.

LEDERLE, F.A.; JOHNSON, G.R.; WILSON, S.E.; CHUTE, E.P.; HYE, R.J.; MAKAROUN, M.S.; BARONE, G.W.; BANDYK, D.; MONETA, G.L.; MAKHOUL, R.G. **The aneurysm detection and management study screening program**: validation cohort and final results. Arch Intern Med, v. 160, n. 10, p. 1425-1430, 2000.

LES, A.S.; SHADDEN, S.C.; FIGUEROA, C.A.; PARK, J.M.; TEDESCO, M.M.; HERFKENS, R.J.; DALMAN, R.L.; TAYLOR, C.A. **Quantification of hemodynamics in abdominal aortic aneurysms during rest and exercise using magnetic resonance imaging and computational fluid dynamics.** Annuals of Biomedical Engineering, v. 38, n. 4, p. 1288-1313, 2010.

LI, J.K. **Dynamics of the vascular system**. *World scientific, v.* 272, 2004.

LONG, D.S.; SMITH, M.L.; PRIES, A.R.; LEY, K.; DAMIANO, E.R. **Microviscometryreveals reduced blood viscosity and altered shear rate and shear stress profiles in microvessels after hemodilution**. Proceedings of the National Academy of Sciences of the United States of America, v. 101, n.27, p. 10060-10065 2004.

MALISKA, C.; **Transferência de Calor e Mecânica dos Fluidos Computacional.** Rio de Janeiro: Livros Técnicos e Científicos Editora, 1995.

MALEK, A.M.; ALPER, S.L.; IZUMO, S. **Hemodynamic shear stress and its role in atherosclerosis**. JAMA, v. 282, n. 21, p. 2035-2042, 1999.

MALVERN, L.E. **Introduction to the mechanics of a continuous medium**. Prentice Hall, Inc., 1977.

MALVINDI, P.G.; PASTA, S.; RAFFA, G.M.; LIVESEY, S. **Computational fluid dynamics of the ascending aorta before the onset of type A aortic dissection.** European Journal of Cardio-Thoracic Surgery, v.51, n. 3, p. 597-599, 2016.

MARIEB, E.; MALLATT, J.; WILHELM, P.; **Human anatomy**. s.l.: Pearson/Benjamin Cummings, 2005.

MATHUR, A.; MOHAN, V.; AMETA, D.; BHARDWAJ, G.; HARANAHALLI, P. **Aortic aneurysm**. J Transl Intern Med, v. 4, n.1, p. 35-41, 2016.

MCMILLAN, D.B.; HARRIS, R.J.; **An atlas of comparative vertebrate histology**. 1 ed. London: Elsevier , 2018.

MENTER, F.R. **Two-equation eddy-viscosity turbulence models for engineering applications**. AIAA Journal, v. 32, n. 8, p. 1598-1605, 1994.

MORBIDUCCI, U.; LEMMA, R.; PONZINI, R.; BOI, A.; BONDAVALLI, L.; ANTONA, C.; MONTEVECCHI, F.M.; REDAELLI, A. **Does flow dynamics of the magnetic vascular coupling for distal anastomosis in coronary artery bypass grafting contribute to the risk of graft failure?** International Journal of Artificial Organs, v. 30, p. 628-639, 2007.

MORBIDUCCI, U.; PONZINI, R.; RIZZO, G.; CARDIOLI, M.; ESPOSITO, A.; DE COBELLI, F.; DEL MASCHIO, A.; MONTEVECCHI, F.M.; REDAELLI, A. **In vivo quantification of helical blood flow in human aorta by time-resolved three-dimensional cine phase contrast magnetic resonance imaging**. Annals of biomedical engineering, v. 37, n.3, p. 515-531, 2009.

MORSI, Y.S. **In vitro comparison of steady and pulsatile flow characteristics of jellyfish heart valve**. The Japanese Society for Artificial Organs, v. 3, p.143-148, 2000.

MYERS, J.G.; MOORE, J.A.; OJHA, M.; JOHNSTON, K.W.; ETHIER, C.R. **Factors influencing blood flow patterns in the human right coronary artery**. Annals of Biomedical Engineering, v. 29, p. 109-120, 2001.

NUMATA, S.; ITATANI, K.; KANDA, K.; DOI, K.; YAMAZAKI, S.; MORIMOTO, K.; MANABE, K.; IKEMOTO, K.; YAKU, H.; **Blood flow analysis of the aortic arch using computational fluid dynamics.** European Journal of Cardio-Thoracic Surgery, v. 49, n. 6, p. 1578-1585, 2016.

PATANKAR, S. V. **Numerical heat transfer and fluid flow**. 1st ed. Hemisphere Publishing Corporation, 1980.

PATANKAR, S.V.; SPALDING, B. **A calculation procedure for heat, mass and momentum transfer in three-dimensional parabolic flows**. Internation Journal of Heat and Mass Transfer, v. 15, p. 1787-1806, 1972.

PERKTOLD, K.; PETER, R.O.; RESCH, M; LANGS, G. **Pulsatile non-Newtonian flow in three-dimensional carotid bifurcation models:** a numerical study of flow phenomena under different bifurcation angles. Journal of Biomedical Engineering, v.13, n. 6, p. 507-515, 1989.

POP, G.A.N.; DUNCKER, D.J.; GARDIEN, M.; VRANCKX, P.; VERSLUIS, S.; HASAN, D.; SLAGER, C.J. **The clinical significance of whole blood viscosity in (cardio)vascular medicine.** Netherlands Heart Journal, v.10, n. 12, p. 512-516, 2002.

POPE, S.B. **Turbulent flows**. Cambridge University Press, 2000.

PORTH, C.; HANNON, R.; POOLER, C.; **Porth pathophysiology**, 1st ed., USA: Lippincott, 2009.

RAGHAVAN, M.L.; VORP, D.A.; FEDERLE, M.P.; MAKAROUN, M.S.; WEBSTER, M.W. **Wall stress distribution on three-dimensionally reconstructed models of human abdominal aortic aneurysm**. Journal of Vascular Surgery, v. 31, n.4, p. 760-769, 2000.

RANUCCI, M.; LADDOMADA, T.; RANUCCI, M.; BARYSHNIKOVA, E. **Blood viscosity during coagulation at different shear rates.** Physiol Rep., v. 2, n. 7, e12065, 2014.

ROACHE, P.J. **Verification and validation in computational science and engineering**. Hermosa Publishers, 446 p., 1998.

RODKIEWICZ, C.; SINHA, P.; KENNEDY, J. **On the application of a constitutive equation for whole human blood.** Journal of biomechanical engineering, v. 112, n. 2, p. 198-206, 1990.

RODRÍGUEZ-PALOMARES, J.F.; DUX-SANTONY, L.; GUALA, A.; KALE, R.; MALDONADO, G.; TEIXIDÓ-TÙRA, G.; GALIAN, L.; HUGUET, M.; VALENTE, F.; GUTIÉRREZ, L; GONZÁLEZ-ALUJAS, T.; JOHNSON, K.M.; WIEBEN, O.; GARCÍA-DORADO, D.; EVANGELISTA, A. **Aortic flow patterns and wall shear stress maps by 4D-flow cardiovascular magnetic resonance in the assessment of aortic dilatation in bicuspid aortic valve disease.** Journal of Cardiovascular Magnetic Resonance, v. 20, n.1, p. 20-28, 2018.

SALAZAR, F.A.; ROJAS-SOLÓRZANO, L.R.; ANTAKI, J.F. **Numerical study of turbulence models in the computation of blood flow in cannulas**. Proceedings of ASME Fluids Engineering Conference, Jacksonville, FL, USA, p. 999-1005, 2008.

SALIBA, E.; SIA, Y. **The ascending aortic aneurysm:** When to intervene? IJC Heart & Vasculature, v. 6, p. 91-100, 2015.

SALLAM, A.M.; HWANG, N.H.C. **Human red blood cell hemolysis in a turbulent shear flow**: contribution of reynolds shear stressess. Biorheology, v. 21, n. 6, p. 783-797, 1984.

SCHINDELIN, J.; ARGANDA-CARRERAS, I.; FRISE, E.; KAYNIG, V.; LONGAIR, M.; PIETZSCH, T.; PREIBISCH, S.; RUEDDEN, C.; SAALFELD, S.; SCHMID, B.; TINEVEZ, J.Y.; WHITE, D.J.; HARTENSTEIN, V.; ELICEIRI, K.; TOMANCAK, P.; CARDONA, A. **Fiji: an open-source plataform for biological-imagem analysis.** Nat Methods, v. 9, n. 7, p. 676-682, 2012.

SCHWARTZ, C.J; MITCHELL. J.R.A. **Observations on localization of arterial plaques**. Circ. Res., v. 11, p. 63-73, 1962.

SIMÃO, M.; FERREIRA, J.M.; TOMÁS, A.C.; FRAGATA, J.; RAMOS, H.M. **Aorta ascending aneurysm analysis using CFD models towards possible anomalies**. Fluids, v. 31, n. 2, p. 1-15, 2017.

SIMMONDS, M.J.; MEISELMAN, H.J.; BASKURT, O.K. **Blood rheology and aging**. Journal of Geriatric Cardiology, v. 10, n. 3, p. 291-301, 2013.

SMITH, J.D.; ADAMS, B.R.; JACKSON, R.E.; SUO-ANTTILA, S.J. **Use of RANS and LES turbulence models in CFD predictions for industrial gas-fired combustion applications**. Journal of the International Flame Research Foundation, p. 1-40, 2017.

SOARES, A.A.; GONZAGA, S.; OLIVEIRA, C.; SIMÕES, A.; ROUBOA, A.I. **Computational fluid dynamics in abdominal aorta bifurcation: non-Newtonian versus Newtonian blood flow in a real case study.** Computer Methods in Biomechanics and Biomedical, v. 20, n. 7, p. 822, 8-31, 2017.

STANDRING, S. (Ed.). **Gray's anatomy: the anatomical basis of clinical practice***.* 41 ed. New York: Elsevier Limited, 2016.

STUART, J.; KENNY, M.W. **Blood rheology.** Journal of Clinical Pathology, v. 33, n. 5, p. 417-429, 1980.

SUN, Z.; CHAICHANA, T. **A systematic review of computational fluid dynamics in type B aortic dissection.** International Journal of Cardiology, v. 210, p. 28-31, 2016.

SUO, J.; OSHINSKI, J.; GIDDENS, D. **Entrance flow patterns in the coronary arteries**: a computational study. Summer Bioengineering Conference, June 25-29, Key Biscayne, Florida, p. 513-514, 2003.

TANYI, B.; THATCHER, R.; **Iterative solution of the incompressible Navier-Stokes equation.** Intentional Journal for Numerical Methods in Fluids, v.22, n. 4, p. 225-240, 1996.

THEODORSEN, T. **Mechanism of turbulence**. Proc. Second Midwestern Conf. of Fluid Mechanics, Ohio State University, Columbus, Ohio, p. 1-9, 1952.

THURSTON, G.B.; HENDERSON, N.M. **Effects of flow geometry on blood viscoelasticity.** Biorheology, v. 43, n. 6, p. 729-746, 2006.

TU, C.; DEVILLE, M. **Pulsatile flow of non-Newtonian fluids through arterial stenoses**. Journal of Biomechanics, v. 29, n. 7, 899-908, 1996.

VAN DE VOSSE, F.N.; GIJSEN, F.J.H.; WOLTERS, B.J.B.M. **Numerical analysis of coronary artery flow.** New York: Bioengineering Conference, ASME, p. 17-18, 2001.

VERTSTEEG, H.K.; MALALASEKERA, W. **An introduction to computation fluid dynamics:** the finite volume method. 1 ed. New York: Longman Scientific & Technical, 1995.

WALBURN, F.J.; SCHNECK, D.J. **A constitutive equation for whole human blood**. Biorheology, v. 13, n. 3, p. 201-210, 1976.

WEIGANG, E.; KARI, F.A.; BEYERSDORF, F.; LUEHR, M.; ETZ, C.D.; FRYDRYCHOWICZ, A.; HARLOFF, A.; MARKL, M.; **Flow-sensitive four-dimensional magnetic resonance imaging: flow patterns in ascending aortic aneurysms**. European Journal of Cardio-thoracic Surgery, v. 34, n. 1, p. 11-16, 2008.

WESOLOWSKI, S.A.; SABINI, C.G.; FRIES, A.M.; SAWYER, P.N. **The significance of turbulence in hemic systems and in the distribution of the atherosclerotic lesion.** *Surg.*, v. 151, n. 57, p. 151-62, 1965.

WIENBAUM, S.; CARO, C.G. **A macromolecule transport model for the arterial wall and endothelium based on the ultrastructural specialization observed in electron microscopic studies**. J. Fluid. Mech., v. 74, n. 4, p. 611-640, 1976.

WILCOX, D. **Reassessment of the scale determining equation for advanced turbulence models.** AIAA Journal, v. 19, n. 2, p. 248-251, 1988.

YEARWOOD, T. L.; CHANDRAN, K.B. **Experimental investigation of steady flow through a model of the human aortic arch**. Journal of Biomechanics, v. 13, n. 12, p. 1075-1088, 1980.

YOGANATHAN, A.P.; CAPE, E.G.; SUNG, H.W.; WILLIAMS, F.P.; JIMOH, A. **Review of hydrodynamic principles for the cardiologist: applications to the study of blood flow and jets by imaging techniques**. JACC, v. 12, n. 5, p.1344-1353, 1988.

ZHOU, J.; ADRIAN, R.J.; BALACHANDAR, S. **Mechanisms for generating coherent packets of hairpin vortices in channel flow**. J. Fluid Mech, v. 387, p. 353-396, 1999.

A1.
Grid Test

Three meshes with different levels of refinement (2×10^6, 4×10^6 and 8×10^6 nodes) were tested using the ANSYS Meshing tool. The mesh was defined employing the tetrahedron method, and it was refined near the aorta's surface, to better capture the boundary layer region (Figure. A1.1). A first mesh was defined and the subsequent meshes were created by dividing and multiplying the control volumes by two, imposing restrictions of maximum and minimum control volume size.

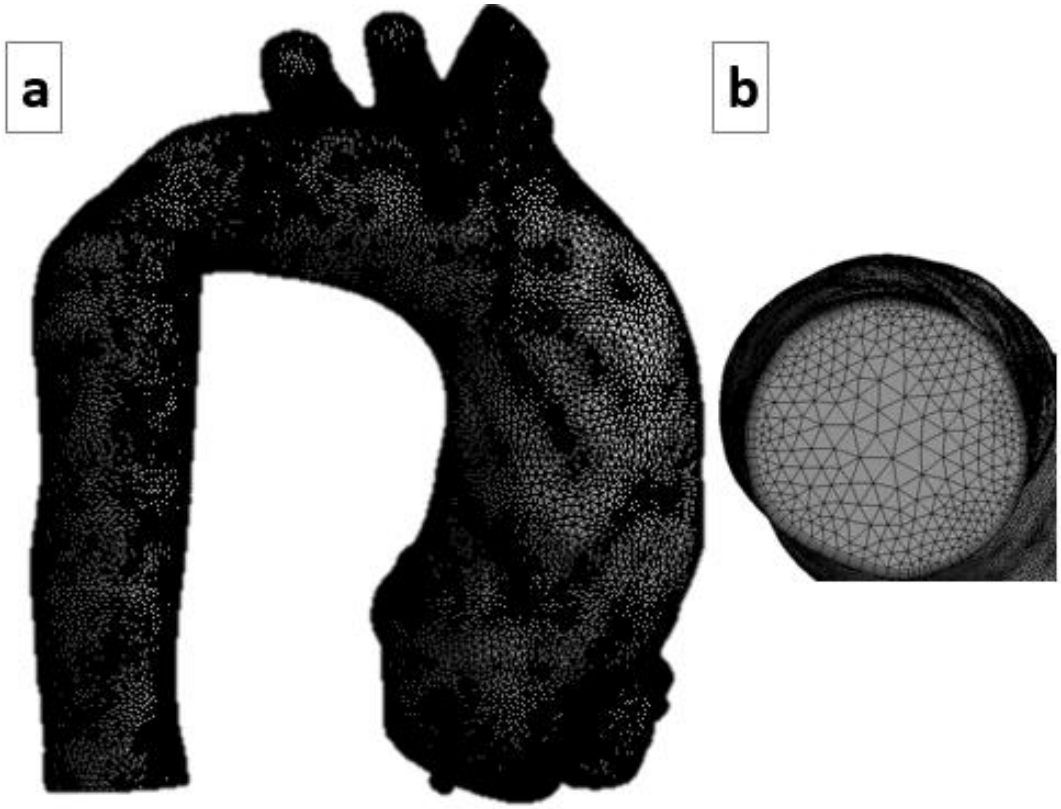

Figure A1.1 – Mesh used in the numerical solution. (a) Complete Geometry (b) Cross-section at right coronary level.

The parameters to verify mesh convergence were global parameters, considered important for the present study, which are the dimensionless mean wall pressure ($\bar{P}$) and dimensionless mean wall shear stress ($\overline{WSS}$) at the aorta's surface reference area (A_{ref}), which is the selected superficial aorta's area, as defined in section 4.1 (Figs. 4.4 and 4.5)

$$\bar{P} = \frac{1}{A_{ref}} \int_{A_{ref}} \frac{p - p_{in}}{\rho\, w_{in}^2 / 2}\, dA \qquad ; \quad \overline{WSS} = \frac{1}{A_{ref}} \int_{A_{ref}} \frac{\tau_w}{\rho\, w_{in}^2 / 2}\, dA \qquad \text{(A1.1)}$$

and the maximum value of dimensionless wall distance (y^+) of the first internal node to the walls (Eq. 3.36).

The aorta of Patient 3, corresponding to the second year, was selected to illustrate the mesh convergence results. Table A1.1 presents the results obtained for these three variables. The error (ϵ) of both pressure and wall shear stress between the data obtained with coarser mesh and the finer mesh is included in the table. The table also presents the Grid Convergence Index, GCI, (Roache, 1998) defined as

$$GCI = F_S \frac{|\epsilon|}{r^m - 1} \qquad ; \quad |\epsilon| = \frac{\phi_1 - \phi_2}{\phi_1} \qquad , \quad r = \frac{h_2}{h_1} \qquad \text{(A1.2)}$$

where the subscripts 1 and 2 refer to fine and course, respectively. *m*=2 is the convergence order of the scheme and F_S=2 is a safety factor.

Table A1.1 – Variation of $\overline{WSS}$, $\bar{P}$ and y^+ for three mesh sizes

Nodes	y^+	**Wall Shear Stress**			**Pressure**		
[$\times 10^3$]		$\overline{WSS}$	$\|\epsilon\|$ **[%]**	**GCI [%]**	$\bar{P}$	$\|\epsilon\|$ **[%]**	**GCI [%]**
200	4.2	0.011	1.9	1.3	0.144	9.0	6.0
400	3.4	0.012	1.0	0.6	0.132	2.7	1.8
800	3.2	0.012			0.129		

Analyzing Table A1.1, the first observation regarding the mesh distribution that can be made is that for all cases, the mesh refinement near the wall was adequate for the turbulence model selected ($\kappa - \omega$ SST), i.e., $y^+ < 5$. It can also be seen that as the mesh is refined, the errors of the selected variables are reduced. Further, the difference between the results obtained with the 4×10^6 nodes mesh and those obtained with the finest mesh are inferior to 3%. The GCI obtained comparing the intermediate to the fine mesh solutions is 0.63% for the mean wall shear stress and 1.80% for the mean pressure, indicating that for an accuracy of 2%, the intermediate size mesh is sufficient.

The profile of the dimensionless axial velocity component (Eq. 4.1) along the z axis, is shown in Figure A1.2 for the three meshes, while the profile of the

dimensionless pressure (Eq. 4.1), also along z-axis, is illustrated in Figure A1.3. An excellent agreement was obtained, especially between the two finer meshes.

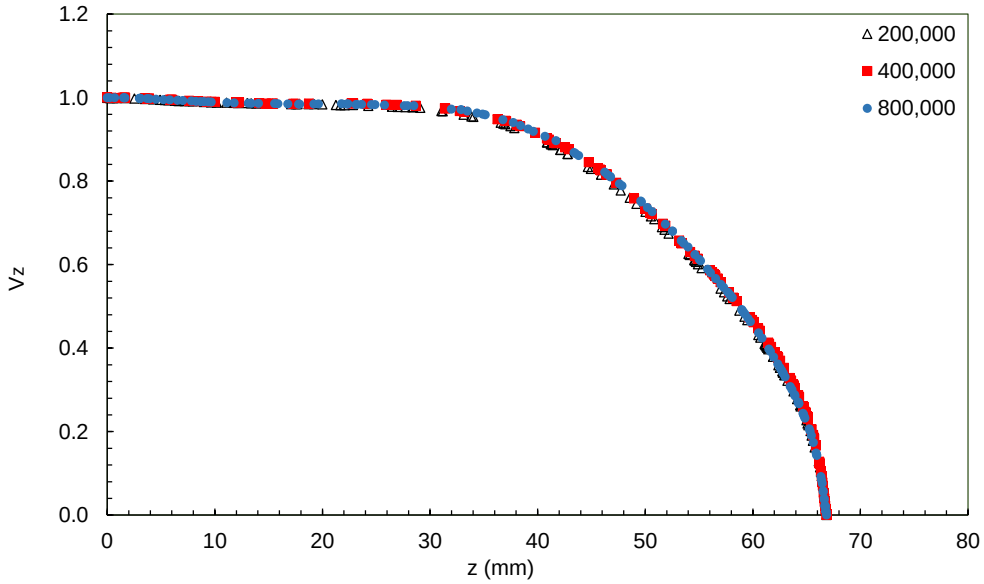

Figure A1.2 – Grid Test. Dimensionless axial velocity along z-axis of three meshes

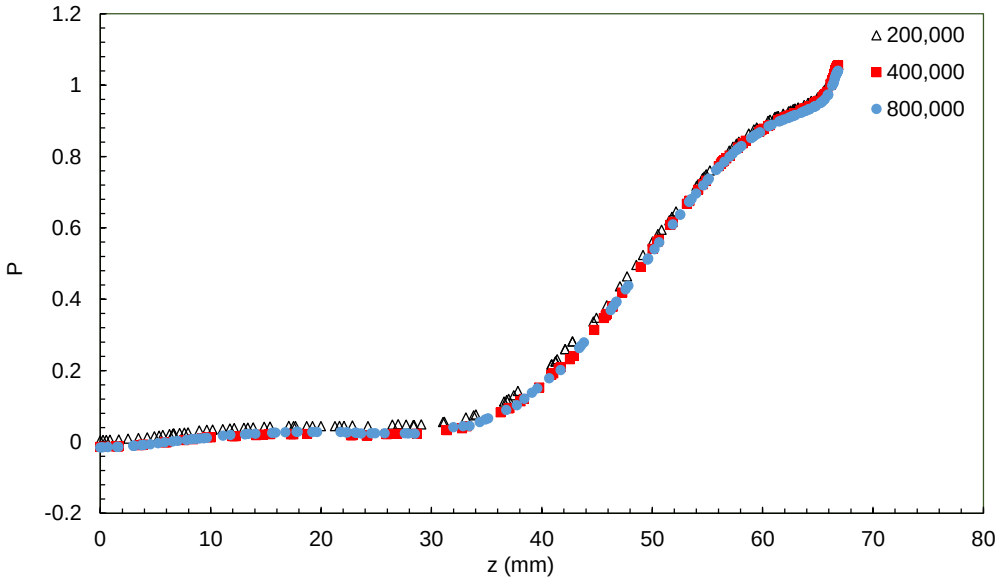

Figure A1.3 – Grid Test. Dimensionless pressure along z-axis of three meshes

To better evaluated the mesh influence in the solution, two planes were created in the region of interest of the aorta. One plane, as shown in Figure A1.4 (a), is parallel to the inlet plane, being displaced 30 mm from inlet along the z-axis. The second plane is a central plane coincident with the z-axis, perpendicular to the incoming jet and to the right coronary, as shown in Figure A1.4 (b). Information such as the area average x, y, and z dimensionless velocity components and area average dimensionless pressure were determined in both planes and the influence of the mesh refinement was examined. The mesh influence on both turbulent quantities, κ and ω, were also explored, being dimensionless as shown in Eq. A1.3.

$$K = \frac{\kappa}{w_{in}^2} \quad ; \quad \Omega = \frac{\omega D}{w_{in}} \tag{A1.3}$$

being w_{in} the velocity of entry, D the diameter of entry, K dimensionless turbulence kinetic energy and Ω dimensionless specific rate of dissipation.

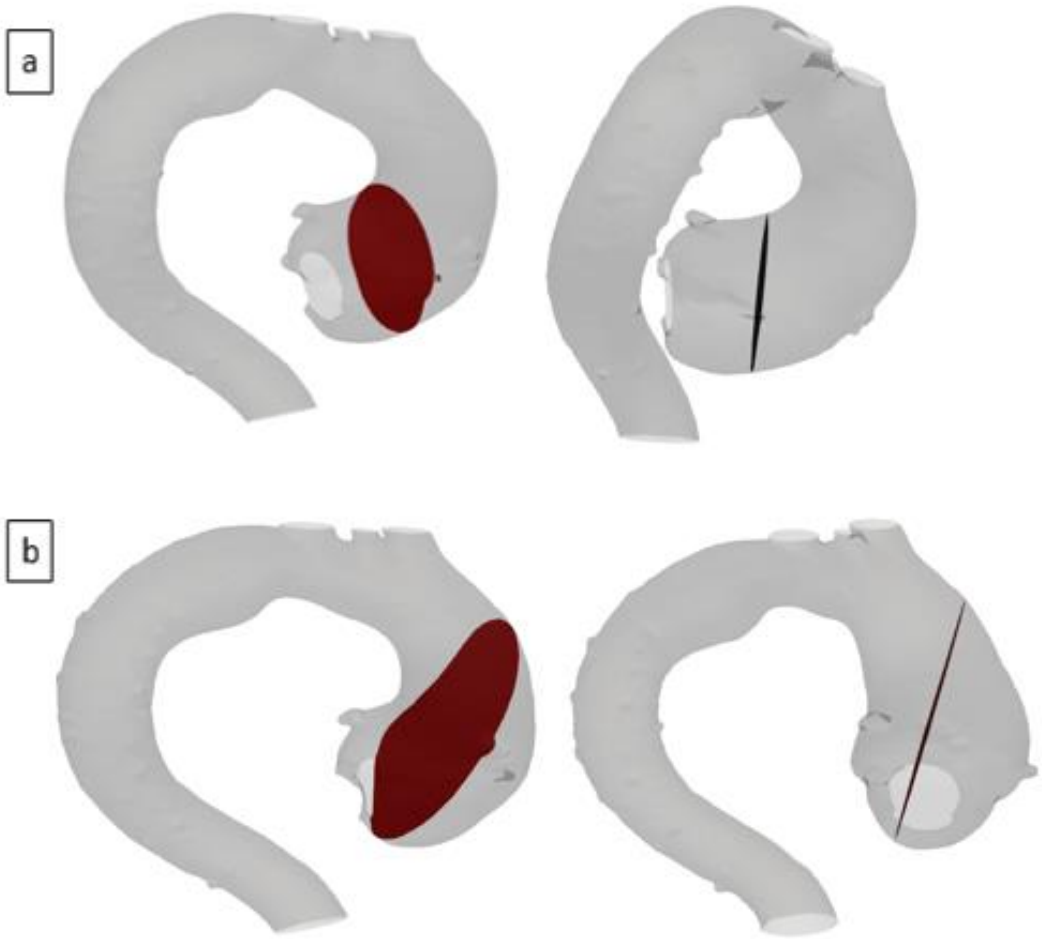

Figure A1.4 – Planes created to evaluate the mesh influence. (a) Plane I. (b) Plane II.

Table A1.2 shows the area average values determined in Plane I and the grid convergence index associated of one mesh in relation to the next finer mesh for each variable. The same type of results obtained in Plane II are shown in Table A1.3. Examining both tables, it is observed that as the mesh is refined the difference between the results is reduced. Examining the CGI of the intermediate mesh of 4×10^6 nodes, it can be seen that for both Plane I and Plane II, an accuracy smaller than 2% is obtained for all variables.

Table A1.2 – Parameters evaluated of Plane I

Nodes	**Velocity Components**					
[$\times 10^3$]	V_x	**GCI [%]**	V_y	**GCI [%]**	V_z	**GCI [%]**
200	-0.062	-2.7%	-0.165	-0.8%	0.238	0.5%
400	-0.064	-0.5%	-0.163	-1.2%	0.240	0.3%
800	-0.065		-0.166		0.241	

Nodes	**Turbulent Quantities**				**Pressure**	
[$\times 10^3$]	K	**GCI [%]**	Ω	**GCI [%]**	P	**GCI [%]**
200	0.016	0.5%	9.0	3.5%	-0.154	-3.7%
400	0.016	0.3%	9.5	1.7%	-0.163	-1.5%
800	0.016		9.7		-0.166	

Table A1.3 – Parameters evaluated of Plane II

Nodes	**Velocity Components**					
[$\times 10^3$]	V_x	**GCI [%]**	V_y	**GCI [%]**	V_z	**GCI [%]**
200	-0.197	-0.64%	-0.128	-1.4%	0.135	5.8%
400	-0.193	-0.58%	-0.130	-1.6%	0.148	0.5%
800	-0.190		-0.127		0.149	

Nodes	**Turbulent Quantities**				**Pressure**	
[$\times 10^3$]	K	**GCI [%]**	Ω	**GCI [%]**	P	**GCI [%]**
200	0.014	1.0%	11.9	5.9%	0.126	9.9%
400	0.014	0.2%	13.0	2.4%	0.110	0.5%
800	0.014		13.5		0.109	

Since the finer mesh requires a significant large computing effort and does not improve the solution, the most efficient choice is the mesh of 4×10^6 nodes. Although it is necessary to build a new mesh for each different aorta´s configuration (two geometries for each patient), approximately the same number of grid points, with similar distribution, was employed in all cases analyzed in this dissertation.